
Galaxy Formation and Evolution in a Λ CDM Universe

Qi Guo



München Juli 2009

Galaxy Formation and Evolution in a Λ CDM Universe

Qi Guo

Dissertation der Fakultät für Physik
der
Ludwig-Maximilians-Universität München

vorgelegt von Qi Guo
aus ShanDong, China

München, den 21 Juli 2009

Erstgutachter: Prof. Dr. Simon D. M. White

Zweitgutachter: Prof. Dr. Gerhard Börner

Tag der mündlichen Prüfung: 28 September 2009

Contents

Zusammenfassung (Summary in German)	5
Summary	7
1 Thesis objectives	11
1.1 Motivation	11
1.2 Essential cosmology	12
1.2.1 The homogeneous Universe	12
1.3 Structure formation	13
1.3.1 Linear theory	14
1.3.2 Spherical Top-Hat collapse	15
1.3.3 Mass Function and Merger Rate	16
1.3.4 N-body simulations	18
1.4 Baryonic processes and semi-analytic models	21
1.4.1 Gas cooling	22
1.4.2 Star Formation	23
1.4.3 Satellite galaxies in clusters	24
1.4.4 Chemical evolution	25
1.4.5 Feedback	26
1.4.6 Stellar Population Synthesis	28
1.5 Outline	29
2 Galaxy growth in the concordance ΛCDM cosmology	31
2.1 Introduction	31
2.2 The simulation and the galaxy formation model	34
2.2.1 The simulation	35
2.2.2 Merger rates	35
2.3 Galaxy growth rates	36
2.4 Growth Rates for FOF groups	42
2.5 Summary and discussion	44
3 High Redshift Galaxy Populations and their Descendants	49

3.1	Introduction	50
3.2	Galaxy Formation	52
3.2.1	Dust Model	53
3.2.2	Light-cone	56
3.3	Mock Catalogue	57
3.3.1	Sample Selection	57
3.3.2	Redshift Distributions	60
3.3.3	Star Formation Rate	61
3.3.4	Mass-Metallicity Relations	62
3.3.5	Correlation Functions	62
3.4	The Descendants of High Redshift Galaxies	63
3.4.1	Number Density, Satellite Fraction and Stellar Mass Growth	64
3.4.2	Morphology	66
3.4.3	Stellar Mass Functions	67
3.4.4	Colour-Stellar Mass Distributions	69
3.4.5	The Dark Halos of LBGs	70
3.4.6	Descendant Correlations	72
3.4.7	Relation between LBGs, BXs and DRGs	74
3.5	Summary and Discussion	75
4	Galaxy Formation Efficiency	77
4.1	Introduction	77
4.2	Dark Matter Halos	78
4.3	Galaxy Formation Efficiency	80
4.3.1	Connecting Galaxies to Dark Matter Halos	80
4.3.2	Dynamical Mass of the Milky Way	82
4.3.3	Galaxy Formation Efficiency	83
4.3.4	Tully-Fisher Relation	84
4.4	Conclusions and Discussion	85
5	Galaxy Formation in a Hierarchical Universe	87
5.1	Introduction	88
5.2	N-body Simulations	89
5.3	Galaxy Formation Models	90
5.3.1	Stellar Mass Function in DLB07	91
5.3.2	Reionization and Cooling	92
5.3.3	Star Formation	93
5.3.4	Supernova Feedback	95
5.3.5	Satellite Galaxies in Groups and Clusters	97
5.3.6	Mergers	99
5.3.7	Bulge Formation	100
5.3.8	Black Hole Growth and AGN feedback	101
5.3.9	Metal Enrichment	102
5.3.10	Stellar Synthesis and Dust Extinction	102
5.4	Results	102

5.4.1	Global Mass Function and Luminosity Functions	103
5.4.2	Correlation Functions	105
5.4.3	Satellite Luminosity Function around the Milky Way	109
5.4.4	Galaxy Stellar Mass Function in Rich Clusters	110
5.4.5	Intracluster Light	111
5.5	Conclusion and Discussion	112
6	Concluding remarks	115
	Bibliography	120

Zusammenfassung

In dieser Arbeit untersuche ich die Entstehung von Galaxien in der standard Λ CDM-Kosmologie. Hierfür werden die beiden N-body Simulationen, „Millenium“ (MS-I) und „Millenium II“ (MS-II), und semi-analytische Modelle der Galaxienentwicklung herangezogen. Die gesamte Arbeit besteht aus vier Teilen.

Im ersten Teil wird untersucht welche Rolle Verschmelzungen für das Anwachsen der Sternmasse in Galaxien spielen. Dem wird eine Analyse analoger Prozesse während der Verschmelzung von dunkle Materie Halos gegenübergestellt. Es zeigt sich, dass das Wachstum von Galaxien maßgeblich von der Sternmasse der Vorgänger bestimmt wird. Dahingegen findet sich nur eine schwache Rotverschiebungsabhängigkeit. Im Gegensatz dazu besteht eine starke Rotverschiebungsabhängigkeit für den Massenzuwachs von Halos aus dunkler Materie. Hier ist das Halowachstum aufgrund von massiven Verschmelzungsprozessen proportional zu $(1+z)$, wobei die Massenabhängigkeit sehr gering ist. Folglich spielt die Verschmelzungsaktivität eine wesentlich geringere Rolle für das Wachstum von Galaxien als für das von dunkle Materie Halos.

Im zweiten Teil meiner Arbeit vergleiche ich die Vorhersagen des Modells mit drei verschiedenen Galaxienpopulation bei hohen Rotverschiebungen. Die Modellgalaxien werden Lyman-break Galaxien (LBG), welche bei Rotverschiebungen von $z \sim 3$ beobachtet werden, mit Galaxien hoher Sternentstehungsraten bei $z \sim 2$ (BX) und mit fernen roten Galaxien (DRG) ebenfalls bei Rotverschiebungen um $z \sim 2$ gegenübergestellt. Anzahldichte, Rotverschiebungsverteilung und Häufung (Clustering) dieser drei Populationen werden von den Modellgalaxien gleichzeitig reproduziert. Dem Modell zufolge kommen LBGs, BXs und DRGs zusammen nur für weniger als die Hälfte der gesamten Sternentstehung bei Rotverschiebungen zwischen $z = 1.5$ und 3.2 auf. Modell LBGs und DRGs entwickeln sich zu roten elliptischen Galaxien, wohingegen die BXs sehr unterschiedliche Schicksaale haben können. Im Allgemeinen ist das Wachstum der stellaren Komponente von Galaxien von frühester Zeit bis $z \sim 1$ durch Sternentstehung geprägt, danach dominieren Verschmelzungen. Das Clustering der Nachkommen aller drei Populationen nimmt mit abnehmender Rotverschiebung zu und übertrifft das von L^* -Galaxien bei $z = 0$.

Im dritten Teil wird, beruhend auf der beobachteten Stern- und der simulierten Halo-Massenfunktion eine direkte, von Galaxienentwicklungsmodellen unabhängige, Verbindung zwischen der Sternmasse von Galaxien und deren Halomassen etabliert. Dabei wird angenommen, dass eine monotone Beziehung zwischen der Sternmasse und der, über den gesam-

ten Formationszeitraum hinweg erfassten, maximalen Halomasse besteht. Die so von den Galaxien ableitbare Halomassenfunktion zeigt gute Übereinstimmung mit direkten Halomassenbestimmungen, welche von „Weak-lensing“-Beobachtungen abgeleitet wurden. Dieses Ergebnis kann als Bestätigung für die Selbstkonsistenz des Λ CDM Modells interpretiert werden. Auch die modellierte Tully-Fisher-Beziehung für die Sternmassen von Galaxien stimmt qualitativ mit den Beobachtungen überein, was zeigt, dass es möglich ist simultan die beobachteten Leuchtkraftfunktionen und die Tully-Fisher-Beziehung in der gegebenen Λ CDM Kosmologie zu reproduzieren. Die von dem semi-analytischen Modell ableitbare Effizienz der Konversion von Baryonen in Sterne erweist sich sehr viel geringer als es die neuesten hochaufgelösten hydrodynamischen Simulationen des Entstehungsprozesses von Spiralgalaxien vorhersagen. Damit wird deutlich, dass derzeitige Simulationen noch Probleme haben eine typische Galaxienpopulation hervorzubringen.

Im letzten Teil meiner Arbeit stelle ich ein neues selbstkonsistentes Modell für die Galaxienentwicklung vor. Hierbei wird insbesondere auf die Supernova-Rückkoppelung, den Massenaustausch verschiedener baryonischer Komponenten, die Reionisation und den Masseverlust aufgrund von Gezeitenkräften eingegangen. Letzter ist von herausragender Bedeutung für die Modellierung von massearmen Galaxien. Mit diesem Modell wurde die Galaxienpopulationen für MS-I und MS-II berechnet. Die Kombination der Resultate basierenden auf MS-I und MS-II erlaubt sowohl die Entwicklung der leuchtkraftstärksten Zentralgalaxien in Galaxienhaufen als auch die Formation der kleinsten sphäroiden Zwerggalaxien nachzuvollziehen. Es zeigt sich, dass die stellare Massenfunktion in einem Bereich von $10^8 M_\odot$ bis $10^{12} M_\odot$ gut mit den Beobachtungen übereinstimmt. Ohne zusätzliche Justierung wird gleichzeitig auch die beobachtete Leuchtkraftfunktion für Satellitengalaxien in milchstraßenähnlichen Systemen reproduziert. Eine eingehende Untersuchung verdeutlicht, dass nur eine Supernova-Rückkoppelung, welche von der Zirkulargeschwindigkeit abhängt, eine Übereinstimmung mit der beobachteten stellaren Massenfunktion bis hinunter zu Massen von $10^8 M_\odot$ herbeiführen kann. Die Reionisation, hingegen, beeinflusst nur die Formation der kleinsten sphäroiden Galaxien. Für Galaxienhaufen mit Massen um $10^{14} M_\odot$ befinden sich, dem Modell zufolge, ein Bruchteil von ungefähr 10% aller Sterne im intra-haufen Medium. Dieser Anteil wächst leicht mit der Masse der Haufen an, was im Allgemeinen von Beobachtungen bestätigt wird. Auch die beobachteten Korrelationsfunktionen massenlimitierter Sample roter und blauer Galaxien stimmen qualitativ mit den Modellresultaten überein. Auf größeren Skalen jedoch liegen die Modelle systematisch über den Beobachtungen, was sich mit der zu hoch angenommenen Normalisierung der Leistungsspektrums (σ_8) in den Simulationen (MS-I und MS-II) erklären lässt.

Summary

In this thesis, I study the galaxy formation in the concordance Λ CDM cosmology, using the “Millennium” and “Millennium II” N-body simulations, and semi-analytic models of galaxy formation. Our work investigates galaxy populations both in the local universe and at high redshift.

In Chapter 1, I explain the motivation for this thesis and briefly review the necessary theoretical background.

First, I explore the growth of galaxies in a Λ CDM universe, using a public model galaxy catalogue which was calculated by implementing galaxy formation models on the Millennium Run. I find that galaxy growth through major mergers depends strongly on stellar mass, but only weakly on redshift. The relative importance of major mergers, minor mergers, and star formation in galaxy growth varies with stellar mass and with redshift. For galaxies significantly less massive than the Milky Way, star formation dominates the growth at all epochs, while for galaxies significantly more massive than the Milky Way, growth through mergers is always the dominant process. At the stellar mass of the Milky Way, star formation dominates at $z > 1$ and mergers at later times. Except for massive systems, minor mergers contribute more to galaxy growth than major mergers at all redshifts and at all stellar masses. At every stellar mass, the growth rates through star formation increase rapidly with increasing redshift. Specific star formation rates are a decreasing function of stellar mass not only at $z = 0$ but also at all higher redshifts. In contrast, I find the growth rates of dark matter halos depend strongly on redshift, but only weakly on mass. This analysis is presented in Chapter 2

In Chapter 3, I shift the focus to high redshift galaxy populations and their evolution. Based on the model galaxy catalogue, I establish a mock catalogue and select three high redshift galaxy populations according to observational selection criteria. Those are: Lyman break galaxies at $z \sim 3$ (LBGs), optically selected star-forming galaxies at $z \sim 2$ (BXs), and distant red galaxies at $z \sim 2$ (DRGs). I first show that the galaxy formation model can simultaneously reproduce the abundances, redshift distributions and clustering of all three observed populations. Model LBGs, BXs and DRGs together account for less than half of all star formation over the range $1.5 < z < 3.2$; many massive, star-forming galaxies are predicted to be too heavily obscured to appear in these populations. About 85% of model galaxies selected as DRGs are star-forming, with SFRs in the range 1 to $\sim 100M_{\odot}/\text{yr}$. Discrepancies between the model predictions and the observations include

the star formation rate distributions for the LBGs and the BXs, which reflect different initial mass functions and the scatter in model dust properties, and the metallicities in the BXs. I find the predicted galaxies are predominantly disk-dominated. Stellar masses for LBGs and BXs are $\sim 10^{9.9}M_{\odot}$, and for DRGs are $\sim 10^{10.7}M_{\odot}$. Only about 30% of model galaxies with $M_* > 10^{11}M_{\odot}$ are classified as LBGs or BXs at the relevant redshifts, while 65% are classified as DRGs. Almost all model LBGs and BXs are the central galaxies of their dark halos, but fewer than half of the halos of any given mass have an LBG or BX central galaxy. Half of all LBG descendants at $z = 2$ would be identified as BX's, but very few as DRGs. Clustering increases with decreasing redshift for descendants of all three populations, becoming stronger than that of L^* galaxies by $z = 0$, when many have become satellite galaxies and their typical stellar mass has increased by a factor of 10 for LBGs and BXs, and by a factor of 3 for DRGs. This growth is dominated by star formation until $z \sim 1$ and thereafter by mergers. Merging is predicted to be more important for LBG and DRG descendants than for BX descendants. Most LBGs and DRGs end up as red ellipticals, while BXs have a more varied fate. Over 70% of local galaxies with $M_* > 10^{11}M_{\odot}$ are predicted to have at least one LBG/BX/DRG progenitor.

In order to establish a galaxy formation model-independent link between galaxy stellar mass and dark matter halo mass, I use a stellar mass function determined from the SDSS over the stellar mass range $10^8M_{\odot} < M_* < 10^{12}M_{\odot}$ and a dark matter halo mass function obtained using large high-resolution simulations. Under the assumption that the stellar mass of a galaxy is an increasing function of the maximum mass ever attained by its halo, it is possible to predict halo mass as a function of stellar mass. The result is in good agreement with direct measurements of mean halo mass as a function of stellar mass from gravitational lensing analysis of SDSS data, providing additional evidence of the overall consistency of the Λ CDM cosmology. This model predicts a halo mass for the Milky Way of about $2.6 \times 10^{12}M_{\odot}$, which is larger than most (but not all) recent direct estimates, but consistent with inferences from the MW/M31 Timing Argument. I define the efficiency of galaxy formation as the fraction of the baryons associated with the halo present in stellar form and find it reaches a maximum of 20% at masses slightly below that of the Milky Way and falls rapidly at both higher and lower masses. These galaxy formation efficiencies are much lower than in recent high resolution simulations of the formation of spiral galaxies, showing that these are not yet viable models for the formation of typical members of the galaxy population. I also use this model to study the Tully-Fisher relation, and show that it is possible to reproduce simultaneously galaxy luminosity functions and the Tully-Fisher relation in the context of a Λ CDM cosmology. This analysis is presented in Chapter 4

Finally, in Chapter 5, I develop a new self-consistent model of galaxy formation and implement this simultaneously on the Millennium and the Millennium II Simulations. For the first time it becomes possible to follow the formation and evolution of galaxies all the way from dwarf galaxies as faint as the faintest spheroidals around the Milky Way to the most massive cD galaxies in clusters. To reproduce the observed stellar mass distribution, I introduce a new supernova feedback model, in which the fraction of the energy used to reheat the interstellar medium and to blow gas out of a halo is a decreasing function of the circular velocity of the host dark matter halo. I further assume that the time scale to reincorporate gas from the surroundings decreases with the circular velocity of the dark matter halo. I also explore environmental effects on galaxy evolution in groups and

clusters by taking into account ram pressure and tidal stripping, disruption, and merging of satellite galaxies. I show that this new model is able to reproduce both the shape and the amplitude of the observed galaxy stellar mass function in the local Universe, from $10^{12}M_{\odot}$ down to 10^8M_{\odot} . Both the stellar mass correlation function and the correlation functions of galaxies as a function of stellar mass and galaxy colors are also qualitatively reproduced. The amplitude, however, is higher than observed, suggesting that a lower value for the fluctuation amplitude σ_8 is needed than is adopted in the MS-I and MS-II. Promisingly, the luminosity function of satellite galaxies around the Milky Way is reproduced automatically. I find that, in the presence of circular-velocity-dependent supernova feedback, reionization has little effect on the mass and luminosity functions of field galaxies. It determines, however, the number density of very faint satellite galaxies in Milky Way-like systems. In rich clusters of mass $\sim 10^{14}M_{\odot}$, I find around 10% of the total stars to be distributed in the intracluster medium. This fraction increases slightly with cluster mass. Both results are broadly consistent with observation. Finally, I show that the results for the MS-I and in the MS-II agree well for L_* galaxies, where both have good resolution and good statistics.

Thesis objectives

Abstract

I explain the motivation of my thesis work and briefly review the relevant background. In the standard paradigm, galaxies are formed within dark matter halos and merge with each other after halo aggregation. In the first part, I briefly summarize the currently favored cosmological models, I introduce linear perturbation theory and I illustrate non-linear evolution with a spherical collapse model. I also review recent progress in N-body simulations. In the second part, I briefly review the most relevant baryonic processes of galaxy formation. An overview of this thesis is presented in the last section of this chapter.

1.1 Motivation

In the standard picture of modern cosmology (Weinberg 1972; Peebles 1993; Peacock 1999), structure grows from initial density fluctuations produced just after of the Big Bang. The perturbations are believed to have been created during *Inflation* (Guth 1981; Liddle & Lyth 2000), a period when the scale factor grew exponentially. In the cold dark matter scenario, small structures form first and then aggregate into larger systems due to the attractive effects of gravity. This model reproduces clusters, filaments and cosmic sheets as observed and has become the most favored theory of structure formation. By now, large-scale structure formation in a dark matter dominated universe has been well explored with the help of high-resolution simulations on supercomputers. However, many baryonic processes relevant to galaxy formation are still far from clear. These include shock heating, accretion of cold gas, star formation, feedback and internal structural evolution.

The primary focus of this thesis is to understand how the baryons are loaded in dark matter halos, to figure out whether galaxy formation traces the dark matter halos, to study the crucial processes of supernova feedback, gas recycling and environmental modification, and to interpret high-redshift observations with current galaxy formation theories. For these purposes, one needs to understand the evolution of the universe as a whole, including both large-scale structure formation and these baryonic processes. A complete review of galaxy formation will easily fill hundreds of pages and here I restrict myself to some of the most basic aspects which are most relevant to this work.

1.2 Essential cosmology

1.2.1 The homogeneous Universe

The central premise of modern cosmology is that the Universe is homogeneous and isotropic on large scales. With this assumption, the geometry of the Universe can be described using the Robertson-Walker metric

$$ds^2 = c^2 dt^2 - a(t)^2 \left(\frac{dr^2}{1 - kr^2} + r^2 (d\Omega^2) \right) \quad (1.1)$$

where (r, θ, ϕ) are spherical comoving coordinates and Ω is solid angle. k indicates the curvature of the Universe: the Universe is open/closed/flat if k is less than/greater than/equal to zero. $a(t)$ is the scale factor which determines the size of the Universe. By convention, $a(0)$ is often assumed to be 1 at the present day. The redshift (z), which is one of the most important variables in cosmology, is related to a as follows:

$$z \equiv \frac{\nu_e}{\nu_o} - 1 = \frac{a_o}{a_e} - 1 \quad (1.2)$$

where ν is the frequency of a photon, and the subscripts e and o represent emitted and observed, respectively.

In Einstein's General Relativity Theory, matter and space-time are related by the equation

$$G_{ik} = R_{ik} - \frac{1}{2} g_{ik} R - \Lambda g_{ik} = \frac{8\pi G}{c^4} T_{ik} \quad (1.3)$$

where G_{ik} is the space-time geometry tensor, and T_{ik} is the energy-momentum tensor. Λ represents *dark energy* when it appears on the right-hand side of this equation and is considered dynamic, and is usually called the cosmological constant when moved to the left-hand side and considered constant.

Applying this equation to the homogeneous and isotropic Universe and assuming that the Universe behaves like an ideal fluid, one obtains the Friedmann equations:

$$\frac{\ddot{a}}{a} = -\frac{4\pi G}{3} (\rho + 3p/c^2) + \frac{1}{3} \Lambda c^2, \quad (1.4)$$

$$\frac{\dot{a}^2}{a} = \frac{8\pi G \rho}{3} - \frac{kc^2}{a^2} + \frac{\Lambda c^2}{3} \quad (1.5)$$

where ρ is the matter density and p is the pressure. Note that for a cosmological constant the dark energy term $\frac{\Lambda c^2}{3}$ is time independent, but to solve these equations in general, one needs to know its equation of state. The Universe consists of three components: baryons, dark matter and dark energy. For relativistic particles, which dominate the energy in the early universe, $p = \frac{1}{3} \rho c^2$. The energy density decays as a^{-4} . For non-relativistic matter, which dominates the energy density after matter-radiation equivalence, $p = 0$ and the energy density decays as a^{-3} . The equation state of dark energy is $p = \omega \rho c^2$ and its density does not evolve with time if it is a cosmological constant for which $\omega = -1$. Dark energy has been dominant only since recent epochs.

Table 1.1: Fit to the WMAP5, BAO and SNLL data

parameter	WMAP+BAO+SNe
Total matter density	$\Omega_{tot}=1.0052\pm 0.0064$
Matter density	$\Omega_{tot}=0.279\pm 0.015$
Baryon density	$\Omega_b=0.0462\pm 0.0015$
Cosmological constant	$\Omega_\Lambda=0.721\pm 0.015$
Hubble constant	$h=0.701\pm 0.013$
Power-spectrum Normalization	$\sigma_8=0.817\pm 0.026$
Spectral index	$n_s=0.960^{+0.014}_{-0.013}$
Decoupling redshift	$z_{dec}=1088.2 \pm 1.1$
Matter-radiation equality redshift	$z_{eq} = 3280^{+88}_{-89}$
Reionization optical depth	$\tau = 0.084 \pm 0.016$
Age of the Universe	$t = 13.73 \pm 0.12[Gyr]$

In the following I list several parameters which are commonly used in cosmological studies. The first one is the Hubble constant:

$$H = \dot{a}/a \tag{1.6}$$

It is usually parameterized as $H = 100h \text{ km s}^{-1}\text{Mpc}^{-1}$, where h is a dimensionless factor. Another is the relative density, which is defined as in terms of the critical density:

$$\Omega_* = \frac{\rho_*}{\rho_{crit}}, \rho_{crit} = \frac{3H^2}{8\pi G} \tag{1.7}$$

where the subscripts * denote different types of component.

Recent observations including measurements of the Cosmic Microwave Background (CMB) fluctuations indicate a flat Universe with the critical density ($\rho_{crit} = 1$), which is consistent with the predictions of inflation theory. In such a Universe, the expansion can be completely specified by the above parameters

$$H^2(t) = H_0^2 \left(\frac{\Omega_r}{a^4(t)} + \frac{\Omega_m}{a^3(t)} + \Omega_\Lambda \right) \tag{1.8}$$

where the subscript 0 denotes the present time, r is for the radiation field, and m is for the dark matter and Λ is for the dark energy. The Ω 's are all specified at the current time and the dark energy has been assumed to be a cosmological constant. The first term on the right-hand side $\frac{\Omega_r}{a^4(t)}$ can be ignored if one considers evolution after matter-radiation equivalence.

In Table 1.1, I show the cosmological parameters based on the Wilkinson Microwave Anisotropy Probe (WMAP) five-year results (Dunkley & et al. 2009).

1.3 Structure formation

The assumption of a homogeneous and isotropic Universe holds on scales larger than 100 Mpc and only at such large scales are the Friedmann equations sufficient to describe the

dynamical evolution. On smaller scales, however, the Universe is far from homogeneous. Rather it is full of structures, like walls, filaments and clusters.

In the CDM paradigm, structure grows from primordial fluctuations generated during inflation. The evolution of the massive, weakly interacting dark matter particles is only governed by gravity. This makes it easier to study their dynamics either analytically or numerically. It is usually convenient to separate the structure formation into two regimes: the linear growth regime where the fluctuations are small and the equations of motion can be linearized around the homogeneous solution; and the non-linear regime where the perturbation is large and the non-linear objects emerge. The first case applies to the early Universe and to the evolution of structures on very large scales (>100 Mpc), while the latter is important for the evolution of the dark matter halos within which galaxies form. The linear evolution is now well understood, while the non-linear evolution is difficult to explore using a purely analytic approach unless special symmetries are assumed. N -body simulations, which trace the evolution of collisionless dark matter particles, are an excellent tool to deal with the non-linear evolution. In the following I will describe the linear theory briefly in Sec. 1.3.1. I will then introduce a special analytic solution which describes the spherical top-hat collapse model, which illustrates the most basic processes (Sec. 1.3.2, Sec. 1.3.3). I summarize some basic aspects of cosmological N -body simulations in Sec. 1.3.4.

1.3.1 Linear theory

A region with density higher than the background can accrete material from its surroundings and become even denser if its gravity wins over its pressure. This process will lead to an instability which ultimately causes a fluctuation to collapse into a gravitationally bound object. In 1902, Jeans derived a characteristic scale length (*the Jeans length*) λ_J , above which fluctuation can grow, for a uniform static gas (Jeans 1902). This work was later extended to an expanding background to study the evolution of primordial perturbations in the early universe (Lifshitz 1946; Silk 1967, 1968; Doroshkevich et al. 1967; Peebles & Yu 1970; Weinberg 1971; Chibisov 1972; Field 1971).

The evolution of an ideal fluid can be described by the Euler-Lagrange Poisson system, which consists of three equations : the continuity equation, Euler's equation and Poisson's equation.

$$\frac{d\rho}{d\tau} + \rho(\nabla \cdot \mathbf{v}) = 0; \quad (1.9)$$

$$\frac{d\mathbf{v}}{d\tau} = -\nabla \Phi - \frac{1}{\rho} \nabla \mathbf{p}; \quad (1.10)$$

$$\nabla^2 \Phi = 4\pi \mathbf{G} \rho. \quad (1.11)$$

where p is the pressure, Φ is the potential and τ is the conformal time. ∇ and $d/d\tau$ are the derivative with respect to \mathbf{x} and τ respectively. Assuming an adiabatic perturbation, in the linear regime, we have

$$\ddot{\delta} + \frac{\dot{a}}{a} \dot{\delta} = \frac{\nabla^2 p}{\bar{\rho}(1+\delta)} + 4\pi G \bar{\rho} \delta. \quad (1.12)$$

where $\delta(= \rho/\bar{\rho} - 1)$ is the density contrast. When calculated in Fourier space, we find an equation of the same form. All Fourier modes are decoupled and grow independently from each other. At small scales, fluctuations cannot grow, while at scales larger than the Jeans length

$$\lambda > \lambda_J = c_s \left(\frac{\pi}{G\rho} \right)^{1/2} \quad (1.13)$$

where c_s is the sound speed, each mode has two solutions, a decaying one and a growing one.

CMB measurements tell us that baryon perturbations at $z \sim 1000$ are very small, the temperature contrast $\frac{\Delta T}{T} \sim 10^{-5}$ and $\delta(z_{CMB}) < 5 \times 10^{-5}$. In a flat universe dominated by baryons ($\Omega_b = 1, \Omega_\Lambda = 0$), $\delta \propto t^{2/3} \propto (1+z)^{-1}$. So at the present day, the predicted density contrast is

$$\delta(z=0) < 0.1. \quad (1.14)$$

This suggests that non-linear structures could never have formed!

A non-baryonic component (dark matter) is thus required, whose fluctuations should have been able to grow sufficiently to form the large structures observed today. This dark matter interacts with baryons in a very weak way, if any, so that at the time of recombination, when the fluctuations in the baryonic component are very small, the fluctuations in the dark matter can have a larger amplitude. Shortly after recombination, the baryonic fluctuations catch up with the dark matter perturbations and together they grow into the observed structures.

The initial density fluctuations from which structure grows are usually analyzed in Fourier space. One particular primordial spectrum for the perturbations first proposed in the 1970's, is the so-called Harrison-Zel'dovich spectrum, which is a scale-invariant spectrum with power law form $P(k) \sim k^n$ ($n=1$). This particular spectrum is consistent with the latest results from WMAP and gained motivation from the inflation theory in the 1980's (e.g. Guth & Pi 1982; Hawking 1982; Starobinsky 1982)

Although the primordial spectrum is usually taken as a power law, the observed power spectrum has a very different shape, which is determined by the nature of the dominant component and the interaction of the different components (such as the coupling between photons and baryons). The net effect is usually described by a *transfer function* $T(k)$. The power spectrum at any redshift of interest is expressed as:

$$P(k, z) = P(k, z_0) T^2(k) \frac{D(z)}{D(z_0)} \quad (1.15)$$

where $D(t)$ is the growing mode of Eq. 1.12 and z_0 denotes a very early time.

1.3.2 Spherical Top-Hat collapse

When the density contrast $\delta > 1$, structure formation enters the non-linear regime and linear theory is not able to describe the evolution anymore. I will describe a particular case of spherical collapse to give some insight into the nonlinear evolution. This is also a basic process for understanding the hierarchical formation process which I will describe later.

In the most simple case, the perturbation is distributed homogeneously within a spherical region. The density contrast within this region is $\delta(t_0)$. Here we assume an *Einstein-de*

Sitter universe for simplicity. The evolution of this overdense region has the same form as Eq. 1.12, which is a consequence of Birkhoff's theorem in general relativity (which is the relativistic analogue of Newton's Iron Sphere Theorem). This mini-universe will expand but at a slower rate compared to the background universe. The expansion goes on until the density within it satisfies

$$\frac{\rho_p}{\rho} \simeq 5.6 \quad (1.16)$$

At this point this overdense region stops expanding and starts to collapse.

At time t_{coll} , the system collapses into a point with infinite density if the pressure can be ignored and if the configuration remains spherically symmetric. In reality, however, density fluctuations are not perfectly spherical, leading to *violent relaxation* during the collapse. According to the virial theorem, the overdensity of the final virialized region is

$$\frac{\rho_p}{\rho} \sim 180 \quad (1.17)$$

The corresponding radius is the virial radius, r_{vir} . At time t_{coll} an extrapolation of linear perturbation theory would give

$$\delta_{coll} \simeq 1.68. \quad (1.18)$$

Note that here we assume an Einstein-de Sitter Universe. The analysis can be easily extended to other cosmologies, however.

1.3.3 Mass Function and Merger Rate

The previous subsection suggests that a region will collapse at a certain time t , if its extrapolated linear density contrast at that time is $\delta > \delta_c$ ($\delta_c=1.686$ in the case of top hat collapse). At any given time, the number density $n(M)$ of objects with masses between M and $M + dM$ is equivalent to the probability of $\delta > \delta_c$ on scale R ($\sim M^{-3}$). Press & Schechter (1974) proposed a simple analytical model to calculate the number density of such objects as a function of mass. In particular, if the linear density field is Gaussian, the distribution of perturbations on a smoothing scale R , corresponding to a mass $M(R)$, may be written:

$$p(\delta)d\delta = \frac{1}{\sqrt{2}\sigma(M)} \exp\left[-\frac{\delta^2}{2\sigma^2(M)}\right]d\delta \quad (1.19)$$

where $\sigma^2(M)$ is the mean square linear density fluctuation in a sphere with radius R . δ is the density contrast $(\rho - \bar{\rho})/\bar{\rho}$. The probability of finding the fluctuation δ to be above the critical value δ_c is

$$P_{>\delta_c}(M) = \int_{\delta_c}^{\infty} p(\delta)d\delta = \frac{1}{2}\left[1 - \text{erfc}\left(\frac{\delta_c}{\sqrt{2}\sigma(M)}\right)\right] \quad (1.20)$$

where $\text{erfc}(x)$ is the complementary error function, for which $\text{erfc}(0)=1$. Consider an arbitrarily large scale R for which $\sigma(M)$ is arbitrarily small. Eq. 1.22 indicates that only half of the total mass is contained in virialized objects. Press & Schechter argue that mass in underdense regions will collapse into overdense regions and they multiply Eq. 1.20 by a

factor of 2 to account for these masses. This argument has some merit but it is far from convincing to say that it will lead to a factor of two.

A related problem of the Press-Schechter approach is called the *cloud-in-cloud* problem. A region which smoothed on a scale R has $\delta < \delta_c$ and thus is “uncollapsed”, may reside in a denser region when smoothed on the larger scale $R' > R$ for which $\delta' > \delta_c$ which is collapsed after all. This problem is solved (Bond et al. 1991) by calculating the probability of the largest value of the smoothing scale R_{max} within which the density threshold is exceeded. The halo containing a particular particle, at whose position the smoothed linear density contrast is calculated, is assumed to have a mass $M \sim R_{max}^3$. Assuming a top hat smoothing in k-space, the trajectory of $\delta(\sigma^2(M))$ executes a Brownian random walk, e.g. each increment of $\delta(S + \Delta S) - \delta(S)$, where $S(M) = \sigma^2(M)$ is independent of the previous step. This is called excursion set theory and is sometimes referred to as the extended Press-Schechter theory (EPS). Under this assumption, the probability that a trajectory first crosses the threshold in the interval $(S, S+dS)$, where $S = \sigma^2$, is

$$f_s(S, \delta_c) = \frac{\delta_c}{\sqrt{2\pi}S^{3/2}} \exp\left[-\frac{\delta_c}{2S}\right] dS. \quad (1.21)$$

Integrating Eq. 1.21, one has

$$P_{>\delta_c}(M) = 1 - \operatorname{erfc}\left(\frac{\delta_c}{\sqrt{2}\sigma(M)}\right). \quad (1.22)$$

which is the same as Eq. 1.20 except that the “arbitrary” factor of 2 has now been derived explicitly. Eq. 1.21 represents the fraction of mass associated with halos with mass $M(S)$. The comoving number density at time t can be expressed as

$$n(M, t) dM = -2 \frac{\bar{\rho}}{M} \frac{\partial F}{\partial R} \frac{dR}{dM} dM \quad (1.23)$$

$$= \sqrt{\frac{2}{\pi}} \frac{\bar{\rho}}{M^2} \frac{\delta_c}{\sigma} \frac{d \ln \sigma}{d \ln M} \exp\left(\frac{-\delta_c^2}{2\sigma^2}\right) dM \quad (1.24)$$

Following the spirit of random walking, it is easy to derive the conditional mass function

$$f(S_1, \delta_1 | S_2, \delta_2) dS_1 = \frac{1}{\sqrt{2\pi}} \frac{\delta_1 - \delta_2}{(S_1 - S_2)^{3/2}} \exp\left(-\frac{(\delta_1 - \delta_2)^2}{2(S_1 - S_2)}\right) dS_1. \quad (1.25)$$

where $S_1 > S_2$ and $\delta_1 > \delta_2$. Note $S_1 > S_2$, the change from S_2 to S_1 corresponds to a mass growth from $M_1(S_1)$ to $M_2(S_2)$ ($M_2(S_2) > M_1(S_1)$). This equation describes the fraction of the mass in objects of mass M_2 at t_2 which were already in a collapsed objects of mass M_1 at the earlier time t_1 . If the time interval $t_2 - t_1$ is very short, a sudden jump in mass can be identified as accretion of another halo. For a halo of a given mass M_2 , the merger rate (the number of mergers a halo undergoes per unit time) can be determined as:

$$\frac{P_M(M_1, M_2 - M_1, \delta_1 | S_2, \delta_2)}{dt/t} = \frac{1}{2} \int_{S(M_1)}^{S(M_2 - M_1)} \frac{M_2}{M_1} \frac{t * d\delta/dt}{(2\pi)^{1/2} (S_1 - S_2)^{3/2}} \frac{\min(M_1, M_2 - M_1)}{M_2} dS_1 \quad (1.26)$$

where $M_1/(M_2 - M_1)$ sets the mass ratio of the progenitors. For example, if one is interested in major mergers, which are usually defined as mergers between two halos with mass ratio larger than one third, we set $M_1 = 3/4 \times M_2$.

Given the conditional mass function for a certain cosmology, one can easily build up the merger tree for a dark matter halo, by selecting a set of progenitors randomly for this halo and then repeating the random selection procedure on their progenitors progressively back in time. The following properties are guaranteed by the Markov characters of the random walks: 1) the merger history of an object does not depend on its future; 2) the merger history of an object does not depend on its environment – k-modes are independent from each other. By combining with the mass function, an ensemble of merger trees for all halos can thus be built (Kauffmann & White 1993a; Cole et al. 1994; Somerville & Kolatt 1999a; Parkinson et al. 2008; Cole et al. 2008). This Monte Carlo Method has an advantage over direct simulation in that it is less time consuming and is free from resolution limits. On the other hand, it is less rigorous because the validity of the underlying model is uncertain.

Finally, I show the probability that a halo of mass M_1 at time t_1 ends up in a more massive halo with mass M_2 at the later time t_2 :

$$f(S_2, \delta_2 | S_1, \delta_1) dS_2 = \frac{1}{\sqrt{2\pi}} \left[\frac{S_1}{S_2(S_1 - S_2)} \right]^{3/2} \frac{\delta_2(\delta_1 - \delta_2)}{\delta_1} \times \exp\left[-\frac{(\delta_2 S_1 - \delta_1 S_2)^2}{2S_1 S_2 (S_1 - S_2)}\right] dS_2. \quad (1.27)$$

This can be extended to calculate the probability that one halo will merge with another for comparison with galaxy pair counts in observations.

1.3.4 N-body simulations

Although analytic models, such as the PS and EPS theories, are valuable in providing us with a physical understanding of the basic processes in non-linear structure formation, they are unable to describe all aspects of evolution in the real universe where the detailed structure of individual systems is often of great interest. Fig. 1.1 shows structures in a Λ CDM universe as simulated by (Springel et al. 2005b). Obviously, in most cases, structures are highly asymmetric. Simplified theories suffer further from the assumptions used to derive them. For example, EPS assumes Markov random walks, which eliminates some environment effects: dark matter halos of given mass form in the same way in regions with different density, unlike in simulations (e.g. Gao and White 2007). EPS is expected to work in an approximate manner. For a full understanding of the non-linear evolution one has to resort to direct simulations.

Dark matter particles have very small interaction cross section and their evolution obeys the collisionless Boltzmann equation. They are usually described by a distribution function $f(\mathbf{r}, \mathbf{v})$ in phase space. The basic idea of N-body simulation is to replace the distribution function $f(\mathbf{r}, \mathbf{v})$ by a set of N particles, each of the which represents a δ - function in phase-space. These dark matter particles evolve under their self-gravity. When the number of particles is large enough, they provide a good approximation to the evolution of the function $f(\mathbf{r}, \mathbf{v})$.

The most straightforward way to calculate the force on each particle is to sum up the gravitational force from all the other particles (*PP* codes). This method requires a computational time scaling roughly as N^2 and thus cannot be used for simulations involving large

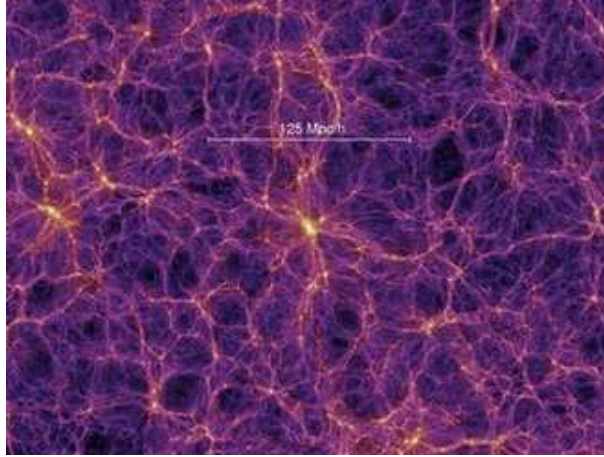


Figure 1.1: The redshift zero distribution of dark matter in a slice of $15h^{-1}\text{Mpc}$ from the Millennium Simulation. Intensity encodes surface density and color encodes velocity dispersion (Springel et al. 2005).

numbers of particles. An alternative is the so-called particle-mesh (*PM*) scheme. The idea is to assign the particle mass to a regular grid and then to solve the Poisson's equation in Fourier space. Note that periodic boundary conditions are usually assumed in simulations, which enables one to use Fast Fourier Transform Techniques (FFT) to calculate the gravitational potential on the grid. The FFT is basically of order $N\log N$ (N is the number of grid points), leading to a considerable increase of the computational speed. The *PM* scheme has its own shortcoming because the force resolution on small scales is poor. The P^3M method combines the advantages of the *PP* method and the *PM* method, by using the *PP* method on small scales and the *PM* method on large scales.

An alternative procedure is a *Tree code*, which adopts a hierarchical algorithm. The basic idea is to treat distant clumps of particles as a single mass point. The size of the clumps is determined by the distance in the sense that cell sizes are larger at larger distances. The gravitational potential is given by the sum over the multipole expansion of the gravitational fields of these groups. The two *N*-body simulations, MS-I and MS-II, which are the foundation of this thesis, are based on the *TreePM* codes Gadget2 and Gadget3 (Springel 2005c). Other methods include the Adaptive Mesh Refinement (AMR) and related algorithms (Kravtsov et al. 1997; Knebe et al. 2001).

Internal structure of dark matter halos

The internal structure of dark matter halos is important for determining many crucial processes related to galaxy formation, for example, gas cooling rates, sizes of galaxy disks, dynamical friction times of satellite galaxies within a cluster, and interactions between dark matter and baryons (Chapter 5).

Navarro et al. (1997a) found a universal density profile for dark matter halos in a wide

variety of hierarchical cosmologies :

$$\rho(r) = \frac{\rho_s}{(r/r_s)(1+r/r_s)^2} \quad (1.28)$$

where r_s is a characteristic radius and ρ_s a characteristic density. Density increases as $\rho \propto r^{-1}$ near the center ($r \ll r_s$) and falls as $\rho \propto r^{-3}$ at large radii. Over much of the halo, $\rho \propto r^{-2}$, an isothermal profile is a good approximation and this is often adopted in semi-analytic models.

One important parameter describing the internal structure of dark matter halos is the concentration parameter, which is defined as

$$c = \frac{r_s}{r_{vir}} \quad (1.29)$$

where r_{vir} is the virial radius of the halo. This concentration parameter is a function of halo mass, with higher values for low mass halos (Navarro et al. 1997a; Merritt et al. 2005, 2006).

Another important parameter is the spin parameter λ ($=J|E|^{1/2}G^{-1}M^{-5/2}$, where J , E and M are the total angular momentum, energy and mass of the dark matter halo). It describes the angular momentum acquired by an asymmetric halo through tidal torques caused by clumps in its surroundings. Baryons have the same specific angular momentum as dark matter when collapse begins. During the subsequent evolution, angular momentum may be lost from baryon clumps to the dark matter due to dynamical friction. The final specific angular momentum carried by the cooled gas determines the galaxy disk sizes in the center of the potential. The distribution of the spin parameter for dark matter halos is found to be

$$p(\lambda) = \frac{1}{\sqrt{2\pi}\sigma_\lambda} \exp\left[-\frac{\ln^2(\lambda^{3/2})}{2\sigma_\lambda^2}\right] \frac{d\lambda}{\lambda} \quad (1.30)$$

where $\bar{\lambda}=0.04$ and $\sigma_\lambda=0.5$. This distribution depends on halo mass M and on cosmological parameters only in a very weak way. Studies of the profiles of angular momentum J within halos have also been made (e.g. Bullock et al. 2001). Although this detailed angular momentum profile is not explored in this thesis, it could easily be implemented in future work to improve the treatment of disk formation.

Dark matter substructures

In the hierarchical scenario, small objects form first and then merge with each other, forming larger systems. Early simulations suggested a smooth and featureless structure for dark matter halos, but with higher resolution it became clear that dark halos are in fact, predicted to contain substantial substructure (Moore et al. 1999; Klypin et al. 1999). After it is accreted onto a larger system, the outskirts of a small halo are removed very rapidly, while its core can often survive as a *substructure*. Typically around 10% of the total mass within r_{vir} is locked in these substructures (subhalos). Fig. 1.2 shows substructures in a cluster taken from the Millennium Simulation. These subhalos are dynamically stable structures and are the nodes of merger trees on which we implement physical recipes for baryons to follow galaxy formation and evolution. A detailed description of the construction

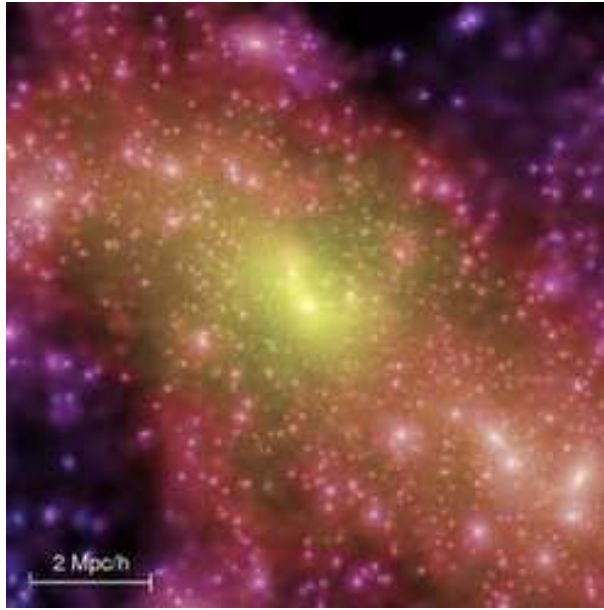


Figure 1.2: Substructures in a cluster (Springel et al. 2005).

of these merger trees and of the galaxy formation models implemented on them can be found in Springel et al. (2005b), Croton et al. (2006), De Lucia & Blaizot (2007) (See also Chapter 5)

1.4 Baryonic processes and semi-analytic models

Galaxies form in dark matter halos through gas condensation and star formation. The Λ CDM model predicts an almost power law mass function for dark matter halos, while observations reveal a Schechter luminosity function for galaxies, with a well defined characteristic luminosity and a lower abundance of objects both at low and high mass with respect to the power law fit to the halo abundance. This implies a variation in mass-to-light ratio with halo mass. In Chapter 4, I will discuss galaxy formation efficiency as a function of halo mass in details.

Despite our success in understanding dark matter dominated structure formation, it is far from clear how galaxies form because this involves more complicated dissipative processes in the non-linear regime. The most straightforward way to approach this problem is to simulate galaxy formation by incorporating a representation of all the physics processes into a code which follows hydrodynamics in addition to N-body treatment of dark matter evolution. In such simulations, gas and stars are coupled to dark matter via gravity alone. Although hydro-simulations can trace the dynamics of diffuse gas well, most of the other important processes are well beyond their resolution limitations and are not well understood. For example, star formation and feedback can only be described with phenomenological recipes. An alternative is the so-called semi-analytic approach. The

basic idea is to implement physical recipes for baryonic processes into the dark matter halo merger trees extracted from N-body simulations. Compared to hydro-simulations, this method is much less time consuming and is thus very useful for exploring a range of physical models and for determining their parameters. The recipes are based mainly on results from detailed hydro-simulations or on directly observed relations. Below I briefly describe the most relevant parts of such codes. Detailed implementation of the SAM used in my own work can be found in Chapter 5.

1.4.1 Gas cooling

A crucial ingredient of galaxy formation is the cooling of gas. There are four main channels through which gas cooling can take place, corresponding to four different temperature ranges.

I) Inverse Compton scattering of CMB photons by electrons. The corresponding time-scale is longer than the Hubble time at late times, so it is only important at very high redshift.

II) $T_v < 10^4 K$, deexcitation of the fine and hyperfine structure lines of heavy elements, if present, and deexcitation of rotational or vibrational energy levels of molecules. Gas is usually neutral at this temperature and excitation occurs through particle collisions.

III) $10^4 K < T_v < 10^{7.5} K$, decay of excited atoms (neutral or partially ionized) or emission through the recombination of electrons and ions. Metallicity plays an important role in this temperature range.

IV) $T_v > 10^{7.5} K$, Bremsstrahlung emission. At such high temperature, gas is almost completely ionized and cooling is dominated by free-free transitions in electron-ion collisions. This dominates in massive clusters.

The cooling rate per unit volume depends on gas density and metallicity.

Before structure forms, gas may be taken to have the same distribution as the dark matter. During gravitational collapse, gas falls into the gravitational well and shocks to a high temperature. In small halos, the cooling is so efficient that the gas loses this energy immediately and continues to collapse towards the center on a free-fall time scale. In massive halos, however, the shocked gas cools less rapidly and can form a quasi-static hot atmosphere. Radiation in the central region may remove the thermal pressure and lead to a cooling flow onto the galaxy in the center. The characteristic mass to separate these two regime is around $10^{12} M_\odot$ (Rees & Ostriker 1977). Numerical simulations suggest a lower value of a few times $10^{11} M_\odot$ (Birnboim & Dekel 2003). These studies usually assume a spherical collapse. In reality, a lot of mass may be accreted along filaments. A recent study (Dekel et al. 2009) shows that at high redshift, even for galaxies as massive as the Milky Way, most of the gas is acquired through narrow cold streams which penetrate the shock-heated atmosphere without being significantly heated. The cooling model adopted in this work takes into account the two different collapse modes assuming the spherical model of White & Frenk (1991). This has been checked in detail against detailed hydrodynamics simulations by Yoshida et al. (2002) and Benson et al. (2001). Nevertheless, more effort is needed in the future to study whether cold streams from filaments can significantly change the story.

A relevant issue is angular momentum transfer during gas cooling. The high efficiency of

gas cooling at early times, causes the later assembly of disks to proceed by coalescence of cold gas clumps. As these clumps merge onto the main galaxy, they can lose a large fraction of their initial angular momentum through dynamical friction. The resulting disks are substantially smaller than observed and contain relatively little stellar mass. Much effort has been directed to solving this problem, mainly by invoking some form of feedback to delay collapse (Sommer-Larsen et al. 1999; Thacker & Couchman 2001), or by adopting an alternate initial fluctuation spectrum with reduced small-scale power (Sommer-Larsen & Dolgov 2001). Some authors (Governato et al. 2004) claim that the problem can be significantly reduced by improving the numerical resolution, but there is no consensus yet on the true solution. Semi-analytic modelers usually assume angular momentum conservation of the cooling gas, which leads to a disk with scalelength consistent with observations (Mo et al. 1998; de Jong & Lacey 2000; Cole et al. 2000; Firmani & Avila-Reese 2000). I have developed a new model to follow the angular momentum accumulation history during gas cooling, merging and star formation processes. The detailed description will be presented in Chapter 5

1.4.2 Star Formation

Cooling gas is assumed to settle to in the center of the potential and to form a cold gas disk. When this disk has accumulated enough mass, gravitational instability leads to episodes of star formation. In general, there are four key ingredients in the star formation process.

I) Giant Molecular cloud (GMC) formation. The star formation in the local universe is observed to be associated with molecular gas. GMC formation is usually driven by turbulence induced by large-scale collapse or by feedback. One can thus relate GMC formation to the global properties a galaxy. In simulations, a critical value of gas density, supposedly a “natural” scale for gravitational instability, is usually introduced, above which GMC formation and star formation can occur. In addition, metallicity plays a role in the formation of molecular gas by enhancing the formation of dust grains on which molecules can form. Many studies about GMC formation have been published (e.g. Krumholz et al. 2008) and this may be included explicitly in our future work.

II) Star formation rates. The facts that GMCs and young star clusters are strongly correlated in space and that GMCs with star formation are very rare suggest a typical life for GMCs of $\sim 10^7$ yr. Assuming axisymmetry for a local perturbation in the disk, the dispersion relation is

$$\omega^2 = \kappa^2 - 2\pi G \Sigma_{gas} |k| + k^2 c_s^2 \quad (1.31)$$

where κ , Σ_{gas} and c_s are the epicyclic frequency, gas surface density and sound speed of the gas, respectively. ω and k are the circular frequency and wavenumber. The timescale for a perturbation to grow is $\tau \sim 1/(\omega) \propto 1/\Sigma_{gas}$. In terms of star formation rate,

$$SFR \propto \Sigma_{gas}^n, \quad (1.32)$$

we have $n \sim 2$ according to Schmidt (1959). Kennicutt (1998) analyzed a variety of star-forming galaxies and found a best fit of $n=1.4$. Although the Schmidt law is successful in many star-forming galaxies, it does not apply to dwarf galaxies. In these small objects, the star formation efficiency is much lower than in normal large galaxies. One possibility

is that the velocity dispersion to circular velocity ratio is much higher than in normal disk galaxies and thus the time scale for GMC formation is longer.

III) Star formation efficiency. It is observed that star formation proceeds very slowly in local, normal, spiral galaxies. The timescale of gas consumption by star formation $\tau \equiv M_{gas}/\dot{M}_{gas}$ is around $(1-5) \times 10^9$ yr in galaxies like the Milky Way. This low efficiency should be related to the low fraction of gas that can be concentrated into structures which are dense enough to collapse. Though turbulence can promote GMC formation by compressing gas through small scales shocks, it can also increase the effective velocity dispersion, which may balance the large-scale gravitational instability and suppress the global GMC formation efficiency. In addition, radiation and other kinds of energy feedback from young stars may also be able to dissociate the GMCs and reduce their formation efficiency.

IV) Initial mass function (IMF). The initial mass function describes the mass spectrum with which stars form. Based on observations in the solar neighborhood, Salpeter (1955) first estimated the IMF as,

$$F(m)dm \propto m^{-\alpha} dm, \quad (1.33)$$

with $\alpha = 1.35$ for stars in the mass range $0.4M_{\odot} < m < 10M_{\odot}$. $F(m)dm$ determines the relative number of stars born with masses in the range $m - m+dm$. Other IMFs, commonly used in the literature, include Miller/Scalo (Miller & Scalo 1979), Scalo (Scalo 1986), Kroupa (Kroupa 2002), and Chabrier (Chabrier 2003). All these IMF are similar at $m > 1M_{\odot}$, but the difference at the low mass end is very significant. We adopted the Chabrier IMF for this work. This IMF is estimated from different stellar components in the Galaxy, including disk stars, bulge stars and stars in young and globular clusters. Compared to the Salpeter IMF, the Chabrier IMF yields fewer low-mass stars per unit mass converted into stars.

1.4.3 Satellite galaxies in clusters

In the hierarchical formation scenario, larger structures form in part by accretion of smaller objects which formed earlier. After dark matter halos merge into a larger system, the galaxies within them enter the larger system and orbit as satellites. The evolution of galaxies in clusters is quite different from that in the field. For example, the blue galaxy fraction is much higher in the field than in clusters. This environmental effect on galaxy evolution can be explored with the help of high redshift observations. Butcher & Oemler (1978) first found evidence that the number of blue galaxies in clusters at $z > 0.2$ is higher than in local rich clusters. This was confirmed by later observations (e.g. Dressler 1980). Besides colors, also star formation rates, morphologies and gas content all appear to be affected by local overdensity. From a theoretical point of view, there are several mechanisms that may account for such effects.

Strangulation and Ram-pressure The pressure from the intra-cluster medium (ICM) may strip a satellite galaxy of its hot gaseous halo which would otherwise cool and replenish the disk of cold, star-forming gas. A consequence is that the galaxy loses its supply of new gas compared to its counterparts in the field. As a result, satellite galaxies experience a decline in star formation and become red over time. This process is called strangulation (Larson et al. 1980). The dynamical pressure from the ICM can be very strong on galaxies moving through it, and may sweep cold gas out of the disk in large clusters, where both

the density of the ICM and relative velocity are very high (Gunn & Gott 1972; Quilis et al. 2000). Star formation ceases even faster in this case which is called ram-pressure stripping.

Tidal Effects and Harassment Tidal effects arise when the external gravitational force exerted on a satellite galaxy is not constant across its diameter. The net effect works as an external force which can remove matter from the satellite. This effect works both on the gas component, by removing gas supply and stopping star formation, and on stars, leading to morphology transformation and stellar mass loss. The cumulative effect of gravitational interactions during multiple high speed encounters (*harassment*) may even destroy galaxy disks (Farouki et al. 1983; Moore et al. 1996).

Merging The orbit of a satellite galaxy spirals into the center of the potential well under the effects of dynamical friction and this may lead to a merger of the satellite galaxy with the central object. Early simulations showed that a merger between two galaxies with comparable mass results in the formation of an elliptical galaxy (Farouki & Shapiro 1982; Barnes 1992, see also Chapter 2). The encounter of two galaxies can also channel their gas into the central region, igniting a starburst. This gas inflow may also fuel a supermassive black hole at the center of the merger remnant, triggering AGN activity.

Most of these processes have been included in our current SAM (Chapter 5). Detailed comparison with observations will help us to understand the relative importance of these physical processes in different environments and at different redshifts.

1.4.4 Chemical evolution

Chemical evolution is important in the study of galaxies for at least three reasons. First, the luminosity and color of stars are affected by their metallicity. The more metal rich, the redder a stellar population is. Secondly, metallicity of hot gas affects the rate at which it can cool. Finally, the dust content of the interstellar medium of a galaxy scales roughly linearly with its metallicity and this determines how much of its star light is absorbed and re-emitted in the infrared.

Primordial gas consists primarily of hydrogen and helium, which was created during the epoch of primordial nucleosynthesis during the first three minute of cosmic history. Most of the metals, defined as elements heavier than helium, are formed by nuclear reactions in stellar interiors. These elements are expelled into the ISM by stellar winds or supernova explosions, which in turn enhance the metallicity of subsequent stellar generations. The relative metallicity in different baryonic components is determined by i) how metals are mixed with cold gas and hot gas after they are expelled from stars; ii) how metals are diluted by the infall of fresh gas; iii) how metals are mixed between merging galaxies. At present, these processes can only be modeled in a pragmatic way.

Metal yields are different for stars with different masses. SNII supernova, which occur when massive stars ($>8M_{\odot}$) experience core-collapse, are primarily responsible for the production of α elements (O, Ne, Mg, Si, S, Ar, Ca, Ti). SNIa supernovae, which originate from the explosion of white dwarfs after accretion of material from a binary companion, dominate the production of iron. Because of the different lifetimes of the progenitor stars along the IMF, the relation between the ratio of α/Fe and the total metallicity can be used to constrain the star formation history of galaxies (Thomas 1999). These two kinds of supernova feedback has been implemented by Nagashima et al. (2005) in their semi-analytic

models to study the metal enrichment of elliptical galaxies.

1.4.5 Feedback

The efficiency with which the baryons are converted into stars reaches its peak in galaxies of characteristic luminosity L_* , and drops towards both lower and the higher masses. The low efficiency can be achieved either by preventing gas from cooling or by reheating and expelling existing cold gas. Three of the most popular mechanisms include supernova feedback, UV reionization and AGN feedback.

1.4.5.1 SN feedback

SN feedback plays a very important role in the formation of dwarf galaxies, for which the potential well is shallow and the ISM is easily ejected from of the galaxy by the energy released by supernova explosions. There is plenty of observational evidence for the existence of supernova driven winds (Martin 1997, 1998, 1999; Ott et al. 2005). Fig. 1.3 shows the starburst galaxy, M82, with its prominent galactic wind. The fraction of the total SN energy converted to the thermal energy of the ISM and to the kinetic energy with which cold gas is blown out of galaxies is determined by the competition between cooling and thermalization of the post-shock gas. Cole et al. (1994) proposed a feedback model, in which the rate of reheating is a strong function of the circular velocity of the host dark matter halo. This model is able to reproduce the flat faint end of the observed galaxy luminosity function.

However, the fate of the ejected gas is still far from clear: De Lucia et al. (2004) studied three models for the ejected gas. These are: the *retention model*, in which the reheated gas is blown into a hot gas halo and then can recool; the *ejection model*, in which gas can be ejected out of the halo and is later re-incorporated after a certain time which is usually related to the dynamical time-scale of the halo; and the *wind model*, a hybrid in which a critical value of the halo circular velocity is set below which the ejection model is applied and otherwise the retention model.

SN feedback is also very important to the formation of Milky-Way like galaxies. It affects the fraction of baryons in the halo that collect into the central galaxy, as well as the angular momentum that they are able to retain during the assembly process. SN feedback is one of the most important possible solutions to the *loss of angular momentum problem* (see also Sec. 1.4.1).

There are two kinds of supernovae in real galaxies: Type I (SNI) and Type II (SNII). The energy released by SNIa and SNII are comparable, while the time delay between the occurrence of these two types is around one Gyr. Current SAMs usually only take into account of the SNII explosion as an instantaneous feedback. In the future a more realistic feedback model should also take into account the SNIa feedback. Another candidate for powering galaxy winds is energy input from stellar winds which is most effective for massive stars, and is accompanied by large amounts of mass loss. Given the observed velocity of stellar winds from OB stars, $\sim 2000\text{km/s}$, the kinetic energy ejected by stellar winds is comparable to that from SN explosions. This effect should also be considered in future work.

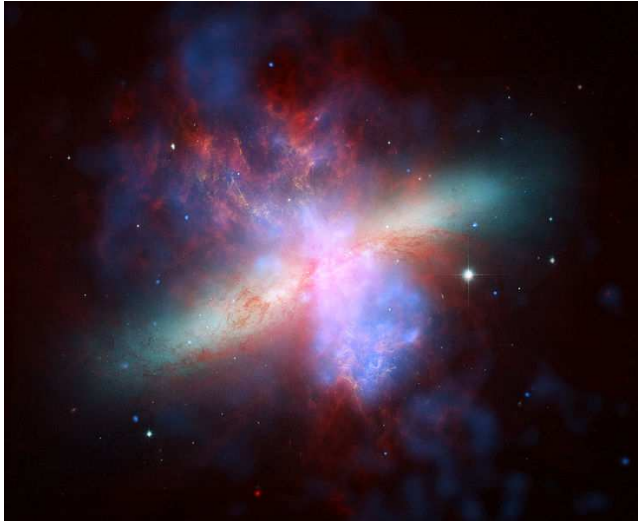


Figure 1.3: A combined Hubble/Spitzer/Chandra image of M82. Hydrogen emission (HST) appear in orange; X-ray data (Chandra) appears in blue; infrared light (Spitzer) appears in red.

1.4.5.2 Reionization

Doroshkevich et al. (1967) first pointed out that high energy background photons have the ability to suppress (or inhibit) galaxy formation in small halos. This idea was later investigated in the context of CDM models by Couchman & Rees (1986). Observations of the Gunn-Peterson trough suggest a lower limit on the reionization epoch at redshift around 6.5 (e.g. Fan et al. 2000, 2006). The cosmological background of ionizing radiation has been dominated by quasars since $z \sim 3$. At earlier times, the observed abundance of bright quasars declines sharply, implying that cosmic hydrogen was probably reionized by stars. Detailed reionization studies involve treatment of the emission mechanisms and statistic properties of the sources, and radiative transfer in the IGM. This must cover scales from small clumps in the ISM, where stars form, to cosmological scale, on which the density field of the IGM can be properly represented. Simulations have been carried out by many authors Gnedin (2000); Miralda-Escudé et al. (2000); Ciardi & Madau (2003); Hoeft et al. (2006); Okamoto et al. (2008).

Usually reionization is included in galaxy formation models as an external input, either analytically (Efstathiou 1992; Thoul & Weinberg 1996; Nagashima et al. 1999) or numerically (Navarro & Steinmetz 1997b; Weinberg et al. 1997; Croton et al. 2006; Somerville & Primack 1999b). One of the most popular models of reionization in SAM (Bullock et al. 2000; Somerville 2002; Croton et al. 2006) was developed by Gnedin (2000). He argued that the characteristic mass, M_c , below which galaxies are strongly affected by photoionization, is equal to the filtering mass, M_f , which corresponds to the scale over which baryonic perturbations are smoothed in linear perturbation theory. Recently, Hoeft et al. (2006) showed that in fact $M_c \ll M_f$, in particular, at low redshift; Okamoto et al. (2008) also found a much lower value for the characteristic mass M_c . The effect of reionization is thus weaker

than Gnedin’s model would imply. Benson et al. (2002) investigated the effect of photoionization on galaxy formation by including the UV photons in a self-consistent way. They argued that reionization is necessary to reproduce the abundance of low mass galaxies in the local universe. In Chapter 5, however, I will show that reionization may not play a role in the formation of any but the very smallest galaxies in the presence of strong SN feedback.

1.4.5.3 AGN feedback

X-ray observations suggest a much higher gas accumulation rate onto galaxies that reside at the cluster centers than is consistent with their observed masses. In fact, these massive central galaxies appear to have formed their stars primarily at very early times. This implies efficient heating processes that can compensate for the cooling expected in massive halos. Suggested explanations have included a constant low density core in the cluster center within which the cooling is inefficient (Cole et al. 2000, though this is inconsistent with the observed X-ray structure), strong SN feedback (Benson et al. 2003; Somerville & Primack 1999b), thermal conduction and superwinds (Benson et al. 2003). More recently, attention has been drawn to the impact of AGN feedback on global galaxy properties. The accretion of matter onto a supermassive black hole (SMBH) can release vast amounts of energy which may reheat/eject gas, suppressing cooling and star formation in galaxies. Clear evidence of interaction between radio lobes and the intracluster gas has been found in X-ray observations of clusters (McNamara et al. 2000, 2005; Fabian et al. 2003). Although it is still not clear exactly *how* AGN feedback operates, it has been proven that AGN feedback would help to reproduce the observed sharp break at L_* in the present-day luminosity function and to solve the *downsizing* problem (stars in massive galaxies are older than in less massive galaxies).

Croton et al. (2006) proposed two modes of AGN activity: the “quasar” mode and the “radio” mode. In “quasar mode”, galaxies merge together and the central black hole of the remnant grows by mergers of the two progenitors’ black holes and by accretion of cold gas from the progenitor galaxies. In “radio mode”, the black hole absorbs hot gas from a surrounding static atmosphere and releases energy back into the hot gas halo, thereby suppressing gas cooling. The efficiency of this mode depends both on the mass of the hot gas and on the mass of the central black hole. Other versions of AGN feedback have been recently included in other semi-analytic models (Bower et al. 2006; Kang et al. 2006; Menci et al. 2006; Monaco et al. 2007; Somerville et al. 2008).

1.4.6 Stellar Population Synthesis

To compare theoretical predictions to observations one needs to calculate the observable properties of the simulated galaxies. This can be done by combining the star formation history predicted by SAM with stellar population synthesis models, which synthesize the spectra of all the stars that have formed, after evolving then to the time under consideration. Compared to all the other processes described above, stellar evolution is reasonably well understood. Galaxy formation modelers usually treat the stellar population synthesis models as trusted black boxes even though there are still, in fact, substantial uncertainties.

In this work, we adopt the stellar population synthesis model of Bruzual & Charlot (2003). This model has a spectral resolution as high as 3\AA .

Dust plays an important role in determining the observed spectrum, especially for young populations that mainly emit in the optical and ultra-violet regions of the spectrum and are still embedded in molecular clouds. A significant fraction of the starlight will be absorbed by dust and re-emitted at infra-red and sub-millimeter wavelengths. The extinction and re-emission depend on the properties of the dust, such as its distribution relative to the stars, and the geometry, the chemical composition, and the size of dust grains, which in turn is determined by gas density, metallicity and other properties. Although the stars and dust are mixed together in reality, it is hard to model this in cosmological semi-analytic models because the inner structure of galaxies is not well resolved. Usually a slab model is assumed, which acts as a screen in front of the stars (Kauffmann et al. 1999; Somerville & Primack 1999b; Croton et al. 2006; De Lucia & Blaizot 2007; Cole et al. 2000). More sophisticated models have also been used, however (Panuzzo et al. 2005, GRASIL). The re-emission of dust grains has been modeled in a semi-analytic way (Kaviani et al. 2003; Guiderdoni et al. 1998; Devriendt & Guiderdoni 2000; Granato et al. 2000). Baugh et al. (2005) devised a model which successfully reproduces the local galaxy luminosity function in the optical and infrared bands, and is consistent with the very high observed number density of sub-millimeter and infrared luminous galaxies at high redshifts. This required them to assume a very different IMF at high redshifts. I will show below that with a redshift-dependent dust model but with a constant IMF we are able to reproduce most properties of three high redshift galaxy populations: the Lyman-Break Galaxies, the BX Galaxies (star forming galaxies at $z \sim 2$) and Distant Red Galaxies.

1.5 Outline

This thesis addresses four areas of galaxy formation: i) the galaxy formation efficiency as a function of dark matter halo mass; ii) the roles which mergers and star formation play in the growth of galaxies, in comparison with the growth of dark matter halos; iii) the predictions of current galaxy formation models at high redshift; iv) the role SN feedback plays in shaping the low mass end of the stellar mass function and in solving the “missing satellite” problem.

Chapter 2 and Chapter 3 are both based on a public model galaxy catalogue ¹ which was calculated by implementing galaxy formation models on the Millennium Simulation. The stellar masses of galaxies increase through three processes, major mergers, the accretion of smaller satellite systems, and star formation. In Chapter 2, I study the relevant roles of these three processes in stellar mass growth as a function of stellar mass and redshift. For comparison, a similar analysis is carried out for the growth of dark matter halos. I will show that mergers are more important for halo growth than for galaxy growth, except for the formation of very massive galaxies. In Chapter 3 I shift the focus to three particular high redshift galaxy populations. I build up a mock catalogue and select simulated galaxies according to exactly the same criteria used by observers. Most of the observational properties, including the color, number density and redshift distribution, as well as their

¹<http://www.mpa-garching.mpg.de/millennium>

spatial distribution are well reproduced provided I introduce a new dust model. I further use the model to interpret the physical properties of these populations and to predict their evolution to lower redshift.

In Chapter 4, I use the stellar mass function of Li & White (2009) based on Sloan Digital Sky Survey data and the dark matter halo mass function derived from the Millennium Simulation I and Millennium Simulation II, two large volume, high resolution simulations, to establish the relation between the stellar mass of a galaxy and the maximum mass ever attained by its halo assuming a monotonic correspondence between these two quantities. This relation can be used to constrain efficiency of galaxy formation, as well as to assess the realism of simulations of individual galaxies. I compare the predicted halo masses of galaxies with given stellar masses with the measurements from weak lensing. I also study the “Tully-Fisher” relations for stellar mass and compare it with the observations in order to test whether the Λ CDM model can reproduce the luminosity function and Tully-Fisher relation simultaneously.

Although the galaxy formation model used in Chapter 2 and Chapter 3 is successful in reproducing many galaxy properties both in the local universe and at the high redshift, it overpredicts the number density of low mass ($\sim 10^8 M_\odot$) galaxies at $z \sim 0$ by a factor of 3 compared to the most recent SDSS DR7 data. In Chapter 5, I revisit the galaxy formation model, mainly focusing on the SN feedback, on the treatment of satellite galaxies in clusters and on the angular momentum transfer. The new galaxy formation model is implemented on the combination of MS-I and MS-II. This makes it possible to study galaxy formation all the way from the giant cD galaxies in cluster cores to dwarf galaxies as faint as the faintest Milky Way satellites. This has not been possible in previous work. I will discuss how the new model reproduces the abundance of low mass galaxies, their color distribution, the mass function of satellite galaxies in Milky-Way-like systems and also in clusters, and I will show how its limited resolution affects predictions made using the Millennium Simulation I only.

A brief summary is represented in Chapter 6, as well as an outlook for future work.

Galaxy growth in the concordance Λ CDM cosmology

Abstract

We use galaxy and dark halo data from the public database for the Millennium Simulation to study the growth of galaxies in the De Lucia et al. (2006) model for galaxy formation. Previous work has shown this model to reproduce many aspects of the systematic properties and the clustering of real galaxies, both in the nearby universe and at high redshift. It assumes the stellar masses of galaxies to increase through three processes, major mergers, the accretion of smaller satellite systems, and star formation. We show the relative importance of these three modes to be a strong function of stellar mass and of redshift. Galaxy growth through major mergers depends strongly on stellar mass, but only weakly on redshift. Except for massive systems, minor mergers contribute more to galaxy growth than major mergers at all redshifts and at all stellar masses. For galaxies significantly less massive than the Milky Way, star formation dominates the growth at all epochs. For galaxies significantly more massive than the Milky Way, growth through mergers is the dominant process at all epochs. At a stellar mass of $6 \times 10^{10} M_{\odot}$, about that of the Milky Way, star formation dominates at $z > 1$ and mergers at later times. At every stellar mass, the growth rates through star formation increase rapidly with increasing redshift. Specific star formation rates are a decreasing function of stellar mass not only at $z = 0$ but also at all higher redshifts. For comparison, we carry out a similar analysis of the growth of dark matter halos. In contrast to the galaxies, growth rates depend strongly on redshift, but only weakly on mass. They agree qualitatively with analytic predictions for halo growth.

2.1 Introduction

Galaxy mergers play an important role in galaxy formation and evolution. They add new gas and stars. They drive gas motions which feed starbursts and central supermassive black holes, and, for comparably massive systems, they entirely restructure both galaxies. Toomre (1976) was the first to stress that the abundance of tidally distorted spirals in the nearby universe suggests that “star piles” produced by past interactions might account for the majority of observed elliptical galaxies. White (1978) carried out the first

dynamically consistent 3-dimensional simulations showing that mergers do indeed produce remnants with a structure similar to that of ellipticals, a conclusion which has been reinforced by increasingly realistic simulations of purely stellar systems (Farouki & Shapiro 1982; Barnes 1988; Naab & Burkert 2003). Inclusion of the gas component showed that a substantial fraction of the interstellar medium should be driven to the centre in major mergers (Negroponte & White 1983; Barnes & Hernquist 1991; Mihos & Hernquist 1996). This work supported the identification of ultraluminous infrared galaxies as merging systems (Sanders et al. 1988) but led to remnant galaxies with cores which are denser than observed ellipticals. Recent work suggests that this contradiction may be resolved by strong AGN- or starburst-generated winds which expel a large fraction of the gas from the galaxy (Springel et al. 2005a; Di Matteo et al. 2005). Work on mergers of unequal galaxies suggests that while such mergers may not greatly alter the structure of the larger system (Velazquez & White 1999; Abadi et al. 2003) they can nevertheless stimulate substantial rearrangements of its gas with associated star formation and AGN activity (Mihos & Hernquist 1994).

In the standard Λ CDM cosmology structure forms hierarchically. Small dark matter halos form first and then aggregate into progressively larger systems. At any given time cosmic matter is distributed over nonlinear objects spanning many decades in mass, and growth is driven by merging with similar halos, by accretion of much smaller halos and of diffuse material, and by destruction by infall onto larger halos (e.g. Lacey & Cole 1993). The situation is made more complex by the fact that the inner cores of halos often survive as long-lived substructure within the larger objects by which they are accreted (Ghigna et al. 1998; Moore et al. 1999; Gao et al. 2004). Galaxies form at the centres of halos in the way suggested by White & Rees (1978) and are swept along with the growth of dark matter structure. They gain stars through formation from their interstellar medium, which may be replenished by infall from their surroundings, and by incorporating the stars of galaxies which merge with them. The interaction between these processes drives the overall evolution of the population and cannot be followed without treating the associated baryonic astrophysics (gas condensation, formation and evolution of stars and black holes, feedback from supernovae and AGN, chemical enrichment, production of observable radiation etc.).

Early studies of the evolution of the galaxy population embedded simplified treatments of this baryonic physics in Monte Carlo realisations of the merger trees associated with the formation of individual dark halos (Kauffmann et al. 1993b; Cole et al. 1994, 2000; Somerville & Primack 1999b). The spatial distribution of galaxies could then be studied using the halo distribution from an N-body simulation of structure formation (Kauffmann et al. 1997; Benson et al. 2000). Improvements on this scheme have used higher resolution N-body simulations so that the merging trees can be taken directly from the simulation itself, thereby allowing the evolution of the galaxy population to be followed in a single consistent simulation (Kauffmann et al. 1999; Springel et al. 2001; Helly et al. 2003; Hatton et al. 2003; Springel et al. 2005b; Kang et al. 2005). A parallel approach has followed the dynamics of diffuse gas (in particular, aspects of the gas condensation and galactic wind processes) by adding a hydrodynamic scheme to the N-body treatment of dark matter while continuing to treat star formation and evolution by semi-analytic means (Cen & Ostriker 1992; Navarro & White 1994; Katz et al. 1996). The development path here has involved continual improvement of the simulation schemes to increase resolution and to treat the

accessible physics more realistically (e.g. Cen & Ostriker 2000; Springel & Hernquist 2003; Pfrommer et al. 2006). Recent work in both approaches has focussed on how feedback from AGN may regulate the formation and evolution of their host galaxies (Springel et al. 2005a; Di Matteo et al. 2005; Croton et al. 2006; Bower et al. 2006).

This body of work has demonstrated that while galaxy mergers are an important aspect of the evolution of the galaxy population, they do not simply parallel the mergers of dark halos. As White & Rees (1978) stressed, galaxies must remain distinct after the merger of their halos if we are to understand the formation of galaxy clusters. Fall (1979) noted that late-type giant galaxies cannot have undergone recent major mergers since these would destroy their stellar disks. While many more recent studies have followed Toomre (1976) in arguing that massive elliptical galaxies assembled relatively recently through mergers (e.g. Kauffmann & Charlot 1998; van Dokkum 2005; De Lucia et al. 2006) other authors have used the age and uniformity of their stellar populations and their apparently undiminished abundance at high redshift to argue against such late assembly (e.g. Cimatti et al. 2006). Observational estimates of merging rates, based primarily on counts of very close pairs of galaxies, or of morphological evidence for recent merging, have varied widely due to uncertainties in the associated timescales (Le Fèvre et al. 2000; Lin et al. 2004). In addition, attempts to measure the evolution of the merger rate, usually parametrised as proportional to $(1+z)^\alpha$ have obtained values for the exponent α ranging from 0 to 6. (Bell et al. 2006; Carlberg et al. 2000; Patton et al. 2002; Conselice et al. 2003; Bundy et al. 2004; Lin et al. 2004).

In the present paper we analyse the build-up of the galaxy population in the galaxy formation model of De Lucia & Blaizot (2007) which is implemented on very large Millennium Simulation (Springel et al. 2005b). This model updates that of Croton et al. (2006) and is a reasonable match to the clustering and to many of the systematic properties of the local galaxy population. It is also consistent with most available data at high-redshift (Kitzbichler & White 2007). For our purposes, this provides a physically consistent and observationally plausible implementation of galaxy formation within the dynamical framework of Λ CDM. It can therefore be used to explore the differences between galaxy growth and dark halo growth in this structure formation model. We use the public database containing the properties of the dark halos and the galaxies¹ to construct mean growth rates for galaxies through major mergers, through minor mergers and through star-formation, each as a function of galaxy mass and of redshift, and we compare these with analogously defined growth rates for dark halos.

Our paper is organized as follows. In Sec. 2.2 we introduce the *Millennium Run* and the prescriptions used to simulate galaxy formation using merger trees built from it. Sec. 2.3 presents our analysis of the mass and redshift dependence both of the major merger rate and of growth rates through major and minor mergers as well as through star formation. In Sec. 2.4, we discuss the corresponding properties of dark halos (defined here as FOF groups) and contrast them with our results for galaxies. Conclusions and discussions are presented in Sec. 2.5.

¹<http://www.mpa-garching.mpg.de/millennium>

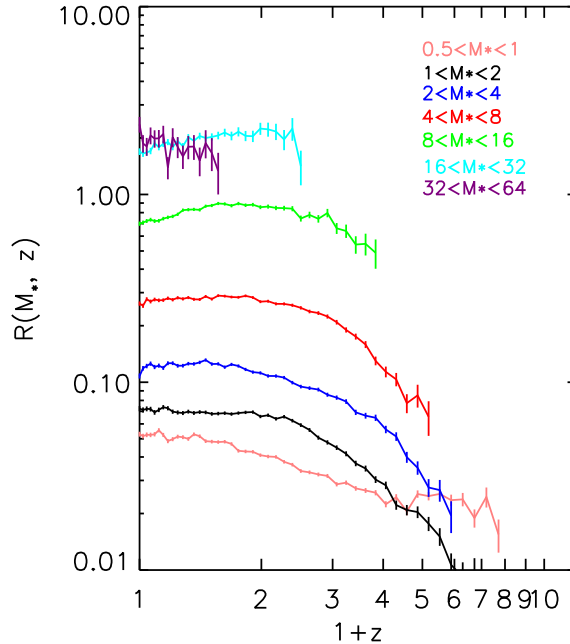


Figure 2.1: The specific rate of formation of galaxies through major mergers as a function of redshift. The 7 curves refer to product galaxies with stellar mass in 7 disjoint ranges, identified by labels with units of $10^{10} M_{\odot}$. A galaxy is considered to have just formed through a major merger if its two largest progenitors in the preceding Millennium Run output differ by less than a factor of 3 in stellar mass. The dimensionless measure of merger rate used here is the fraction of all galaxies in the given stellar mass bin at redshift z which form through a major merger per unit time, multiplied by the age of the Universe at redshift z . Error bars give Poisson uncertainties derived from the number of new merger products in each bin at each redshift. The probability that a galaxy has just formed through a major merger is a strong function of stellar mass, but a weak function of redshift.

2.2 The simulation and the galaxy formation model

The galaxy catalogue used in this paper was produced using a “hybrid technique: a large N-body simulation was first carried out to define the evolution of the dark matter distribution, and then a suite of semi-analytic prescriptions was implemented in order to simulate the formation and evolution of galaxies within a stored “forest” of (sub)halo merging trees constructed from the original simulation. A detailed description of the *Millennium Simulation* and of the galaxy formation model can be found in (Springel et al. 2005b; Croton et al. 2006; De Lucia & Blaizot 2007). Here we summarize the main simulation characteristics and the way the halo merger trees were constructed, as well as those aspects of the galaxy formation modelling that are relevant to our study of galaxy growth.

2.2.1 The simulation

The *Millennium Simulation* (Springel et al. 2005b) used in this study is one of the largest simulations of cosmic structure evolution to the present day so far carried out. It adopts the concordance Λ CDM cosmology and follows $N = 2160^3$ particles from redshift $z = 127$ to $z = 0$ in a comoving box of side-length 685 Mpc. This volume is large enough to investigate rare objects such as quasars and rich clusters of galaxies, yet, has a dark matter particle mass of only $8.6 * 10^8 M_{\odot}$, allowing the galaxy formation model to follow the formation of all galaxies more massive than the Small Magellanic Cloud. The assumed cosmological parameters are $\Omega_m = 0.25$, $\Omega_b = 0.045$, $h = 0.73$, $\Omega_{\Lambda} = 0.75$, $n = 1$, and $\sigma_8 = 0.9$, where the Hubble constant is parameterized as usual as $H_0 = 100h \text{kms}^{-1} \text{Mpc}^{-1}$. These parameters are consistent with a combined analysis of the 2dFGRS (Colless & et al. 2001) and the first-year WMAP data (Spergel et al. 2003).

During the simulation, the full particle data were stored at 64 output times approximately logarithmically spaced from $z = 20$ until $z = 2$ and at approximately 300 Myr intervals thereafter. At each time, the simulation code produced a friends-of-friends group catalogue on the fly by linking together particles separated by less than 0.2 of the average interparticle separation (Davis et al. 1985). Subsequently, the SUBFIND algorithm (Springel et al. 2001) was used to divide each FOF group into a disjoint set of self-bound subhalos. These subhalos are the basis for the merger trees, which are defined by linking each subhalo from a given output time to one and only one descendent at the following output time. When studying the growth of dark halos in Sec. 2.4, we define a halo as an FOF group and we estimate its mass as the sum of the masses of all its subhalos. This typically loses a small amount of “diffuse” material which was bound to none of the subhalos. This is not significant for our purpose here, and this definition was convenient, since the original FOF halo mass was not stored in the (sub)halo database when we carried out this project. More importantly, this mass definition allows us to deal in a straightforward way with the problem that simulated halos, unlike our simulated galaxies or the halos considered in simplified models for halo growth, not only merge but can also fragment. Mass from a single FOF halo can thus contribute to several FOF halos at some later time.

2.2.2 Merger rates

In the galaxy formation models implemented on the Millennium Simulation, a galaxy begins to condense at the centre of a halo as soon as it is identified as a persistent object with more than 20 dark matter particles. As the halo grows, so does the galaxy at its centre, forming stars at a rate governed by its cold gas content and by empirically determined star formation “laws”. The halo may merge into a larger system, becoming an independent subhalo orbiting within the FOF group. The galaxy is now considered a satellite, losing its supply of fresh gas, and perhaps ceasing to form stars if it uses up its available interstellar medium. Dynamical friction effects bring the orbit of the subhalo ever closer to the centre of its parent, and tidal effects strip away its outer regions until eventually it may be disrupted entirely (or at least drop below the resolution limit of the simulation). At this point the galaxy is associated to the most-bound particle of the subhalo at the last time it was identified and is marked as a candidate for merging with the central galaxy of the parent

halo. The merger takes place one estimated dynamical friction time later.

Galaxy mergers may trigger strong star formation. In the galaxy formation model of Croton et al. (2006) and De Lucia & Blaizot (2007) which we analyse here, a recipe similar to that of Somerville et al. (2001) is adopted to describe starbursts during minor mergers. In this model, a fraction e_{burst} of the cold gas of final galaxy is converted into stars, where

$$e_{burst} = 0.56 * \left(\frac{M_{satellite}}{M_{central}} \right)^{0.7}.$$

A major merger is assumed to occur whenever the two galaxies differ by a factor of less than 3 in baryonic mass. In such a merger the starburst is assumed to convert a large fraction of the cold gas into stars and to eject the rest from the galaxy. The remnant of such a merger is assumed to be an elliptical galaxy. It may, however, grow a new disk if gas is able to cool from the surrounding halo, and in this case the merged system becomes the bulge of a larger spiral galaxy.

In this galaxy formation model, central galaxies are treated differently than satellites. Only central galaxies are fed new material by cooling from the hot atmosphere of their halo, by direct infall of cold gas, or by merging of satellites. No new material accretes onto satellite galaxies, so that their star formation terminates when their cold gas is used up. Gas accretion processes depend strongly on time and on galaxy mass. At early times and in low-mass galaxies gas cools substantially more efficiently than in high-mass systems and at late times. In addition, an important innovation in the model of Croton et al. (2006) (and included here) is a treatment of “radio mode” feedback. This assumes that if the central galaxy has a supermassive black hole and sits at the centre of a static hot atmosphere, then radio activity will prevent further cooling of hot gas. This resolves the long-standing “cooling flow problem” and ensures that a massive elliptical at the centre of a group or cluster does not grow a new disk and so remains “red and dead”. As a result the only significant growth mode for high mass galaxies is through merging.

In this study, we consider all galaxies in the Millennium/DeLucia database with stellar mass between $5 \times 10^9 M_{\odot}$ and $6.4 \times 10^{11} M_{\odot}$. Although the galaxy catalogues are nearly complete to a mass at least 5 times lower than this, we want to be able to resolve the recent merging history of each system and so we adopt this more conservative limit. This choice leaves us with a total 81896686 galaxies (summed over all redshifts). To investigate the mass dependence of galaxy growth, we divide this sample into seven mass bins, each a factor of 2 wide. The highest mass bin contains the smallest number of galaxies, a total of 22827 systems.

2.3 Galaxy growth rates

Growth in the stellar mass of galaxies occurs through two processes: conversion of gas into stars (either quiescently or in a starburst) and the addition of stars through mergers. In this section we mine the publicly available database to study the interplay between these processes. We begin by studying how the rate of major mergers depends on the mass of the product galaxy and on redshift. We then compare mean galaxy growth rates due to this process to mean growth rates due to all mergers (major and minor) and to star formation.

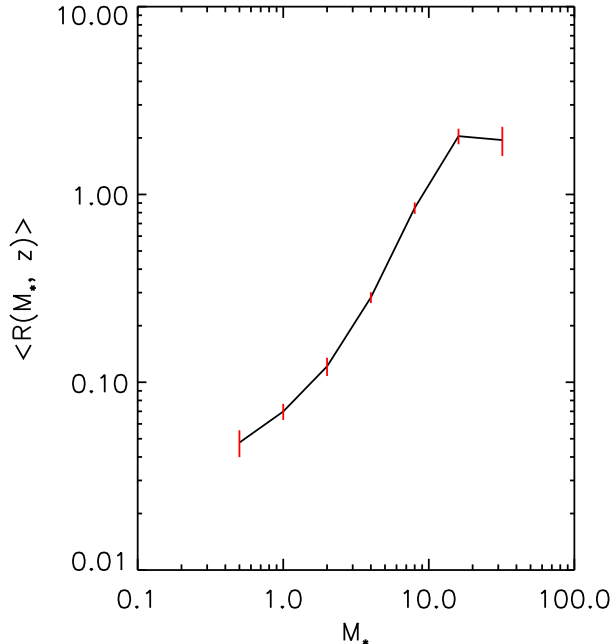


Figure 2.2: The relation between the stellar mass of galaxies and their specific formation rate through major mergers. The rates given here average the data plotted in Fig. 1 over the redshift range $0 \leq z \leq 2$ (except for the highest stellar mass bins where there are insufficient objects to determine a rate at the higher redshifts). The error bars indicate the *rms* fluctuation in rate over these redshift intervals. Clearly, the probability that a galaxy has just formed through a major merger increases approximately linearly with stellar mass in this galaxy formation simulation.

For each galaxy in the database at each time, we define the main progenitor at the previous stored time to be the progenitor with the largest stellar mass. If a galaxy has more than one progenitor at the earlier time, then it has undergone a merger between the two times. If m of the other progenitors differ from the main progenitor by less than a factor of 3 in stellar mass, then the galaxy is assumed to have had m major mergers in this time interval.

We define a dimensionless major merger rate per galaxy as a function of redshift and stellar mass through

$$R(M_*, z) = \frac{N_{major}(M_*, z)/\delta t(z)}{N_{gal}(M_*, z)/t(z)} \quad (2.1)$$

where $N_{gal}(M_*, z)$ is the number of galaxies in the simulation at redshift z and with stellar mass in a chosen interval centred on M_* , $N_{major}(M_*, z)$ is the number of these galaxies which have had a major merger since the last stored redshift $z_p(z)$ (a galaxy which has had m major mergers is counted m times), $\delta t(z)$ is the time interval between z_p and z and $t(z)$ is the age of the universe at z . Hence $R(M_*, z)$ is the fraction of galaxies of stellar mass

M_* formed per Hubble time through major mergers at redshift z .

Fig. 2.1 shows major merger rates estimated in this way as a function of redshift for seven intervals of stellar mass, each a factor of 2 wide. We plot Poisson errors on our estimates which are determined entirely by the number of merger remnants $N_{major}(M_*, z)$ found at each time. At low redshift ($z < 2$) our dimensionless rate depends remarkably weakly on redshift. For most stellar masses, any variation is within the noise. At high redshift we see a decline in merger rate for all but the highest masses. On the other hand the dependence of $R(M_*, z)$ on stellar mass is very strong. The probability of formation through major mergers is about 40 times higher for the most massive galaxies we consider than for the least massive galaxies. Galaxies comparable in mass to our Milky Way ($\sim 6 * 10^{10} M_{sun}$) form through major mergers at a rate of about 25% of the population per Hubble time, while for galaxies with a stellar mass $\sim 4 \times 10^{11} M_{\odot}$ the corresponding rate is about 8 times higher.

To see more clearly the stellar mass dependence of the specific rate of formation through major mergers, we plot in Fig. 2.2 the relation between $\langle R(M_*, z) \rangle$ and stellar mass. Here we have averaged the data of Fig. 2.1 over the redshift interval from $z = 2$ to 0 (or, for massive galaxies, over redshifts where there are more than 15 major mergers in total). Error bars show the *rms* variation in the rate over the redshift range used. The relative formation rate through major mergers is approximately proportional to stellar mass $\langle R \rangle \propto M_*$, although the plot suggests a more complex behaviour with an initial steepening towards higher mass followed by a (possible) saturation at the highest mass.

Galaxies grow not only through major mergers, but also through minor mergers and through star formation. In order to compare the relative importance of these processes, we now calculate mean growth rates for galaxies in each of these channels as a function of stellar mass and redshift. In analogy to equation (1) we define mean dimensionless growth rates due to major mergers, to all mergers and to star formation as

$$R_{m,major}(M_*, z) = \frac{M_{major}(M_*, z)/\delta t(z)}{M_{gal}(M_*, z)/t(z)} \quad (2.2)$$

$$R_{m,merger}(M_*, z) = \frac{M_{merger}(M_*, z)/\delta t(z)}{M_{gal}(M_*, z)/t(z)} \quad (2.3)$$

$$R_{m,gas}(M_*, z) = \frac{M_{gas}(M_*, z)/\delta t(z)}{M_{gal}(M_*, z)/t(z)} \quad (2.4)$$

where $M_{gal}(M_*, z)$ is the total stellar mass of all galaxies at redshift z with individual stellar masses in the bin centred on M_* , and M with subscripts ‘major’, ‘merger’ and ‘gas’ indicates the total stellar mass added to the main progenitors of these galaxies since the previous output time through major mergers, all mergers and star formation, respectively. This includes star formation over this time interval in all the progenitor galaxies, as well as in quiescent and in merger-related starburst modes. $\delta t(z)$ and $t(z)$ have the same meaning as before. These rates represent the recent growth of galaxies *prior* to the time they are observed in terms of the fractional increase in their stellar mass per current Hubble time occurring in each of the three modes. For example, $R_{m,gas} > 1$ represents a class of galaxies whose recent average star formation rate exceeds their past average star formation rate.

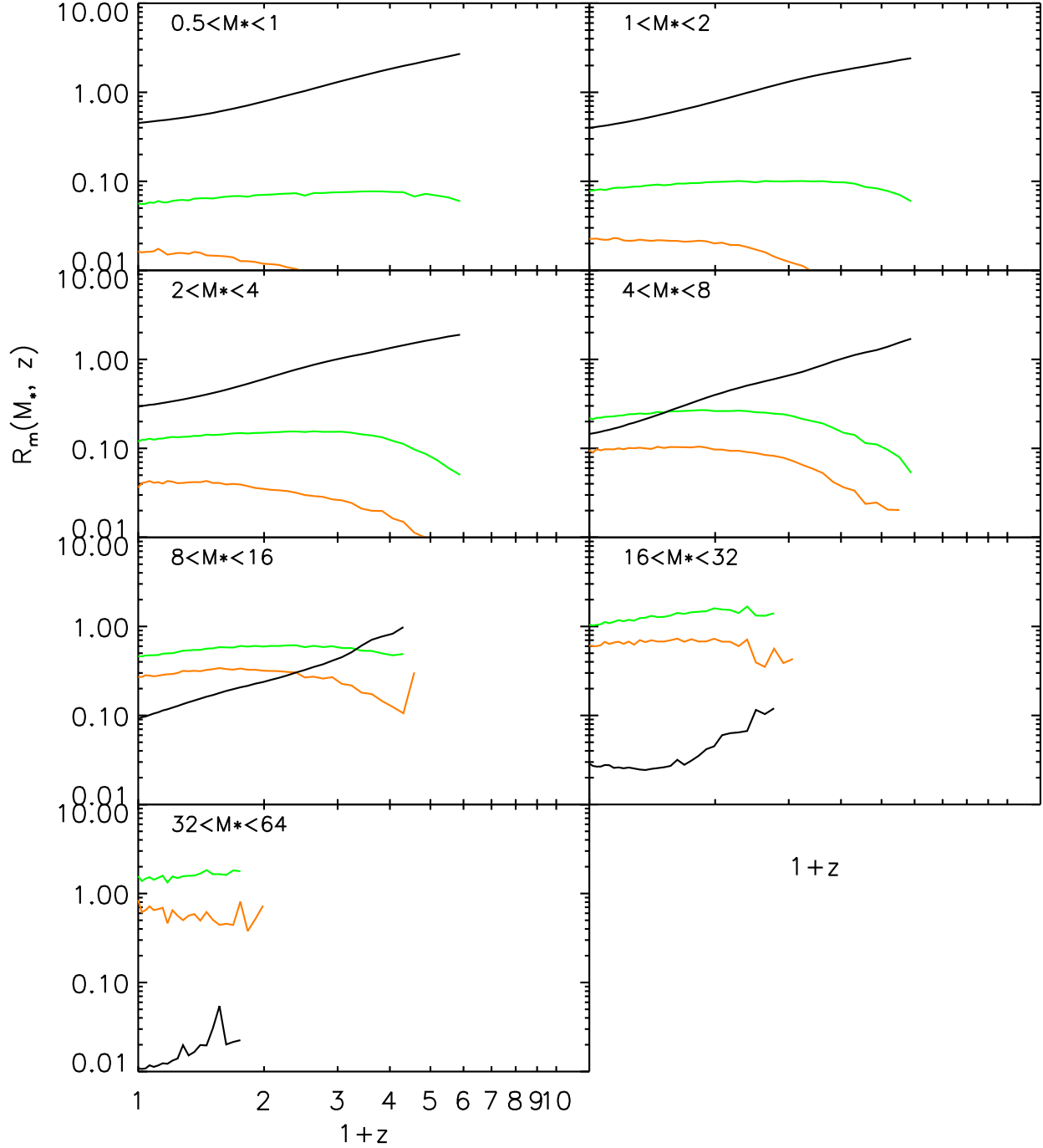


Figure 2.3: Dimensionless mean growth rates for galaxies as a function of redshift for the 7 different stellar mass bins of Fig. 1 and for different growth modes. For each galaxy at each output time, the fraction of its stellar mass gained in a particular mode since the previous output is divided by the time between outputs and multiplied by the current age of the Universe. The result is then averaged over all galaxies in the chosen mass bin and plotted against output redshift. The different curves represent stellar mass growth through major mergers (orange) through all mergers (green) and through star formation (black). The stellar mass ranges in the labels for each panel are given in units of $10^{10} M_{\odot}$.

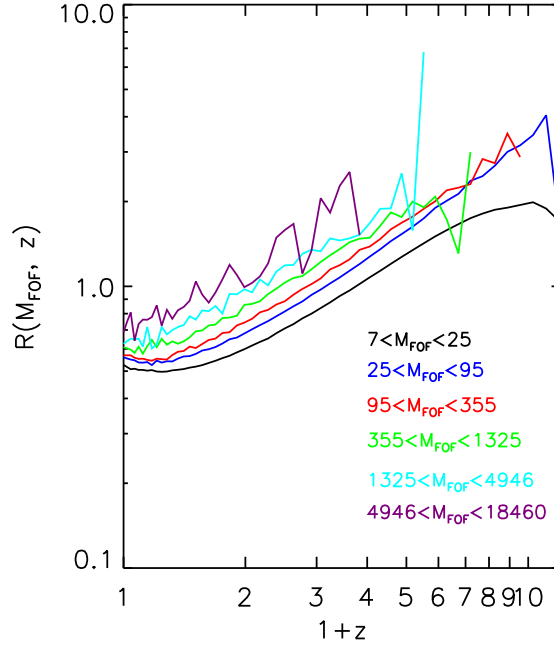


Figure 2.4: For comparison with Fig. 2.1 we plot redshift against the specific formation rate of FOF groups through major mergers, averaged over groups in 6 different mass bins as indicated by label color. The mass unit here is $10^{10} M_{\odot}$.

In Fig. 2.3 we plot these growth rates as a function of redshift for the same 7 bins of stellar mass already illustrated in Fig. 2.1. The orange curves give the dimensionless growth rate through major mergers and so are very similar to the curves already plotted in Fig. 2.1. Indeed, the ratio of the two is just the average of the ratio of the stellar mass of the smaller galaxy in a major merger to the stellar mass of the merger product. Thus, the dimensionless growth of galaxies through major mergers also depends little on redshift but strongly on stellar mass (as in Fig. 2.2). Only for the most massive galaxies does R_{major} approach unity; for galaxies of Milky Way mass it is around 10% at all redshifts.

The green curves in Fig. 2.3 give mean growth rates due to all mergers. For all but the more massive galaxies at the lowest redshifts, these curves lie more than a factor of 2 above the major merger curves. The difference between the two curves increases with increasing redshift in all cases. Thus, minor mergers are generally *more* important for increasing the stellar mass of galaxies than are major mergers. For small mass galaxies at high redshift the ratio of the two growth rates can be an order of magnitude. For galaxies with masses above $10^{11} M_{\odot}$ (in the model this represents the classical giant elliptical population) merging dominates the growth rates at redshifts $z < 2$, and major mergers account for more than half of the total stellar mass growth at low redshifts. In the highest stellar mass bin the relative importance of major and minor mergers is slightly different; these objects are the Brightest Cluster Galaxies investigated in detail by De Lucia & Blaizot (2007).

Finally, the black curves in Fig. 2.3 give mean growth rates due to star formation as a function of redshift. These are constructed by averaging *all* the star formation between two output times in *all* the progenitors of the galaxies in each mass bin. As a result, they include quiescent star formation both in the main galaxies and in smaller galaxies which merge with them, as well merger-induced starbursts. Unlike the growth rates due to mergers, they increase monotonically and relatively steeply towards high redshift, roughly as one power of $(1+z)$ on average, although the slope decreases with redshift at low stellar mass and increases with redshift at high stellar mass. At the present day $R_{m,gas}(M_*, 0)$ is a decreasing function of M_* and is always below unity. Thus, galaxies of all stellar masses are, on average, currently forming stars at less than their past average rate. For galaxies of Milky Way mass, the mean star formation rate at $z = 0$ is about 15% of the past average; this ratio drops to very small values for more massive systems.

This behaviour is well known in the real Universe and is often taken as evidence for “downsizing”; massive galaxies seem to complete most of their star formation at higher redshift than low mass systems. Somewhat surprisingly, however, this ranking of dimensionless growth rate holds at *all* redshifts, not just at $z = 0$. In this model there is *no* redshift at which high stellar mass galaxies are growing faster (in relative terms) than less massive systems. Except for the highest mass bin (where galaxies form almost exclusively through multiple mergers) the dimensionless growth rates due to star formation exceed unity at sufficiently high redshift for galaxies of all stellar mass. This remains true to lower redshift for lower stellar mass.

If we compare the mean growth rates due to star formation with those due to (all) mergers, we see that, except at the highest stellar masses, star formation dominates at sufficiently high redshift. This is true all the way down to $z = 0$ for galaxies less massive than the Milky Way, but for higher mass systems mergers are the dominant growth mode at low redshift. It is interesting that the Milky Way mass, which is also approximately the characteristic stellar mass at the knee of the galaxy luminosity function, marks the boundary between the two regimes. This is not a coincidence. It is built into the model by the physical assumptions required to get a good fit to the observed galaxy luminosity function. In low-mass systems cooling is very efficient and supernova feedback has to be invoked to prevent overproduction of stars. Even with such feedback, a significant fraction of the baryonic material gained by small halos is turned into stars, and most of this accreted material is associated with objects which were too small to contain stars of their own. Hence star formation is a more effective growth mode than merging. At Milky Way mass, cooling is still efficient, particularly at early times, and supernova feedback is less effective in preventing star formation. On the other hand, much of the infalling material is in objects which are massive enough to contain substantial numbers of their own stars. Thus stellar mergers become competitive with star formation. For higher stellar masses, the model invokes “radio mode” AGN feedback to suppress cooling and star formation. The steep quasi-exponential tail of the stellar mass function is then populated almost exclusively by mergers.

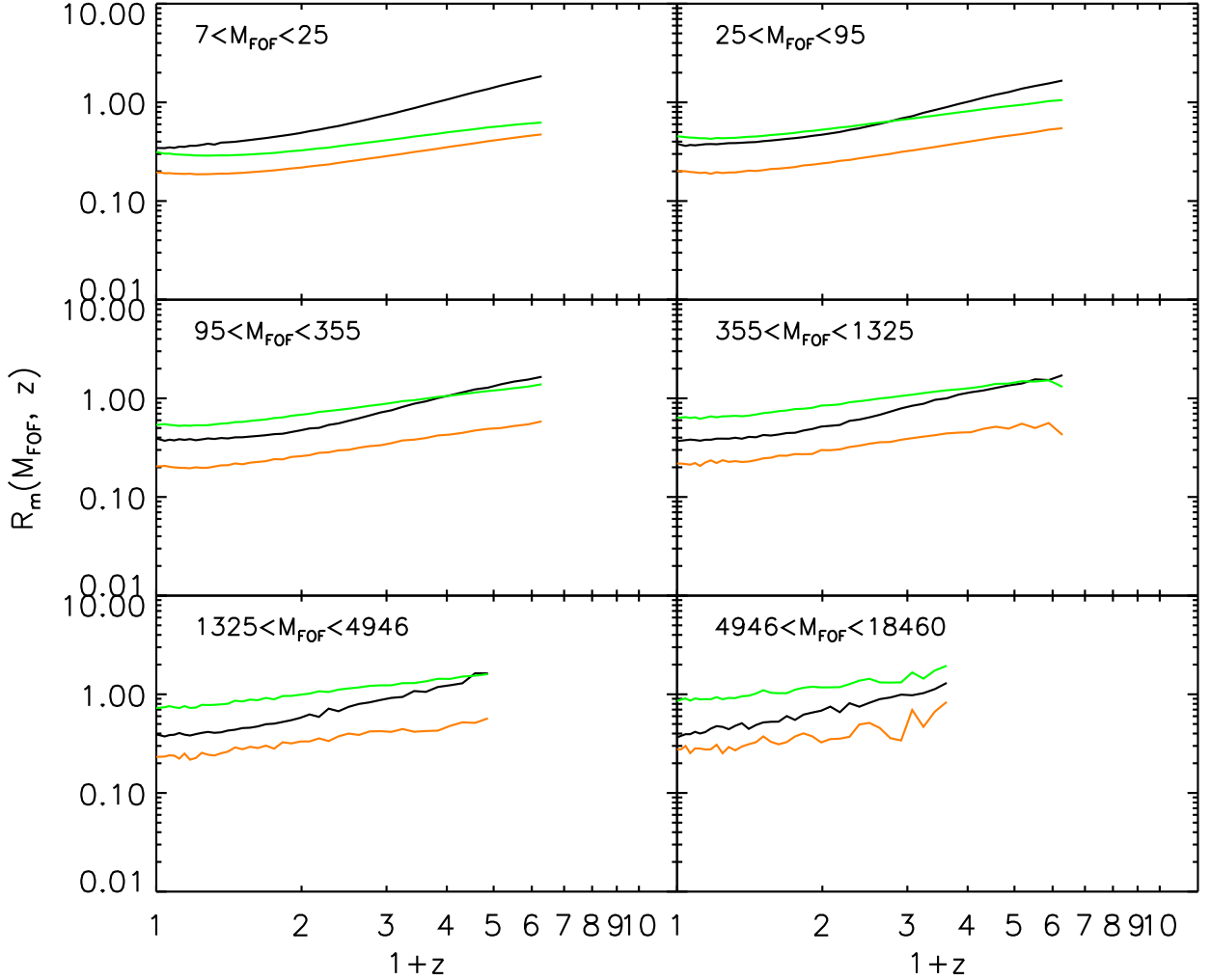


Figure 2.5: For comparison with Fig. 2.3, we plot dimensionless mass accretion rates for FOF groups as a function of redshift for the same 6 mass bins as in Fig. 2.4. The different curves give the mean mass accretion rate due to major mergers (orange), to all mergers (green) and to accretion of diffuse particles (black). The mass unit for the labels in each panel is $10^{10}M_{\odot}$.

2.4 Growth Rates for FOF groups

As discussed in Sec. 2.1, the relation between galaxy mergers and mergers of their host halos is less straightforward than one might expect. In this section we investigate merger and growth rates for dark halos in a way which allows direct comparison with the results presented for galaxies above. For the purposes of our study it is convenient to identify dark halos as the friends-of-friends (FOF) groups initially identified in the Millennium Simulation, and to approximate the mass of each FOF group by the sum of the masses of

its identified subhalos. This loses the mass of a certain number of “diffuse” particles which are not bound to any subhalo, but this systematic is relatively small for most halos and is of no consequence for our analysis. This scheme provides a straightforward way for us to deal with the problem that simulated halos, unlike those in extended Press-Schechter models (e.g. Lacey & Cole 1993) or the galaxies discussed above, often fragment into pieces which can become parts of different halos at a later time. This means that the progenitors of an FOF halo may include only part of an earlier FOF halo. Tracking individual subhalos allows us to account for this, since the Millennium halo database is set up so that each subhalo has a unique descendent, ensuring that the progenitors of an FOF group are a unique set of subhalos which may form all or part of several FOF halos.

We bin the FOF groups at each redshift according to mass, with each bin spanning a factor of 3.8 in mass. The six bins for which we present results then correspond very roughly to halos whose central galaxies lie in the upper six stellar mass bins of figures 2.1 and 2.3.

In Fig 2.4, we plot the redshift dependence of the specific rate of formation of FOF halos through major mergers for our 6 bins of halo mass. A halo is defined to have just undergone m major mergers if its progenitor subhalos at the previous output come from at least $m + 1$ different FOF halos, and if the total subhalo mass coming from m of the subdominant FOF progenitors is more than a third of that coming from the main FOF progenitor. This merger count can then be used to define a merger rate in direct analogy to equation (1). The six curves of Fig. 2.4 can be compared directly with the curves for the 6 most massive classes of Fig. 2.1. The behaviour is quite different, however. In Fig. 2.4 there is a strong and monotonic dependence of formation rate on redshift, but there is little dependence on halo mass. This is the exact contrary of what we found for galaxies, where the mass dependence was strong and the redshift dependence weak. The redshift dependence of these curves is reasonably well described as a simple proportionality to $(1 + z)$. For all masses the rates exceed unity for redshift beyond 1 or 2. Recall that in Fig. 2.1 we found the corresponding rates for galaxies to exceed unity only for the most massive systems. Major mergers are thus a much more significant growth mode for dark halos than they are for most galaxies.

Fig 2.5 shows dimensionless growth rates for FOF halos as a function of redshift for the same 6 halo mass bins. These rates are defined in exact analogy to equations (2) through (4) and refer to growth through major mergers (orange), through all resolved mergers (green), and through accretion of “diffuse” particles (i.e. simulation particles not assigned to any FOF halo with more than 20 particles; the black curve). Again the growth rate through major mergers parallels the specific formation rate already plotted in Fig. 2.4; the ratio of the two is just the average mass of the smaller partner in a major merger in units of the final halo mass. Both the growth rate through major mergers and the growth rate through all (resolved) mergers are near power-laws of similar slope. The growth rate through all resolved mergers exceeds that through major mergers by a larger factor for high-mass halos than for low-mass ones. This primarily reflects the fact that the resolution limit of the simulation corresponds to a much lower mass ratio limit for identifying a merger in the former case. This is not the whole story, however, as one can see by the fact that the diffuse accretion rate depends differently on redshift than the other growth rates. Hence the growth of objects of *given* mass is more strongly affected by accretion of diffuse material at early times than at late times. In addition, comparing the major merger growth rates (the

orange curves) with the total growth rates (the sum of the green and black curves), one sees that while at high masses and at early redshifts major mergers account for about 15% of the total growth rate, for small objects at late times they account for a larger fraction of the growth. Note that at all redshifts and for all masses, accretion of “diffuse” particles accounts for at least 30% of the total growth.

2.5 Summary and discussion

We have used publicly available data for the De Lucia & Blaizot (2007) model of galaxy formation to study the relative importance of merging and of star formation for the growth of galaxies. This model is based on stored halo merging trees for the *Millennium Simulation*, a very large simulation of the evolution of the dark matter distribution in a Λ CDM cosmology. It is consistent with a wide variety of observational data on the properties and clustering of galaxies both at low and at high redshift. We thus expect its behaviour to give at least a qualitative indication of the balance needed between the various modes of galaxy assembly in any successful model in the Λ CDM context. A particular goal of our study has been to contrast the roles of merging in galaxy and dark halo evolution.

The most striking result from our study is that formation through merging depends in a completely different way on mass and redshift for our two classes of object. Recent formation through a major merger is almost equally likely for halos of all masses at any given time, but is substantially more likely at early times than it is today. For galaxies, on the other hand, the likelihood of recent formation through a major merger is a strong function of stellar mass, but depends at most weakly on redshift. In addition, halos of all masses have grown more rapidly through mergers than all but the most massive galaxies. A little reflection shows that these differences are required by the facts that a galaxy cluster is considered as a single dark matter halo but contains many distinct galaxies, and that the stellar mass function for cluster galaxies differs little from that of the Universe as a whole. This implies that the build-up of massive halos through mergers cannot be paralleled by merging of the associated galaxies. Merging plays a much less important role (though still significant) in galaxy growth than in dark halo growth. The high rates of recent merging found for the most massive galaxies are a selection effect. Only through merging can galaxies attain such high masses. This is also the reason why the most massive galaxies are usually ellipticals,

A second striking result from our study is the increasing importance of star formation with increasing redshift for galaxies of all masses. At low redshift we find the observed result that mean specific growth rates through star formation are smaller in high-mass galaxies than in low-mass ones, but it turns out that this result also holds at high redshift. According to the De Lucia & Blaizot (2007) model there is no redshift where the specific star formation rate of massive galaxies significantly exceeds that of low mass systems. Individual objects may be experiencing dramatic starbursts, but averaged over the population of all objects of given stellar mass, the prediction is that the mean specific growth rate through star formation is always a decreasing function of stellar mass.

Only at redshifts below one and for galaxies comparable to or more massive than the Milky Way does the growth rate through mergers exceed that through star formation. This

corresponds nicely to the “transition stellar mass” at which the stellar populations and the structural parameters of local galaxies switch from being predominantly star-forming and disk-like to predominantly old and spheroidal (Kauffmann et al. 2003a). This agreement is, of course, in part a consequence of the tuning of the parameters of the galaxy formation model to fit observation.

A less surprising but still interesting result is that merger-related growth for objects of all stellar masses and at most times is roughly equally divided between what we have defined as major and minor mergers. Clearly our separation at a progenitor stellar mass ratio of 3 to 1 is arbitrary. If we had chosen 5 to 1, major mergers would have dominated in most cases. If we had chosen 50 to 1, minor mergers would have been unimportant. Clearly the accretion of the LMC will make a much more significant change to the Milky Way’s stellar mass than the addition of all the Dwarf Spheroidals, and this in turn will be dwarfed by the impending merger with M31!

As we now show, the FOF halo behaviour we find is at least qualitatively consistent with the predictions of EPS theory (Lacey & Cole 1993). The analytical expression for the probability that a mass element which is part of a halo of given mass M_2 at time t_2 is part of a halos of (smaller) mass M_1 at the earlier time t_1 is

$$\begin{aligned} & f(S_1, \omega_1 | S_2, \omega_2) dS_1 \\ &= \frac{\omega_1 - \omega_2}{(2\pi)^{1/2} (S_1 - S_2)^{3/2}} \exp\left[-\frac{(\omega_1 - \omega_2)^2}{2(S_1 - S_2)}\right] dS_1 \end{aligned}$$

where $S_{1,2}$ are the mean square linear density fluctuations (extrapolated to $z = 0$) in spheres containing mean mass $M_{1,2}$, $\omega_{1,2} \equiv \delta_{c0}/D(z_{1,2})$ are the redshift-dependent critical densities for collapse, $D(z)$ is the growth factor of linear fluctuations, and $\delta_{c0} \approx 1.69$ is a constant. By taking the limit as t_2 tends to t_1 (so $\omega_2 - \omega_1$ tends to 0) and integrating over S_1 , we can get the dimensionless merger rate per product halo:

$$\begin{aligned} & \frac{P(M_{high}, M_{low}, \omega_1 | S_2, \omega_2)}{dt/t} \\ &= \frac{1}{2} \int_{S(M_{low})}^{S(M_{high})} \frac{M_2}{M_1} \frac{t * d\omega/dt}{(2\pi)^{1/2} (S_1 - S_2)^{3/2}} dS_1 \end{aligned}$$

Setting $M_{low} = \frac{M_2}{4}$ and $M_{high} = \frac{3M_2}{4}$ we get the major merger rate which is seen to evolve with time as $t * d\omega/dt$. In a Einstein de Sitter universe $D(z) \propto (1+z)^{-1} \propto t^{2/3}$ and thus $t * d\omega/dt \propto (1+z)$, roughly reproducing the behaviour we get for the major merger rate of FOF halos in the Millennium Simulation. In the Λ CDM cosmology, the formula is more complex but is quantitatively similar. As shown by Carroll et al. (1992), $D(z) = g(z)/[g(0)(1+z)]$ where

$$g(z) \approx 5/2\Omega_m[\Omega_m^{4/7} - \Omega_\Lambda + (1 + \Omega_m/2)(1 + \Omega_\Lambda/70)]^{-1}$$

and Ω_m (Ω_Λ) is the density parameter of matter (dark energy). We plot $t * d\omega/dt$ against $1+z$ for the two cases in Fig 6 to illustrate the size of the expected differences.

Table 2.1: Table 1:Relative growth rates due to major mergers and to other accretion modes.

α	$R_m(\text{majormergers}) : R_m(\text{smoothaccretion})$
-2/3	0.40 : 0.60
-1/3	0.37 : 0.63
-1	0.43 : 0.57

The same formalism also allows the dimensionless mass accretion rates through mergers and/or smooth accretion to be expressed as

$$\frac{P_M(M_{high}, M_{low}, \omega_1 | S_2, \omega_2)}{dt/t}$$

$$= \frac{1}{2} \int_{S(M_{low})}^{S(M_{high})} \frac{M_2}{M_1} \frac{t * d\omega/dt}{(2\pi)^{1/2} (S_1 - S_2)^{3/2}} \frac{\min(M_1, M_2 - M_1)}{M_2} dS_1$$

The M_2 dependence of this rate can be seen by assuming the limits M_{low} and M_{high} to scale with M_2 , and approximating the dependence of S on M as a power-law $S \propto M^\alpha$, where $\alpha = -(n+3)/3$ for the usual definition of the density power spectrum index n . The *rhs* of the above equation then scales as $M_2^{-\alpha/2}$. When n lies in the expected range between -2 and -1 , the mass dependence is very weak, roughly $\sim M_2^{0.2}$. Taking into account that in the simulation one cannot really take infinitesimal time intervals, this dependence on final halo mass may be further weakened by the exponential term in the expression for f .

Finally, we can also use these formulae to estimate the ratio of the growth rate through major mergers to that through “smooth” accretion (here defined as $M_1 < \frac{1}{4}M_2$). It is not easy to obtain analytic expressions for this ratio but it can easily be computed from the above formulae in the power law approximation for $S(M)$. Here we give in Table 1 the relative fraction for several typical values of α . Roughly speaking, major mergers are predicted to contribute around 40% of the total mass accretion, somewhat larger than the 25% we obtain from our simulation results.

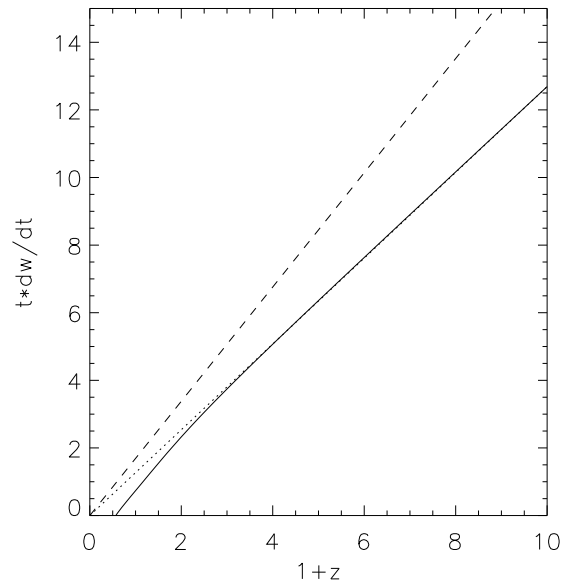


Figure 2.6: Predicted relation between $t * d\omega/dt$ (proportional to the dimensionless merger rate) and $1 + z$ for the concordance Λ CDM model (solid curve) and for an Einstein de Sitter universe (dashed curve) according to extended Press-Schechter theory. At redshifts above about 0.5 the two quantities are very nearly proportional to each other in the Λ CDM case also, as shown by the dotted straight line.

High Redshift Galaxy Populations and their Descendants: What we can tell about the fate of the high redshift galaxy populations from galaxy formation models

Abstract

We study predictions in the concordance Λ CDM cosmology for the abundance and clustering of high-redshift galaxies and for the properties of their descendants. We focus on three high-redshift populations: Lyman break galaxies at $z \sim 3$ (LBGs), optically selected star-forming galaxies at $z \sim 2$ (BXs), and distant red galaxies at $z \sim 2$ (DRGs). We select galaxies from mock catalogues based on the Millennium Simulation using the observational colour and apparent magnitude criteria. With plausible dust assumptions, our galaxy formation model can simultaneously reproduce the abundances, redshift distributions and clustering of all three observed populations. The star formation rates (SFRs) of model LBGs and BXs are lower than those quoted for the real samples, reflecting differing initial mass functions and scatter in model dust properties. About 85% of model galaxies selected as DRGs are star-forming, with SFRs in the range 1 to $\sim 100 M_{\odot}/\text{yr}$. Model LBGs, BXs and DRGs together account for less than half of all star formation over the range $1.5 < z < 3.2$; many massive, star-forming galaxies are predicted to be too heavily obscured to appear in these populations. Model BXs have metallicities which agree roughly with observation, but model LBGs are only slightly more metal-poor, in disagreement with recent observational results. The model galaxies are predominantly disk-dominated. Stellar masses for LBGs and BXs are $\sim 10^{9.9} M_{\odot}$, and for DRGs are $\sim 10^{10.7} M_{\odot}$. Only about 30% of model galaxies with $M_* > 10^{11} M_{\odot}$ are classified as LBGs or BXs at the relevant redshifts, while 65% are classified as DRGs. Almost all model LBGs and BXs are the central galaxies of their dark halos, but fewer than half of the halos of any given mass have an LBG or BX central galaxy. Half of all LBG descendants at $z = 2$ would be identified as BX's, but very few as DRGs. Clustering increases with decreasing redshift for descendants of all three populations, becoming stronger than that of L^* galaxies by $z = 0$, when many have become satellite galaxies and their typical stellar mass has increased by a factor of 10 for LBGs and BXs, and by a factor of 3 for DRGs. This growth is dominated

by star formation until $z \sim 1$ and thereafter by mergers. Merging is predicted to be more important for LBG and DRG descendants than for BX descendants. Most LBGs and DRGs end up as red ellipticals, while BXs have a more varied fate. Over 70% of local galaxies with $M_* > 10^{11} M_\odot$ are predicted to have at least one LBG/BX/DRG progenitor.

3.1 Introduction

The redshift interval $1 < z < 3$ is a very important epoch in the history of galaxy formation. During these several billion years, the star formation rate per unit comoving volume, the abundance of luminous quasars and the specific merger rate of galaxies all reached their peak values. This is when the Hubble sequence of galaxies was established, and most galactic stars were formed.

The last few decades have seen a remarkable development in the observational study of high-redshift galaxies. Using strong the Lyman break feature in the spectrum of star-forming galaxies, Steidel et al. (1996) developed colour-colour criteria to select so-called Lyman Break Galaxies (LBGs) at $z \sim 3$ using deep U_nGR photometry. Extensions of this technique allowed the selection of large samples of star-forming galaxies at lower redshifts, specifically $z \sim 2.3$ (BXs) and $z \sim 1.7$ (BMs) (Adelberger et al. 2004). Recent observations show that there are many high-redshift galaxies with rather little rest-frame UV luminosity which are missed in such optically selected surveys. Franx et al. (2003) have successfully developed near-infrared colour criteria to select distant red galaxies (DRGs) at $z \sim 2$ using deep JK photometry. Follow-up observations at a variety of wavelengths have clarified the physical properties of all these high-redshift galaxy populations by providing star-formation rates (Erb et al. 2006a; Reddy et al. 2006), stellar masses (Shapley et al. 2005; Erb et al. 2006b; Kriek et al. 2006; Papovich & et al. 2006), morphologies (Abraham et al. 1996; Papovich et al. 2005; Law et al. 2007), dust luminosities (Webb et al. 2003), kinematics (Pettini et al. 2001; Erb et al. 2006b) and clustering estimates (Adelberger et al. 2005; Quadri et al. 2008).

Each of these observational samples provides information on a limited subset of the galaxy population at a specific cosmic epoch, and it is obviously of interest to understand their relation to the population as a whole, both at the redshift of observation and at other redshifts, particularly $z = 0$ where our knowledge of galaxies is best. Within the current standard cosmological paradigm, structure formation in the gravitationally dominant dark matter distribution can be simulated reliably and is now quite well understood (e.g. Springel et al. 2006). For the purposes of modelling galaxy evolution, it can usefully be idealised as a distribution of dark matter halos of “universal” structure which grow steadily in mass through accretion and merging. Galaxies form through condensation of gas within this evolving dark halo population, as first set out by White & Rees (1978). At any given time their distribution can be well modelled by populating halos with galaxies according to a simple recipe, and then adjusting parameters to fit the observed abundance and clustering. The recipe can be based either on a simplified model of the galaxy formation process or on fitting formulae which make no direct reference to the underlying physics (Peacock & Smith 2000; Seljak 2000). The flexibility of the latter Halo Occupation Distribution (HOD) approach allows excellent fits to galaxy luminosity functions and clustering

properties at any given epoch (see Cooray & Sheth 2002 for a review) but provides no natural way to link populations at different epochs (see Conroy & Wechsler (2008) for a recent attempt to remedy this). In addition, detailed physical models are needed to assess how observational cuts on luminosity and colour affect the properties of high redshift samples.

A more straightforward approach is to follow galaxy formation directly within the evolving dark matter distribution. This extends the semi-analytic technique developed in the early 1990's (White & Frenk 1991; Kauffmann et al. 1993b; Cole et al. 1994), and has made increasingly sophisticated use of information from N -body simulations of cosmic structure formation (Kauffmann et al. 1997, 1999; Springel et al. 2001, 2005b). The idea is to design simple parametrised models for the baryonic physics, based either on observation or on more detailed simulations of individual systems, and to implement these recipes in the structure formation framework provided by a dark matter simulation. This provides a powerful tool for studying the formation, evolution and clustering of the galaxy population. It is much less resource-intensive than simulations involving a more direct treatment of baryonic processes, and as a result it allows the treatment of larger volumes and the exploration of a wider range of input parameters and physics recipes. Recent improvements in such modelling have included the move to higher resolution N -body simulations, enabling use of the substructure information they provide (Springel et al. 2001; Okamoto & Nagashima 2001; Helly et al. 2003; Hatton et al. 2003; Okamoto & Nagashima 2003; Springel et al. 2005b; Kang et al. 2005) and the inclusion of additional relevant physics, for example, AGN feedback (Croton et al. 2006; Bower et al. 2006), galactic winds (Bertone et al. 2007) and gas stripping in clusters (Font et al. 2008). These techniques have previously been used to study the properties of LBGs by Blaizot et al. (2004).

The semi-analytic models used in this paper are implemented on the *Millennium Simulation* (Springel et al. 2005b, hereafter MS) and are a minor modification of those presented in De Lucia & Blaizot (2007, hereafter DLB07) and Kitzbichler & White (2007, hereafter KW07), which are publicly available at the MS download site¹. These are refinements of the model originally published as Croton et al. (2006). They have successfully matched a wide range of galaxy properties both locally and at high redshift, but there are some notable discrepancies which demonstrate that the description of galaxy formation physics remains incomplete. Our models (and that of KW07) differ from the model of DLB07 only through the introduction of a redshift dependence in the way dust is treated. We construct light-cone surveys of our models as in KW07, and we select LBGs, BXs, and DRGs exactly as in observational studies. We then compare observed and simulated samples in terms of their abundance, their clustering and their distributions of redshift, colour, metallicity and star formation rate, finding good agreement in most cases. We move on to examine model predictions for the relation of these various populations to each other and to the high-redshift galaxy population as a whole, and for the properties of their descendants at lower redshift.

Our paper is organized as follows. In Sec. 3.2, we summarize relevant properties of the *Millennium Simulation*, of the semi-analytic model and of our light-cone surveys. Sec. 3.3 deals with the selection of model LBG, BX and DRG samples, and compares them with observed samples. Sec. 3.4 examines the relation of these model samples to each other and

¹<http://www.mpa-garching.mpg.de/millennium>

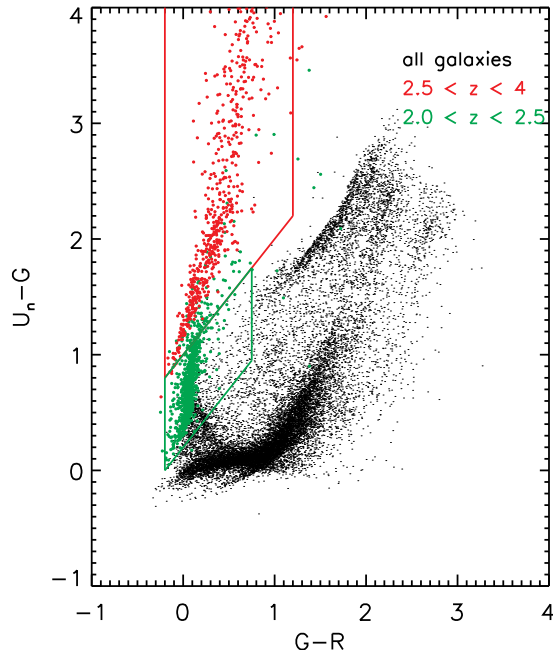


Figure 3.1: $G - R$ vs. $U_n - G$ diagram for model galaxies selected from a mock redshift survey. The redshift ranges highlighted by coloured circles are indicated in the upper right corner. The red and green boxes outline the original observationally defined selection windows for LBGs and BXs respectively.

to the full high-redshift population, and the properties of their descendants. We summarize our results in Sec. 3.5.

3.2 Galaxy Formation

Our mock galaxy catalogues are constructed by implementing a series of semi-analytic galaxy formation models on stored merger trees which represent the entire growth of non-linear structure, both dark matter halos and their subhalos, in the very large *Millennium Simulation* (Springel et al. 2005b). This simulation assumed a concordance Λ CDM cosmology with parameters consistent with a combined analysis of the 2dFGRS and the first-year WMAP data (Spergel et al. 2003): $\Omega_m = 0.25$, $\Omega_b = 0.045$, $h = 0.73$, $\Omega_\Lambda = 0.75$, $n = 1$, and $\sigma_8 = 0.9$, where the Hubble constant is parameterized as usual as $H_0 = 100h \text{ km s}^{-1} \text{ Mpc}^{-1}$. The *Millennium Simulation* represents the dark matter distribution by following $N = 2160^3$ particles from redshift $z = 127$ to $z = 0$ in a comoving box of side $500h^{-1} \text{ Mpc}$. Each particle thus has a mass of $8.6 \times 10^8 h^{-1} M_\odot$. The simulation data were stored at 64 redshifts apaced approximately logarithmically at early times and linearly at late times. This spacing determines the time resolution of the semi-analytic modelling of galaxy formation, A detailed description of the *Millennium Simulation* can be found in the original article of

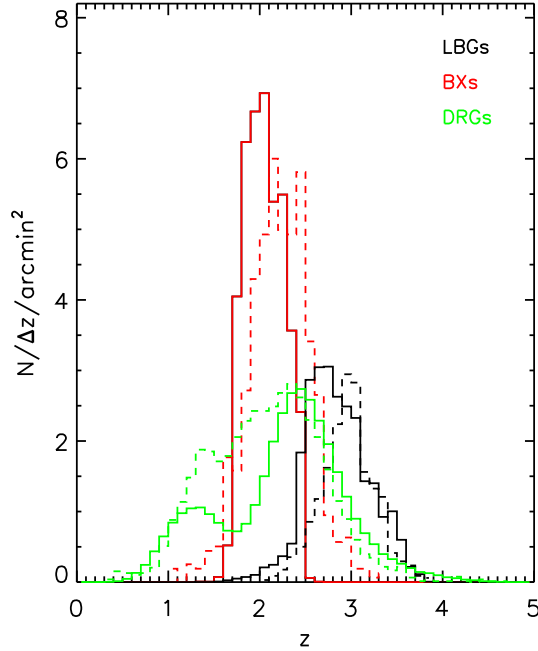


Figure 3.2: Redshift distributions for LBGs, BXs and DRGs. The solid histograms are for mock galaxies while dashed ones are for the real observed samples. Black histograms indicate LBGs, red ones indicate BXs and green ones indicate DRGs (scaled up in number by a factor of 3 for clarity). Note that the normalisations are given in terms of the surface density of objects on a linear scale, and have not been adjusted. The models do indeed reproduce the observed abundance as a function of redshift for all three types of object.

Springel et al. (2005b)

The simulation of the evolution of the galaxy population is based on the modelling techniques developed by the Munich Group. Our galaxy formation model is almost identical to the publicly available model of De Lucia & Blaizot (2007) which is itself a refinement of the model originally implemented on the *Millennium Simulation* by Croton et al. (2006). These models include treatments of gas cooling, star formation and stellar evolution, chemical enrichment, central black hole formation and growth, material and energy feedback both from supernovae and from (radio) AGN, and galaxy merging. The reader is referred to DLB07 and Croton et al. (2006) for detailed descriptions of how these processes are modelled. As was also the case in KW07, we have found it necessary to modify the original treatment of dust attenuation in order to be consistent with high-redshift observations. We describe this in the next section.

3.2.1 Dust Model

Dust extinction is a crucial ingredient when comparing models of galaxy evolution with observation. In this paper we adopt a simple dust model similar to that used in KW07.

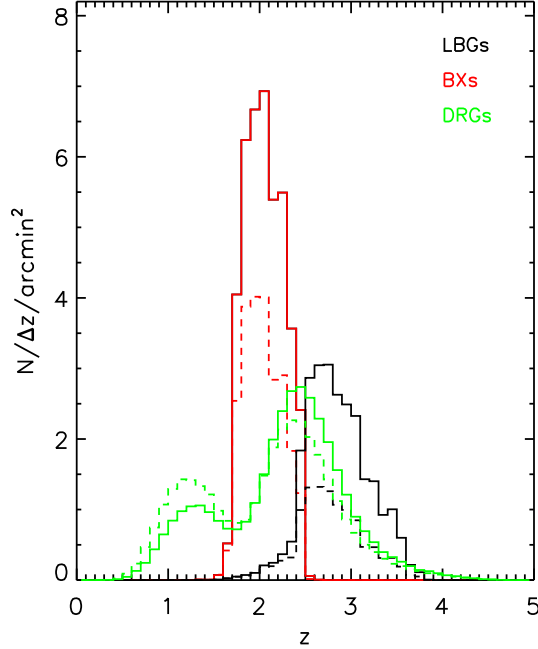


Figure 3.3: Redshift distributions for LBGs, BXs and DRGs. The solid histograms repeat the predictions of our preferred model from Fig. 3.2. The dashed histograms are predictions from the original DLB07 model. This differs from our model only in that it assumes a redshift-independent recipe for calculating extinction from the gas mass, metallicity and size of a galaxy.

The face-on optical depth is modeled as a function of HI column density and metallicity in the following way:

$$\tau_{\lambda}^Z = \left(\frac{A_{\lambda}}{A_V}\right)_{z_{\odot}} \eta_Z \left(\frac{\langle N_H \rangle}{2.1 \times 10^{21} \text{ cm}^{-2}}\right) \quad (3.1)$$

where A_{λ}/A_V is the extinction curve estimated in Cardelli et al. (1989) and $\langle N_H \rangle$ is the the average hydrogen column density. The quantity $\eta_Z = (1+z)^{-0.4} (Z_{gas}/Z_{\odot})^s$ is the redshift- and metallicity-dependent scaling of dust-to-gas ratio, where $s = 1.35$ for $\lambda < 2000\text{\AA}$ and $s = 1.6$ for $\lambda > 2000\text{\AA}$, The metallicity scalings interpolate between the extinction curves measured in the Milky Way and in the two Magellanic Clouds (Guiderdoni & Rocca-Volmerange 1987). The redshift dependence is observationally motivated, based on indications that dust-to-gas ratios are lower at high redshift than in the local universe for galaxies with the same bolometric luminosity and metallicity (Adelberger & Steidel 2000). In KW07 a similar model was used, except that the redshift dependence was set to be $(1+z)^{-0.5}$ and an artificial disk size evolution with redshift was assumed so that the equivalent redshift dependence of dust extinction became $(1+z)^{-1}$. As in DLB07 and KW07, we assume that the radii of galaxy disks are proportional to the virial radii of their dark matter halos. There is rather little change in the number count and redshift distribu-

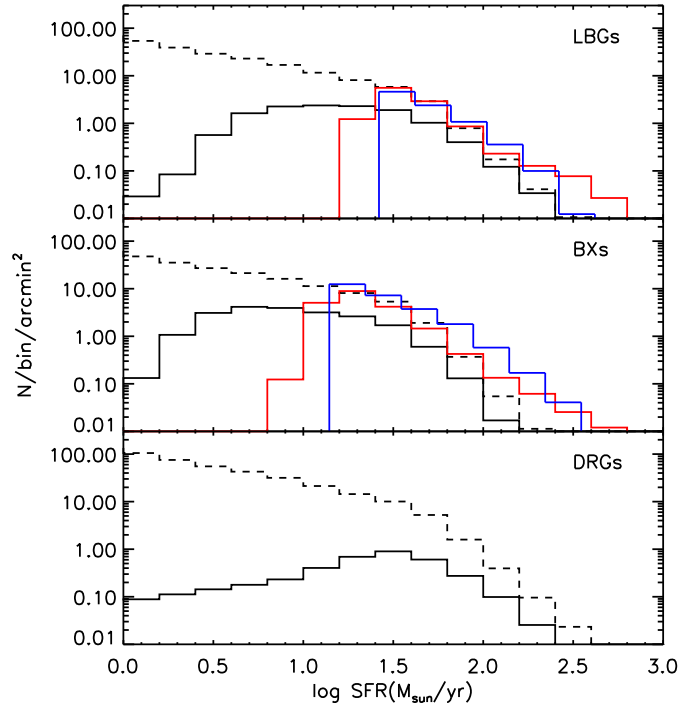


Figure 3.4: Star formation rate distributions for LBGs, BXs and DRGs. Solid black histograms in each panel refer to model galaxies selected according to the observational colour and magnitude criteria which define the relevant population. They may be compared with the dashed black histograms which give results for all model galaxies in the corresponding redshift range. At all redshifts and SFRs, the observational criteria select fewer than half of all star-forming galaxies. Blue histograms in the LBG and BX panels are direct observational estimates of the SFR distributions for these two populations taken from Reddy et al. (2008). They are clearly centred at higher SFR than in the models. The red histograms show what happens if SFRs are estimated for the model galaxies from their “observed” fluxes assuming the same mean correction for extinction and the same conversion factor from UV luminosity to SFR as in Reddy et al. (2008). The results agree well with the “observed” SFR values but differ substantially from the true values.

tion of galaxies in our mock catalogues when the power index of the redshift dependence is changed from -1 to -0.4. We will show later that the dust model we adopt here produces high-redshift galaxies with the proper number density both at $z \sim 3$ and at $z \sim 2$.

In addition, our dust model assumes that young stars, defined as stars younger than 3×10^7 yr, are more strongly attenuated than the rest of the galaxy. This population is typically still partly embedded in the molecular clouds from which it formed, and so suffers more obscuration than the general population. Based on the results of Charlot & Fall (2000), we assume the mean optical depth in front of young stars to be three times that which applies to older populations. Our extinction model does not distinguish between young stars in “quiescent” disks and young stars in major starbursts. This will lead us to underestimate

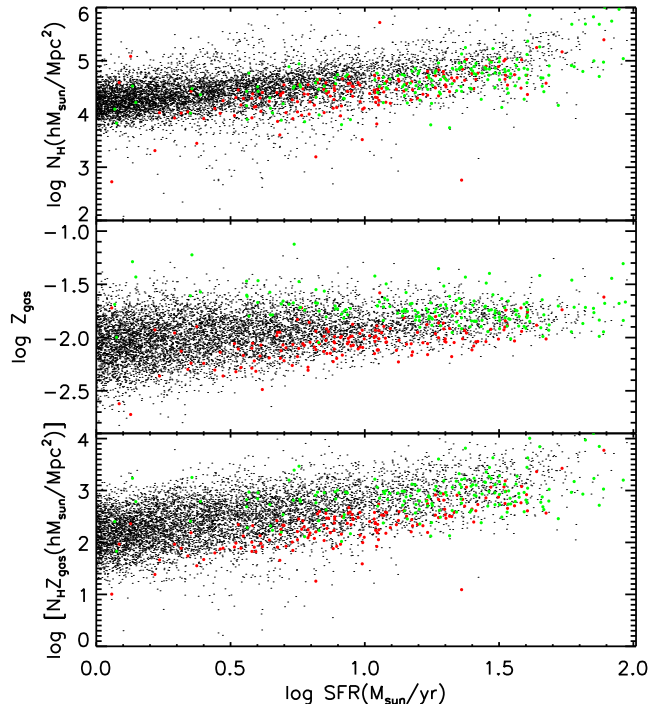


Figure 3.5: Gas surface density (upper panel), metallicity (middle panel) and the product of the two (bottom panel) plotted against star formation rate for model galaxies at $z = 2.2$. Red and green points are galaxies that satisfy the BX and DRG selection criteria respectively. Black dots correspond to other galaxies, most of which are excluded from either sample because they are too faint.

dust effects in the latter, since we estimate the gas column (and so the extinction) for the galaxy as a whole, whereas strong starbursts are observed to occur in more compact regions with substantially higher than average extinction. Our models are too crude to be able to treat this realistically, so we do not attempt to treat galaxy populations where these effects dominate, e.g. ultraluminous infrared galaxies or high-redshift submillimeter galaxies. When calculating extinctions we assign a random inclination to every galaxy and assume a slab geometry to obtain an effective extinction from the face-on value.

3.2.2 Light-cone

To make a direct comparison of our galaxy formation simulation with observation, it is necessary to create a deep light-cone survey which mimics a real observational survey. Here we use techniques developed by KW07 to set up the geometry of the light-cone on the periodic *Millennium Simulation* and to interpolate galaxy properties from the discrete stored outputs to the continuously varying redshift coordinate of the light-cone. The only difference to KW07 is in the dust treatment, as described in the last subsection. We refer the reader to the original paper for detailed descriptions.

For this paper we construct a mock catalogue on an area of 1.4×1.4 square degrees.

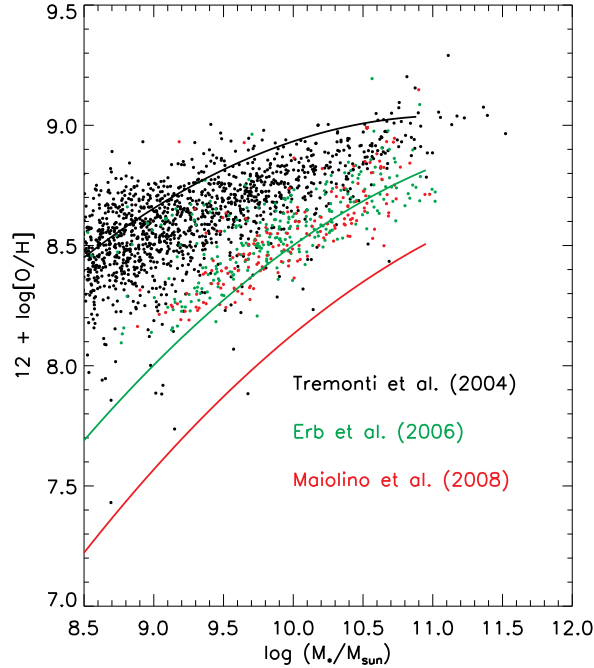


Figure 3.6: Stellar mass vs. gas-phase metallicity for star-forming galaxies. Black dots represent the low-redshift galaxies, the green dots represent BXs, and the red dots represent LBGs. Observational estimates of the mean relations between these quantities are overplotted using curves with the same colour coding. The sources of the observational relations are indicated by labels

We calculate apparent magnitudes in the (U_n, G, R) filters used by the KPNO survey of Steidel et al. (2004) and in the (J, H, K) filters used by the MUSYC survey of Quadri & et al. (2007a). IGM absorption is modeled by taking into account Lyman series line blanketing, continuum absorption by neutral hydrogen and absorption by heavy elements according to the recipes of Madau (1995). We quote all magnitudes in the AB system. There are a total of 5566388 galaxies in our mock catalogue, of which 393272 and 224604 galaxies are brighter than apparent magnitudes of $R < 25.5$ and $K < 22.86$, respectively. These are the respective limits of the KPNO and MUSYC surveys.

3.3 Mock Catalogue

3.3.1 Sample Selection

Owing to the sharp drop-off which it causes at rest-frame 912\AA , the Lyman break can be used to identify star-forming galaxies at $z \sim 3$ from optical broad-band photometry. Steidel et al. (1996) developed an effective criterion for identifying such Lyman Break

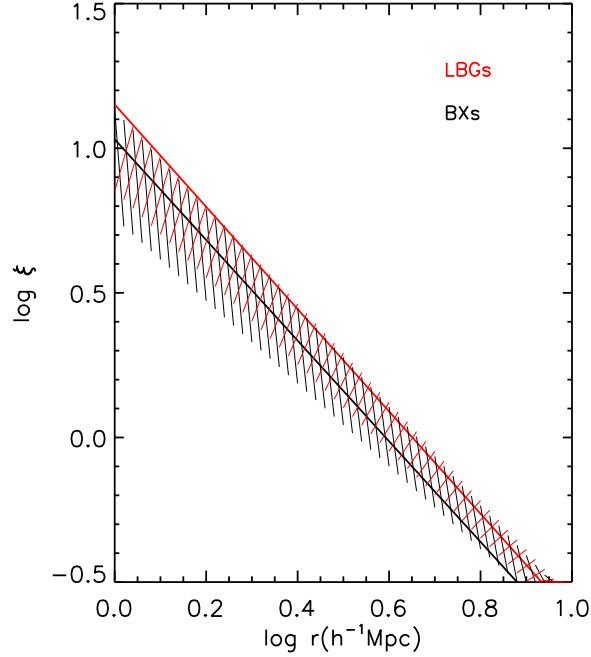


Figure 3.7: 3D correlation functions for LBGs and BXs. The solid curves are for galaxies from our mock catalogue, while the hatched regions indicate the $\pm 1\sigma$ range for the strength of observed correlations, as quoted by Adelberger et al. (2005). Red curves are for LBGs and black curves are for BXs.

Galaxies (LBGs) based on $U_n - G$ and $G - R$ colours as follows:

$$R \leq 25.5 \quad (3.2)$$

$$U_n - G \geq G - R + 1.0 \quad (3.3)$$

A similar technique was later developed by Adelberger et al. (2004) to pick out star-forming galaxies at lower redshifts ($z \sim 2$) so-called BX and BM systems. The criteria proposed for selecting BXs are:

$$R \leq 25.5 \quad (3.4)$$

$$G - R \geq -0.2 \quad (3.5)$$

$$U_n - G \geq G - R + 0.2 \quad (3.6)$$

$$G - R \leq 0.2(U_n - G) + 0.4 \quad (3.7)$$

$$U_n - G \leq G - R + 1.0 \quad (3.8)$$

Fig. 3.1 shows a colour-colour diagram for galaxies in our mock catalogue. Only galaxies with R -band apparent magnitude brighter than 25.5 are shown, in order to mimic the magnitude limit of the observations. Red circles indicate galaxies in the redshift range $2.5 < z < 4.0$, while green circles show galaxies with $2.0 < z < 2.5$. Black dots show galaxies

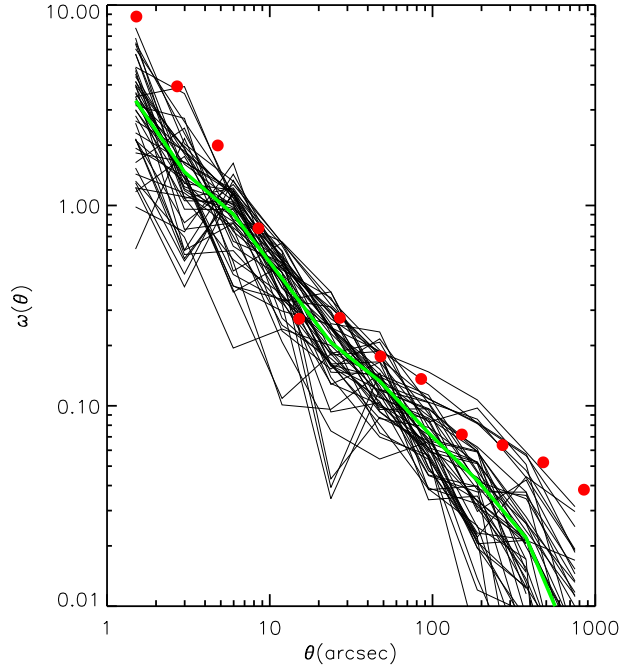


Figure 3.8: Angular correlation functions for DRGs. Thin black curves are estimates from 48 independent mock catalogues for fields similar in size to that analysed by Quadri et al. (2008). The thick green curve is the average of these 48 model estimates, while the red dots indicate the actual measurement of Quadri et al. (2008).

at other redshifts. Red and green boxes outline the colour selection criteria for LBGs and BXs respectively. Clearly our model predicts LBGs and BXs with the proper colours. A careful comparison with Fig.1 in Steidel et al. (2004) shows, however, that the model LBGs and BXs are about 0.2 mag. bluer in $G - R$ colour than the real systems. Our colours would be shifted to the red by about 0.1 if we adopted a Calzetti dust model (Calzetti et al. 2000) rather than that described above. In our mock catalogues the number densities of LBGs and BXs with $R < 25.5$ are 2.37 and 4.35 per square arcminute, respectively, within 30% of the observational estimates (Steidel et al. 2003, 2004): 1.8 per sq.arcmin for LBGs and 5.2 per sq.arcmin for BXs.

Distant Red Galaxies (DRGs) are K-selected galaxies (Franx et al. 2003) satisfying:

$$K < 22.86 \quad (3.9)$$

$$J - K > 1.3 \quad (3.10)$$

The number density of such objects in our mock catalogue is 1.16 per sq.arcmin, in good agreement with the observed density of 1.4 per sq.arcmin. More impressively, we also reproduce the number density of a subsample of DRGs with $2 < z < 3$; there are 0.68 per sq.arcmin. in our mock catalogue, in excellent agreement with the observed value of 0.66 per sq.arcmin given by Quadri et al. (2008).

If we revert to the DLB07 dust model by removing the redshift-dependence of our assumed dust-to-gas ratios, the surface number densities of LBGs, BXs and DRGs drop to 1.2, 3.0 and 1.0 per square arcminute, respectively. For the optically selected galaxies, these values are significantly below those observed.

3.3.2 Redshift Distributions

We show redshift distributions for LBGs, BXs and DRGs in Fig. 3.2. Black histograms refer to LBGs, red histograms to BXs and green histograms to DRGs. Solid histograms are for model galaxies in our mock catalogue, while the dashed histograms are taken from Steidel et al. (2004) for LBGs and BXs and from Quadri et al. (2008) for DRGs. Note that the normalisations in these histograms have not been adjusted and that the numbers of galaxies are plotted on a linear scale. The redshift distributions for model LBGs and BXs are consistent with observation, although shifted slightly towards lower redshift. Rather than the observed ranges, $2.7 < z < 3.4$ for LBGs and $1.9 < z < 2.7$ for BXs, in our model the LBGs lie primarily in the range $2.5 < z < 3.2$ and the BXs in the range $1.7 < z < 2.5$. These lower redshift BXs correspond to the black dots in Fig. 3.1 lying within the green selection window. The redshift distribution of DRGs is similar that shown in Quadri & et al. (2007a) with a gap between $1.6 < z < 2$. However, recent studies (Quadri et al. 2008; Grazian et al. 2006) show a continuous distribution over $1 < z < 3$, with no evident gap. Further observations are needed to reduce photometric redshift uncertainties and to test whether this gap is an artifact or a real feature. In our model it is caused by the number density of DRG's decreasing with redshift for $1 < z < 2$, due to the K -band apparent magnitude limit, but then increasing again for $z > 2$ as the Balmer break moves into the J -band, allowing a broader range of galaxies to pass the $J - K$ colour cut. Thus the gap might be real.

In our mock catalogue, contamination by low redshift interlopers is $\sim 0.9\%$ for LBGs ($z < 2$), $\sim 8\%$ for BXs ($z < 1$) and $\sim 24\%$ for DRGs ($z < 1.8$). These numbers are quite similar to the observational results: $\sim 0.5\%$ for LBGs (Steidel et al. 2003), 6% for BXs (Steidel et al. 2004) and $\sim 15\%$ for DRGs (Reddy et al. 2008). The fraction of galaxies with redshift $2.5 < z < 3.2$ and apparent magnitude $R < 25.5$ which satisfy the LBG colour criteria is 96% in our model. The fraction of galaxies with redshift $1.7 < z < 2.5$ and $R < 25.5$ which satisfy the BX colour criteria is 76% . Both are higher than the observational values quoted by Reddy et al. (2008): 47% for LBGs and 58% for BXs. Photometric errors, which scatter intrinsically more (or less) luminous galaxies into (or out of) the selection windows may partly account for the low observational completeness. On the other hand, in our model, neither AGN luminosity nor Ly α line luminosity has been taken into account, both of which may affect the selection efficiency.

In Fig. 3.3 we compare the redshift distributions of our model LBGs, BXs and DRGs (solid histograms) with predictions from the original DLB07 model (dashed histograms). Although removing the redshift-dependence of our dust model significantly changes the abundances of galaxies in all three classes (resulting in too few LBGs and BXs to be compatible with observation) it makes very little difference to the redshift distributions.

3.3.3 Star Formation Rate

We plot the star formation rate distributions of LBGs, BXs and DRGs in Fig. 3.4. Our model galaxies (solid black histograms) cover a wide range in star formation rate, with average values of $21M_{\odot}/\text{yr}$ for LBGs, $11M_{\odot}/\text{yr}$ for BXs and $24M_{\odot}/\text{yr}$ for DRGs. Observational estimates of star formation rates are shown by the blue histograms (Reddy et al. 2008) and are typically several tens of M_{\odot}/yr for LBGs and more than $15M_{\odot}/\text{yr}$ for BXs, significantly larger than the values for our model galaxies.

The star formation rate estimates in Fig. 3.4 were derived from dust-corrected UV magnitudes. Rather than using the actual SFR values for our model galaxies, we can estimate “observational” values from the apparent magnitudes and colours by applying the procedures proposed by Reddy et al. (2008). We derive an “unextincted” UV luminosity for each object by combining its G and R magnitudes to get an approximate rest-frame 1700\AA apparent magnitude. We use its redshift to get the corresponding absolute magnitude. We then multiply by 4.5 as a mean correction for extinction. The resulting UV luminosity is converted to a star formation rate using the relation given by Kennicutt (1998) for a Salpeter Initial Mass Function (IMF).

The result is shown in Fig. 3.4 by the red histograms. These now agree quite well with the “observed” data from Reddy et al. (2008), reflecting the fact that the magnitudes, colours and redshifts of the model galaxies agree quite well with those of the observed populations. The distributions of these “observational” SFR estimates disagree badly, however, with the true SFR distributions in the models. Only a small part of this is due to the fact that the mean extinction in our model is a factor of 3.9, slightly lower than the factor of 4.5 proposed in Reddy et al. (2008). Almost a factor of two comes from the fact that the conversion from UV luminosity to SFR assumes a Salpeter IMF, while the model assumes a Chabrier IMF. The substantial difference in shape reflects the fact that extinction factors vary dramatically from one object to another and are poorly represented by a mean value. Additional dispersion comes from the finite width of the galaxy redshift distribution which affects the conversion from observed magnitudes to rest-frame 1700\AA magnitude.

Thus the “observable” properties of our mock samples agree quite well with the real data, but their physical properties suggest that simple SFR estimates based on mean estimates of obscuration can lead to substantial systematic and random errors, in particular to an overestimate of the mean star formation rate.

Comparing the SFR distributions of our photometrically selected samples of model high-redshift galaxies to that for the high-redshift population as a whole (dashed histograms) we find that only around 30% of the galaxies with SFR greater than $5M_{\odot}/\text{yr}$ are selected as LBGs or BXs at $z \sim 3$ and $z \sim 2.2$, respectively. We show in Fig. 3.5 scatter plots of gas mass, gas-phase metallicity and the product of the two against SFR for all galaxies at $z = 2.2$ separated into those which satisfy the observational BX selection criteria (red) and those that do not (black). We also indicate in green the objects which satisfy the DRG selection criteria. BX systems are clearly less obscured than other galaxies with the same SFR. Gas content is the main contributor to this effect, although metallicity also plays a role. Similar effects are found for model LBGs – there are many objects at the same redshift with similar SFR which are not included in the LBG sample because obscuration makes them too faint. It is interesting to see that in the model there are many DRGs

among the highly extinguished part of the star-forming galaxy population at $z = 2.2$.

The last panel in Fig. 3.4 is the SFR distribution of model DRGs. Although selected as red galaxies, most DRGs are, in fact, star-forming. 85% of them fill a rather flat SFR distribution extending from 1 to $40 M_{\odot}/\text{yr}$ and beyond. Only around 15% of the DRGs are passive galaxies with SFR less than $1 M_{\odot}/\text{yr}$. One thing of interest is to explore the relation between DRGs and BXs. As can be inferred also from Fig. 3.5, very few DRGs are also BXs. We will discuss this further below.

3.3.4 Mass-Metallicity Relations

Fig. 3.6 plots stellar mass against gas-phase metallicity for LBGs (red), for BXs (green) and for $z = 0$ star-forming galaxies (black) in our model. Mean observational relations taken from Tremonti et al. (2004) (for local galaxies), from Erb et al. (2006b) (for BXs) and from Maiolino & et al. (2008) (for LBGs) are overplotted as solid curves of the corresponding colour. The mass-metallicity relations for local star-forming galaxies and for BXs are moderately well reproduced by the model. (The $z = 0$ result was already given by De Lucia et al. (2004).) The strong evolution between these two populations reflects the different physical properties of star-forming galaxies at these two well-separated epochs. It appears somewhat smaller in the model than in the real data. At early times, the galaxies are more gas-rich and their gas metallicity is relatively low compared to local galaxies of the same stellar mass. The metallicity predicted for BXs is higher than that for LBGs, but the difference is small; both BXs and LBGs are selected as UV-bright star-forming galaxies and they are separated by only 1 Gyr. This is inconsistent with the results of Maiolino & et al. (2008); the slope of their observed LBG mass-metallicity relation is similar to that of our model, but its normalisation is much lower, indicating a strong apparent evolution between $z \sim 2.2$ and $z \sim 3$.

3.3.5 Correlation Functions

We show 3D two-point spatial correlation functions for model LBGs (red) and BXs (black) in Fig. 3.7 and we compare them with observational data from Adelberger et al. (2005). The solid curves are the mean functions for model LBGs and BXs, while the hatched regions between the dashed lines show the $\pm 1\sigma$ range estimated for their observed clustering. For LBGs the model results lie within this one sigma band but are near its upper limit. For BXs the predicted clustering strength is well centred in the observational band, but the slope of the predicted correlation function is slightly higher than observed.

The number density of DRGs is quite small. To get a more statistically secure result and to estimate how cosmic variance may affect observational clustering measurements, we constructed 48 light-cones for areas of size $0.8 \times 0.8 \text{ deg}^2$. In an attempt to better mimic observational uncertainties, we assign a “photometric redshift” to each model galaxy by adding a random perturbation to its true redshift. Based on the data of Quadri et al. (2008), we set the *rms* value of this perturbation to be $(1 + z) * 0.06 \sim 0.18$. We then study the angular correlation function of DRGs with “photometric” redshifts in the range $2 < z < 3$. The results of this exercise are shown in Fig. 3.8. The thick green curve represents the mean angular correlation function and the 48 thin curves represent the

angular correlation functions estimated in the individual $0.8 \times 0.8 \text{ deg}^2$ regions. The red dots are the observational result of Quadri et al. (2008). At scales between 7 and 100 arcsec, our predictions overlap the observations quite well. At larger and smaller scales, they are low, although one or two of the mock surveys still come close to the observational data.

Quadri et al. (2008) fit line-of-sight projections of simple non-evolving double power-law models to the angular correlation data shown in Fig. 3.8 and conclude that a comoving correlation length of $10.6 \pm 1.6 h^{-1} \text{ Mpc}$ is needed to match the observations. They note that in the concordance ΛCDM cosmology, this is significantly larger than expected for *any* galaxy population with the observed abundance of DRG's. We confirm this for our own specific model: at $z = 2.24$ objects which satisfy the photometric criteria to be considered DRGs have a comoving correlation length (defined as the scale at which the 3-D spatial correlation function is unity) of $6.6 h^{-1} \text{ Mpc}$, significantly smaller than the Quadri et al. (2008) value. We have tested whether this apparent discrepancy could be due to the difference in redshift distributions between model and observed DRGs (see Fig. 3.2). We increase the abundance of DRGs in the redshift range $1.6 < z < 2$. by shifting the $J - K$ colour cut to 1.1 over this interval. This results in a total number density of 1.4 DRGs per sq.arcmin and a continuous redshift distribution over $1 < z < 3$ with no gap. Thus it reproduces the observed distributions well. However, model DRGs with photometric redshifts in $2 < z < 3$ show almost identical angular correlations to our original samples. Thus, for Gaussian photometric redshift errors, we conclude that our failure to match precisely the observed photometric redshift distribution has no significant effect on the predicted angular correlations. However, the errors in real photometric redshifts are far from Gaussian, so it remains possible that more realistic error distributions perturb the relation between angular and spatial correlations in a more significant way, as argued by Quadri et al. (2008)).

Alternatively, the difference in conclusions here and in Quadri et al. (2008) may stem from the fact that we emphasise the agreement of our model with the observed angular correlations over the central part of the measured range, and give less weight to disagreements on the largest and smallest scales, while Quadri et al. (2008) fit the shape of their measured angular correlations quite precisely and then use the correlation length as a measure of clustering strength. At $z = 2.24$, a comoving scale of $10.6 h^{-1} \text{ Mpc}$ corresponds to 540 arcsec, and so is in the range where the observed angular correlations are well above almost all of our mock catalogues. As a result, the DRG correlation length quoted by Quadri et al. (2008) is larger than that for our model DRGs. Given the noise expected for fields of the observed size (illustrated by the scatter among the thin lines in Fig. 3.8) it seems likely that a final resolution of this issue will need to wait for a survey of a substantially larger area.

3.4 The Descendants of High Redshift Galaxies

In the last section we showed that our galaxy formation simulation reproduces most of the observational properties of the LBGs, BXs and DRGs. The model may therefore provide a useful guide to the physical properties of these systems, as well as to their relations to each other and to lower redshift galaxy populations. We define the descendant of a high-redshift

Table 3.1: Comoving number density ($h^3 Mpc^{-3}$) of model LBGs, BXs, DRGs and their descendants

z	<i>LBGs</i>	<i>BXs</i>	<i>DRGs</i>
3	0.00143		
2	0.00142	0.00372	0.00061
1	0.00138	0.00366	0.00058
0	0.00121	0.00332	0.00050

Table 3.2: Satellite galaxy fraction among model LBGs, BXs, DRGs and their descendants

z	<i>LBGs</i>	<i>BXs</i>	<i>DRGs</i>
3	0.031		
2	0.235	0.035	0.235
1	0.446	0.386	0.346
0	0.484	0.490	0.386

galaxy population, for example the LBGs, to be the set of all galaxies at some lower redshift which have at least one LBG progenitor (which need not be their main progenitor). In the following, we maximise our statistics by selecting high-redshift populations from the full Millennium Simulation volume rather than from a mock catalogue. This can entrain slight differences with the results above because the full data are stored only at discrete epochs and we do not interpolate between them.

3.4.1 Number Density, Satellite Fraction and Stellar Mass Growth

Table 1 lists predictions from our simulation for the abundance of LBGs, BXs, DRGs and their descendants. The left column is the redshift. The LBG sample is selected as all objects in the MS volume at $z = 3.06$ which would satisfy the observational criteria to be an LBG, if seen on our past light-cone at this redshift. The LBG abundances at lower redshift then refer to the descendants of this population. The BX and DRG populations are similarly selected, but at $z = 2.2$. The abundance of LBG descendants changes very little from $z \sim 3$ to $z \sim 1$, but decreases by 12% by $z = 0$ as a result of mergers. The abundance evolution of BXs and DRGs is similar; there is little change until $z \sim 1$ followed by drops of 10% and 17% to the present day, respectively.

The fractions of model LBGs, BXs, DRGs and their descendants which are satellite galaxies (i.e. are no longer the central galaxy of their dark halo) are shown in Table 2. LBGs and BXs are almost all central galaxies, while 24% of DRGs are already satellite galaxies at the time when they are identified. The satellite fractions among the descendants increase rapidly and become comparable by $z \sim 1$: 45% for LBGs, 39% for BXs and 35% for DRGs. These fractions evolve more slowly at later times. At $z \sim 0$ around half of the descendants are satellite galaxies in all three samples. While DRGs had the largest satellite fraction when they were identified, their descendants actually have the lowest satellite fraction at $z = 0$.

Fig. 3.9 shows how the descendants of high-redshift galaxies grow in mass.. The solid

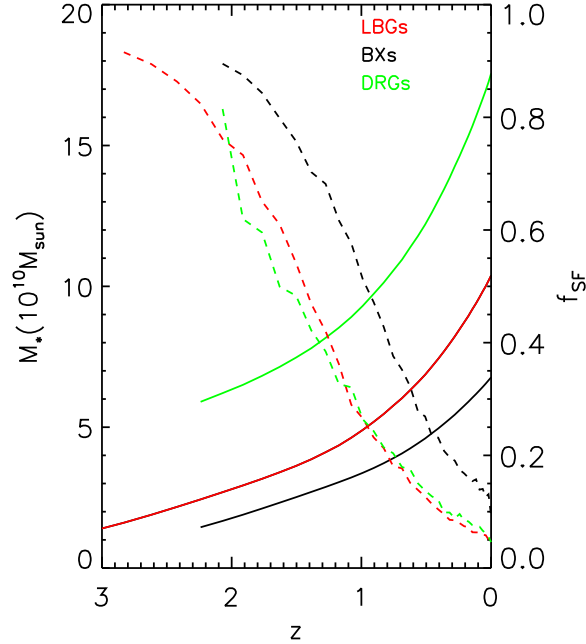


Figure 3.9: Stellar mass growth in the descendants of high-redshift galaxies. The left axis refers to the mean stellar masses of LBGs, BXs, DRGs and their descendants which are indicated by solid curves. The right axis refers to the fraction of the mass growth rate at each redshift which is due to star formation (the dashed curves). The x-axis is redshift. Red curves are for LBGs, black curves for BXs and green curves for DRGs.

curves indicate the evolution of the mean stellar mass of each population as a function of redshift. The red, black and green curves are for LBGs, BXs and DRGs, respectively. In all three cases the stellar mass increases relatively slowly until $z \sim 1$ and more rapidly thereafter. This reflects quiet star-formation-dominated growth at early times, followed by merger-dominated growth after $z \sim 1$. To see this more clearly, we also plot as dashed curves the fraction of the mass growth rate at each redshift which is due to star formation, $f_{SF} = \frac{\dot{M}_{SF}}{\dot{M}_*}$. Here \dot{M}_{SF} is the mean star formation rate while \dot{M}_* is the mean of the total stellar mass growth rate. At $z \sim 3$, almost 90% of the stellar mass growth in LBGs is due to star formation. This fraction drops with time, and mergers becomes comparable to star formation at $z \sim 1.5$. At the present day, only 5% of the growth in stellar mass of LBG descendants is due to star formation. BXs and their descendants behave in a similar way, star formation accounts for 90% of their stellar mass growth at the time they are identified, but this drops to around 50% by $z \sim 1$ and to only 10% at $z \sim 0$. At any given time, the effect of star formation is more important for BXs than for LBGs. Interestingly, the evolution of f_{SF} for DRGs is always close to that for LBGs. Stellar mass growth is dominated by star formation before $z \sim 1.5$ and by mergers thereafter. The long steady star-formation-dominated epoch between $z \sim 2.3$ and $z \sim 1.5$ reflects the fact that

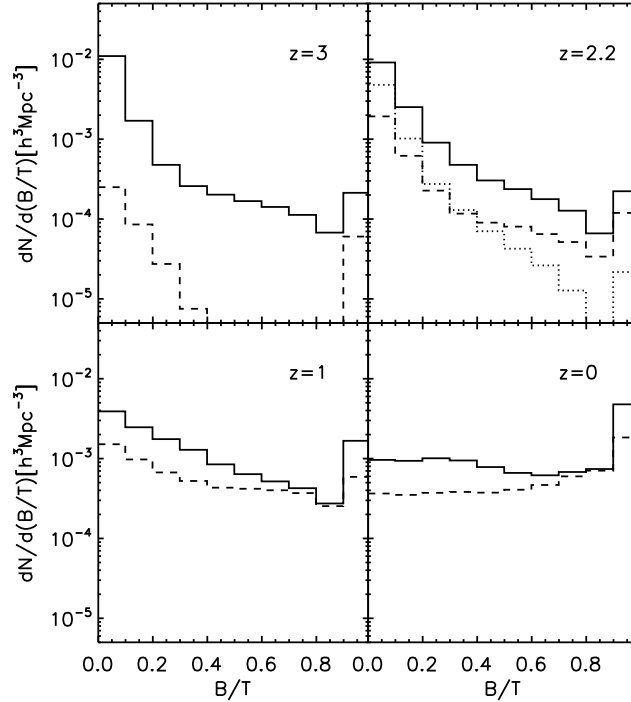


Figure 3.10: Distributions of bulge-to-total stellar mass ratio for model LBGs and their descendants. The corresponding redshifts are indicated on the upper right corner of each panel. The solid histograms are for all LBGs and their descendants, while dashed histograms show the fraction of each population which are satellite galaxies. The dotted histogram in the upper right panel represents the LBG descendants which would be classified as BXs at $z \sim 2.2$.

most DRGs in our simulation are highly obscured star-forming galaxies. Note that star formation in this figure includes the starburst mode during mergers. Gas-rich mergers can be an important growth mechanism even before $z \sim 1$.

3.4.2 Morphology

Fig. 3.10 shows distributions of bulge-to-total stellar mass ratio (B/T) for model LBGs and their descendants. When identified, most LBGs are disk-dominated ($B/T < 0.5$) systems. The fraction of disk-dominated LBGs remains almost unchanged until $z \sim 2$ and then decreases slowly to $z \sim 1$, showing that gas-rich major mergers are not a dominant mechanism. (The remnants of major mergers are assumed to be spheroids in our model.) This fraction decreases dramatically later on, and more than half of the descendants are bulge-dominated at $z \sim 0$. Indeed, more than a third are ellipticals with B/T greater than 98%. Given the small fraction of the $z \sim 0$ growth rate contributed by star formation (less than 10%) it is clear that the model predicts dry mergers to dominate the recent evolution of LBG descendants. The morphologies of satellite LBGs and satellite LBG-descendants are similar to those of their parent samples, gradually changing from disk-dominated to

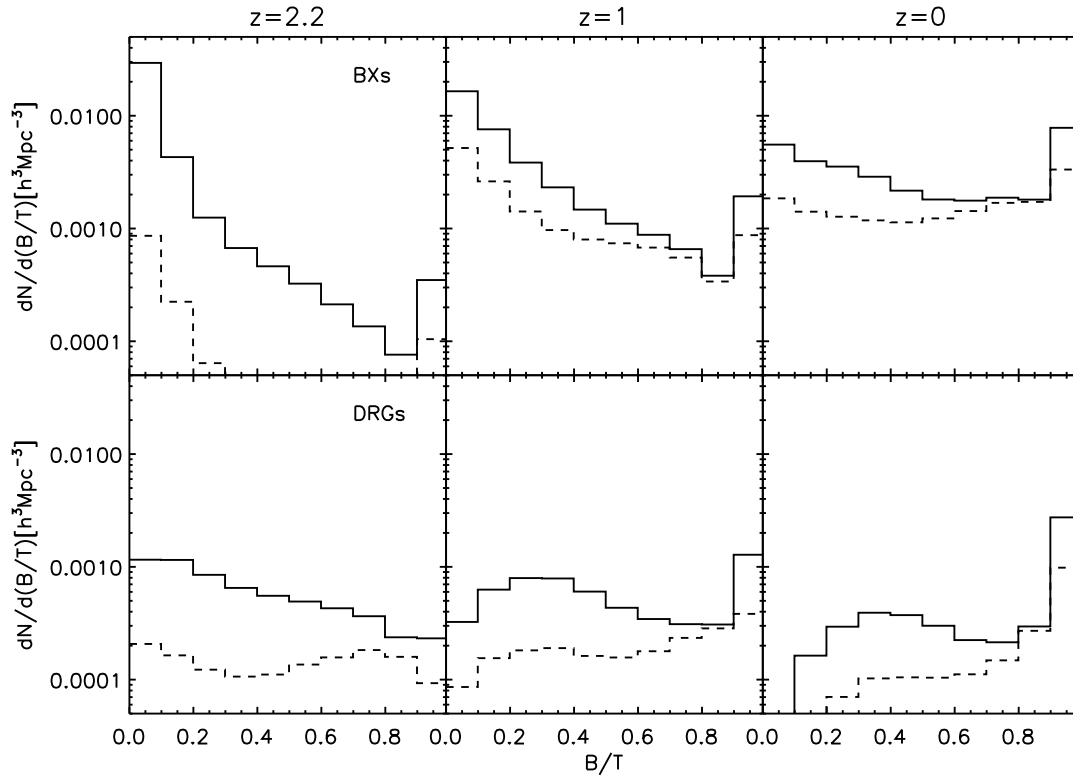


Figure 3.11: Distributions of bulge-to-total stellar mass ratio for BXs, DRGs and their descendants. The line-style coding of the histograms is the same as in Fig. 3.10. The corresponding redshifts are indicated at the top of each column.

spheroid-dominated as the population ages.

The distributions of bulge-to-total stellar mass ratio for model BXs, DRGs and their descendants are shown in Fig. 3.11. The BXs behave in a very similar way to the LBGs except that the fraction of disk-dominated systems is larger at all redshifts. Even at $z \sim 0$, around half of all BX descendants are disk-dominated. At the time of identification, most model DRGs are also disk-dominated. By $z \sim 1$ the fraction of pure disk systems among their descendants has dropped by a factor of two. By $z \sim 0$, ellipticals dominate the population of DRG descendants, accounting for 54% of the population; almost no pure disk descendants remain. Mergers clearly play a more important role in the evolution of DRG descendants than in the evolution of LBG and BX descendants.

3.4.3 Stellar Mass Functions

In Fig. 3.12 we plot stellar mass functions for model LBGs and their descendants and compare these with stellar mass functions for the galaxy population as a whole at each redshift. The LBGs cover a wide range in stellar mass, more than two orders of magnitude, with a peak at $10^{9.9} M_{\odot}$. As time goes by, the median stellar mass grows by an order of magnitude, becoming more massive than M^* at $z \sim 0$. Very few LBGs end up as

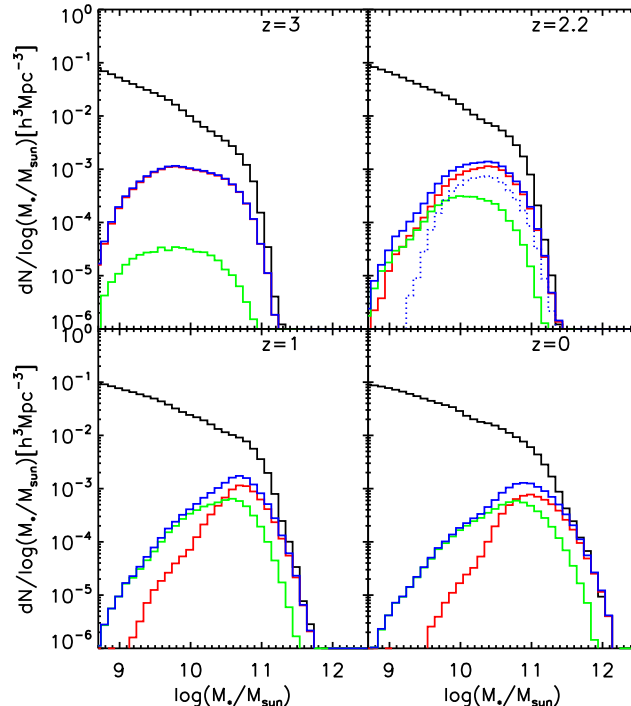


Figure 3.12: Abundances of model LBGs and their descendants as a function of stellar mass. Redshifts are indicated in the upper right corner of each panel. Blue histograms are for LBGs and their descendants, red and green histograms split these populations into central and satellite galaxies, respectively. For comparison, stellar mass functions for the galaxy population as a whole are overplotted using black histograms. The dotted blue histogram in the upper right panel shows those LBG descendants which would be identified as BXs at $z \sim 2.2$

central galaxies less massive than $10^{9.9} M_{\odot}$. Comparing to the overall stellar mass function at $z \sim 0$, we find that 88% of the most massive galaxies ($M_* > 10^{11.5} M_{\odot}$) are LBG descendants. For $M_* > 10^{11.0} M_{\odot}$ and $M_* > 10^{10.5} M_{\odot}$ the corresponding fractions are 34% and 15%, respectively. Thus, most very massive galaxies have at least one LBG as their progenitor. Since fewer than 30% of $z \sim 3$ galaxies with $M_* > 10^{11} M_{\odot}$ are identified as LBGs, many LBGs were accreted onto more massive non-LBG galaxies during their evolution to low redshift.

The stellar mass functions of satellite galaxy LBGs and central galaxy LBGs are quite similar, but satellite and central galaxies have rather different mass distributions in the descendant populations. The peak of the distribution for satellite galaxies is about a factor of two below that for central galaxies by $z = 0$. Satellite descendants grow less rapidly because almost all mergers occur onto central galaxies and gas cools only onto central galaxies in our model. As a result there are also many more satellites in the low-mass tail of the descendant population.

Stellar mass functions for model BXs, DRGs and their descendants are shown in Fig. 3.13. The results for BXs are again quite similar to those for LBGs and the mass functions peak

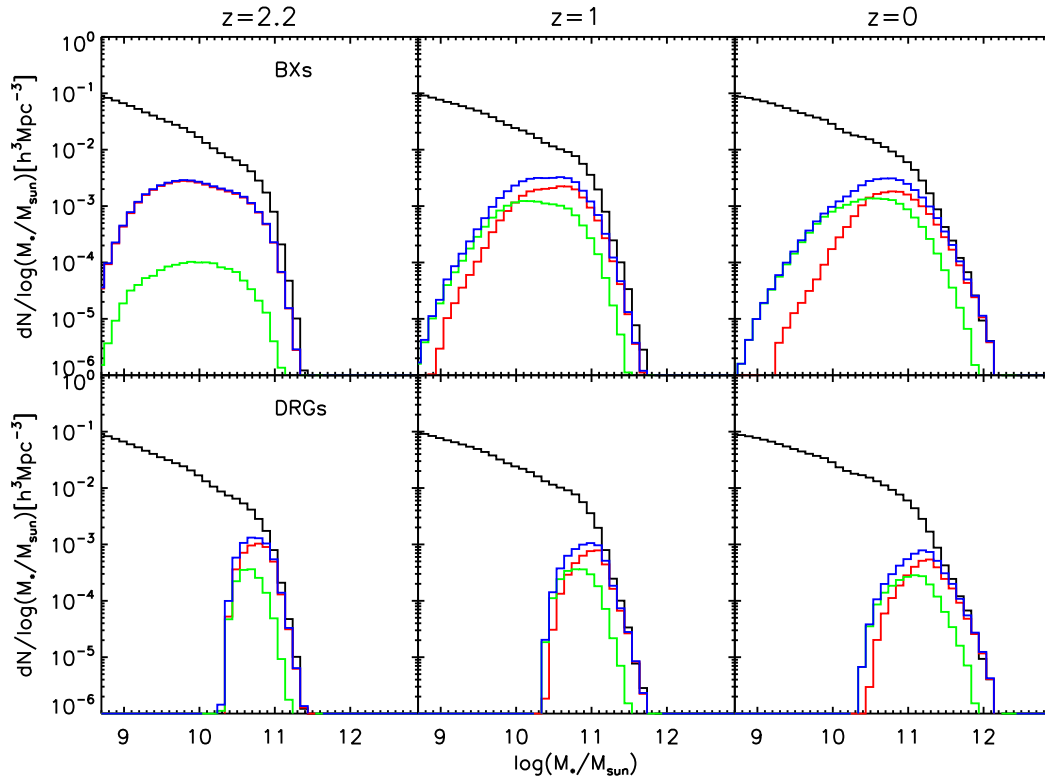


Figure 3.13: Abundances of model BXs, DRGs and their descendants as a function of stellar mass. The histograms use the same colour coding as in Fig. 3.12.

at the same value. The stellar mass of BX descendants is shifted to slightly lower values than that of LBG descendants and peaks at $10^{10.7} M_{\odot}$ at $z \sim 0$. At this time 86% of galaxies with $M_* > 10^{11.5} M_{\odot}$ are BX descendants and 50% of galaxies with $M_* > 10^{11} M_{\odot}$. For comparison, only 30% of $z \sim 2$ galaxies with $M_* > 10^{11} M_{\odot}$ are classified as BXs. Unlike the LBGs and BXs, model DRGs span a narrow range of stellar mass at the time they are identified, peaking at $10^{10.7} M_{\odot}$. By $z \sim 0$ the typical mass of their descendants has increased only by a factor of 3, but almost no descendant is less massive than the Milky Way. DRGs account for more than 65% of galaxies more massive than $10^{11} M_{\odot}$ at $z \sim 2.2$ and their descendants at $z = 0$ account for more than 84% of galaxies more massive than $10^{11.5} M_{\odot}$. Many LBGs and BXs are accreted onto massive DRG descendants by $z \sim 0$.

3.4.4 Colour-Stellar Mass Distributions

In Fig. 3.14 we show a scatter plot of rest frame $B - V$ colour (AB system) against stellar mass for model LBGs and their descendants, as well as for other galaxies at the corresponding redshifts. When identified, the LBGs are mostly blue galaxies, and none are part of the small red population which already exists at $z \sim 3$. The blue fraction decreases with time. Although their stellar mass has increased by a factor of 2 by $z \sim 2.2$, most of the descendants, especially the central descendants, are blue, indicating a high specific star

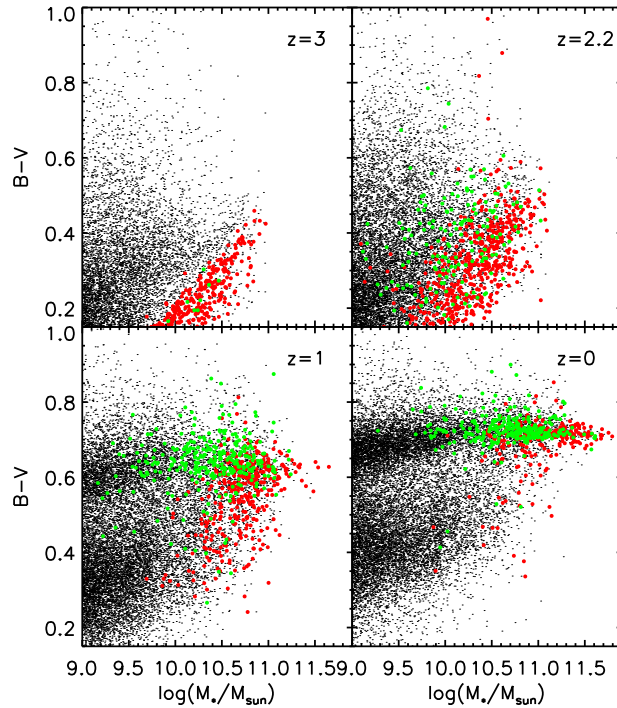


Figure 3.14: B-V colour vs. stellar mass for model LBGs and their descendants at the redshifts indicated in each panel. Red points denote central LBGs and central LBG descendants, while green points denote satellite LBGs and satellite descendants. Black dots indicate other galaxies at the same redshift.

formation rate. At $z \sim 1$ a significant fraction of the descendants lie on the red sequence. These objects are primarily satellite galaxies where star formation is suppressed. By $z \sim 0$, most of the descendants, even central descendants, have moved to the red sequence.

Fig. 3.15 shows similar scatter plots of colour against stellar mass for model BXs, DRGs and their descendants. Yet again the behaviour of the BXs is very similar to that of the LBGs: When selected they are almost all blue galaxies which then gradually move to the red sequence. There are relatively more blue central BX descendants at $z \sim 0$ than blue central LBG descendants. Unlike the LBGs and BXs, most DRGs reside at the massive end of the red sequence in the stellar mass colour diagram, with a typical B-V colour of 0.5. As time goes by, the colour of DRGs gets even redder and they remain on the red sequence. There is almost no difference in colour between their central and satellite descendants.

3.4.5 The Dark Halos of LBGs

Fig. 3.16 shows mass distributions for the dark matter halos of model LBGs and their descendants. The dark matter halo here is taken to be the friends-of-friends halo defined by linking together dark matter particles separated by less than 0.2 of the average interparticle separation (Davis et al. 1985). Each FOF halo typically contains several galaxies: one central galaxy and some satellites. Thus, these histograms may count a given halo more

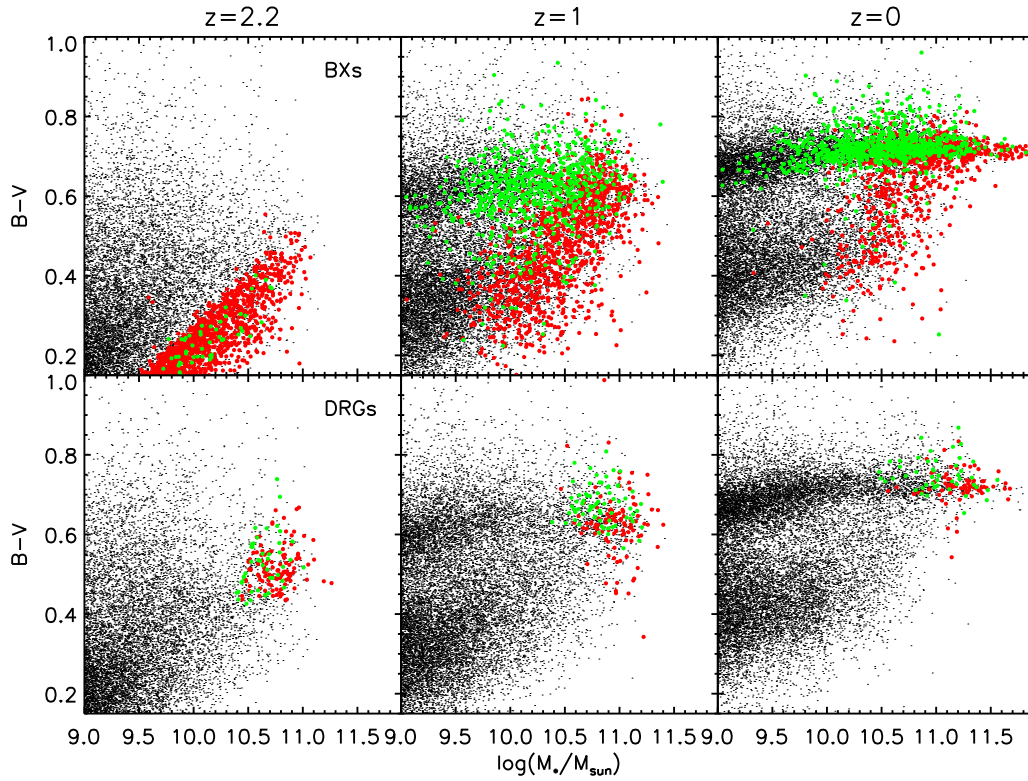


Figure 3.15: B-V colour vs. stellar mass for model BXs, DRGs and their descendants using the same colour coding as Fig. 3.14.

than once if it contains several LBGs or LBG descendants. The peak of the halo mass distribution is at $10^{12} M_{\odot}$ at $z \sim 3$ and moves to $10^{13.4} M_{\odot}$ by $z \sim 0$, corresponding to the mass of a large galaxy group. At high redshift, central and satellite LBGs live in halos of similar mass, but at lower redshifts satellite descendants tend to live in more massive halos than central descendants. In fact, the typical present-day environment of central LBG descendants is a poor galaxy group with mass $\sim 10^{13} M_{\odot}$, while the typical environment of the satellite descendants is a cluster with mass $\sim 10^{14} M_{\odot}$.

Fig. 3.17 shows halo mass distributions of model BXs, DRGs and their descendants. As before, BXs are distributed in a similar way to LBGs, although their halos are shifted to noticeably lower masses, peaking at $10^{11.8} M_{\odot}$ at $z \sim 2$ and then shifting to $10^{12.6} M_{\odot}$ by $z \sim 0$. For DRGs, the halo masses are larger, peaking at $10^{12.6} M_{\odot}$ at $z \sim 2.2$ and shifting to $10^{13.4} M_{\odot}$ by $z \sim 0$. Note that the distribution of halo masses for DRGs is quite narrow compared to that for BXs, consistent with their narrower distribution in stellar mass (Fig. 3.13). The satellite descendants of BXs and DRGs also more likely be found in more massive halos than their central descendants.

Blue histograms in the highest redshift panels of Figs 3.16 and 3.17 show halo mass functions at the redshifts where LBGs, BXs and DRGs are identified. By comparing these with the red histograms referring to central galaxies, it can be seen that the assumption of most previous work (e.g. Conroy & Wechsler 2008), that LBGs or BXs can be identified

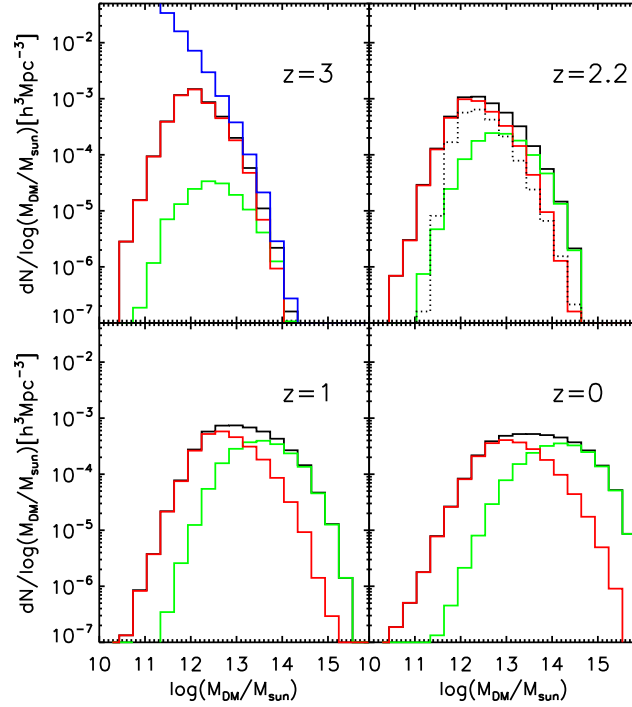


Figure 3.16: Abundances of model LBGs and their descendants as a function of dark halo mass. Black histograms are for all objects, while red and green histograms split the sample into central and satellites galaxies, respectively. The dotted black histogram in the upper right panel shows the LBG descendants which would be classified as BXs, while the red dotted histogram shows the subset of these objects which are also central galaxies. Dark halos are multiply counted in these histograms if they contain more than one LBG or LBG descendant. The blue histogram in the $z = 3$ panel is the abundance of dark halos regardless of their galaxy content. The ratio of the red and blue histograms thus gives the fraction of dark halos at each mass which has an LBG central galaxy.

as the central galaxies of all halos above some threshold mass at the relevant redshift, is very poorly obeyed by our model. For example, fewer than half the halos of any mass have a central galaxy classified as LBG or BX. Indeed, we predict the probability that the central galaxy enters these observational categories to *decrease* with increasing halo mass. In contrast, the probability that the central galaxy of a $z = 2.2$ halo is classified as a DRG increases monotonically with halo mass, exceeds 50% for halo masses above $10^{13.5} M_{\odot}$ and approaches unity at high mass.

3.4.6 Descendant Correlations

In a previous section we showed that the correlation functions of our model high-redshift galaxies match observation quite well. Here we look at the evolution of their clustering. In Fig. 3.18, we plot 3D correlation functions as a function of redshift. For all three populations, the clustering of descendants gets stronger towards lower redshift. For LBG

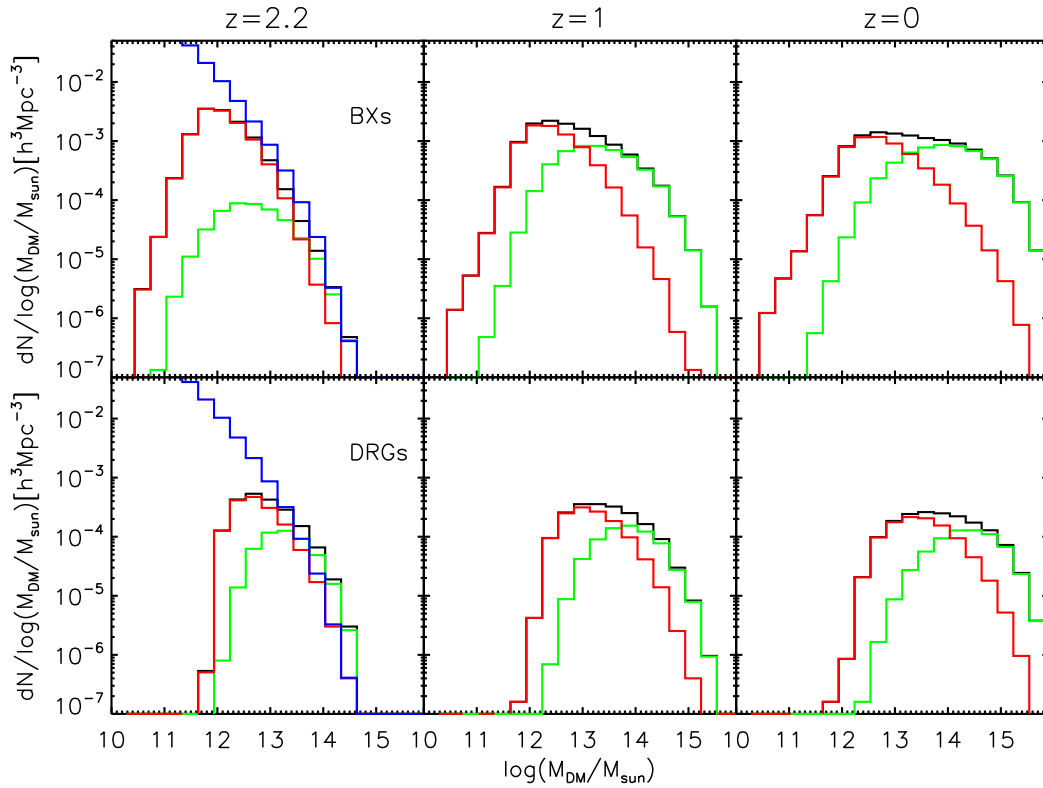


Figure 3.17: Abundances of BXs, DRGs and their descendants as a function of dark halo mass. The colour coding is the same as in Fig. 3.16. The blue histograms in the $z = 2.2$ panels show the abundance of dark halos independent of their galaxy content.

descendants, the correlation length is $9.7h^{-1}\text{Mpc}$ at $z = 0$, as estimated from a power law fit over $3h^{-1}\text{Mpc} < r < 10h^{-1}\text{Mpc}$. This is about twice the comoving value at $z \sim 3$. The difference between $z \sim 3$ and $z \sim 2.2$ is quite small compared to changes at later times. At low redshifts there is an obvious turn-up in clustering strength at small scales, indicating the increasing importance of satellite galaxies which we already noted above.

The clustering of BX descendants increases similarly with time, but is always weaker than that of LBG descendants. Their correlation length reaches $8.1h^{-1}\text{Mpc}$ at $z = 0$. The turn-up at small scales also shows up for BX descendants at low redshift. The comoving correlation length of DRGs evolves less than that of LBGs and BXs, reaching $10h^{-1}\text{Mpc}$ at $z = 0$. Indeed the correlations of DRG descendants and LBG descendants are almost identical at $z = 0$. For all three populations, the present-day correlation lengths are larger than for L^* galaxies, as might be expected given that their typical stellar masses are higher than M^* .

It is interesting to check whether galaxy merging has any significant effect on these descendant correlations. We have tested this by tagging the dark matter particles associated with each BX galaxy at the time it is identified, and then calculating correlations for this particle set at later redshifts. The results are indicated by stars in the central panel of Fig. 3.18. Clearly, this procedure produces results which are indistinguishable from

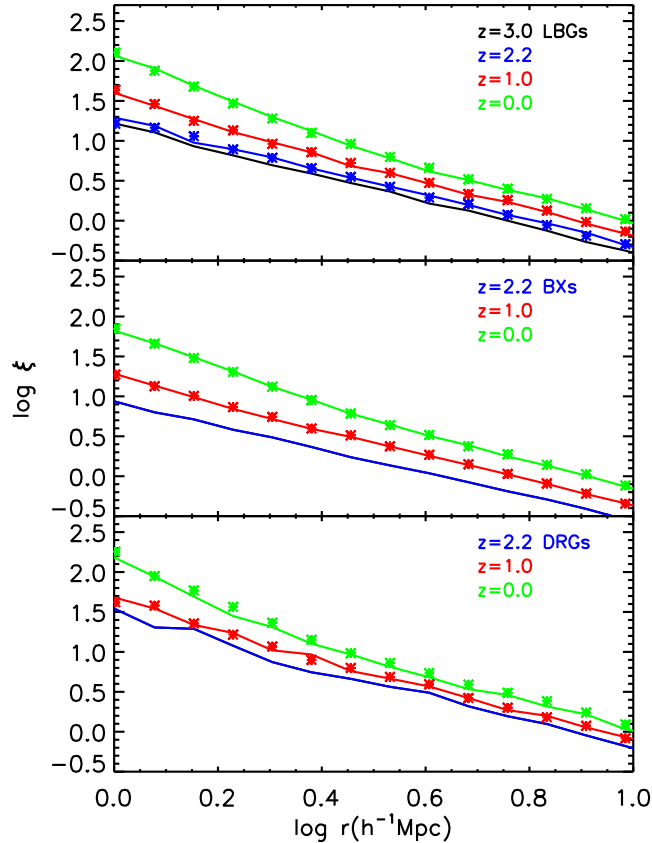


Figure 3.18: 3D correlation functions for LBGs, BXs, DRGs and for their descendants. Redshifts are indicated at the right upper corner of each panel using the appropriate colour. Solid curves represent the results for full samples of LBGs, BXs, DRGs or their descendants. The dotted curve in the upper panel represents the correlation for LBG descendants which are BXs at $z \sim 2.2$. Stars show correlations at later times of the dark matter particles originally identified as LBGs, BXs and DRGs, and so represent how correlations would evolve in a non-merger scenario.

those obtained by following BX descendants through the *Millennium Simulation* galaxy trees. Results for LBGs and DRGs are similar. This validates one part of the simplified recipe adopted by Conroy & Wechsler (2008) and Quadri et al. (2007b) when estimating clustering for the descendants of high redshift galaxy populations based on simple HOD assignments of the high-redshift objects to dark halos. Valid results from such recipes will still, of course, require that they assign galaxies to the correct high-redshift halos, and the results of Section 3.4.5 suggest that this was not the case, at least for LBGs and BXs.

3.4.7 Relation between LBGs, BXs and DRGs

At $z \sim 2.2$, only 0.8% of model BXs and 10% of LBG descendants are classified as DRGs. Conversely, 4.7% and 25% of DRGs are identified as BXs and LBG descendants, respec-

tively. The overlap between DRGs and BXs or LBG descendants is thus quite small.

In contrast, LBGs and BXs are closely correlated. Fully 45% of LBG descendants at $z \sim 2.2$ are identified as BXs. We illustrate the properties of these particular LBG descendants (which we refer to as LBG-BXs in the following) in the right upper panels of Fig. 3.10, Fig. 3.12 and Fig. 3.16 using dotted histograms. Their distribution in stellar mass is similar to that of all LBG descendants, but with fewer galaxies in the low-mass tail, which consists of satellite galaxies and small central galaxies. Very few satellite galaxies have enough star formation to qualify as BXs in our model, and only 5% of LBG-BXs are satellites, as compared to 23.5% of all LBG descendants. Some of the more massive LBG descendants fail to be identified as BXs because they are rich in gas and heavy elements, and the associated extinction pushes them outside the BX detection window, even though they are strongly star-forming. LBG-BXs are more massive than the overall BX population at $z \sim 2.2$, and this is reflected in their stronger clustering, as shown in the upper panel of Fig. 3.18. Their clustering is similar to that of LBG descendants in general. A related coincidence shows up in the halo mass distributions which are very similar for the two populations (Fig. 3.16). Since mergers play a minor role in the evolution of LBG descendants before $z \sim 2.2$, the LBG-BXs are, as expected, mainly disk-dominated.

3.5 Summary and Discussion

We have used the De Lucia & Blaizot (2007) model for galaxy formation within the *Millennium Simulation* to explore the likely physical nature of observed high-redshift galaxies, specifically Lyman Break Galaxies, BX galaxies and Distant Red Galaxies, and their likely descendants at lower redshift. We first built mock catalogues in order to compare observed high-redshift galaxies with similarly selected objects in the simulation. We then used the full galaxy catalogue from the simulation to study the descendants of the high-redshift populations. We found it necessary to modify the original DLB07 dust model in order to match the abundance and colour of the observed high-redshift populations,

Impressively, with a proper dust model it is possible to match the observed abundances, redshift distributions and clustering of all three high-redshift populations in a model which also fits the properties of low-redshift galaxies. The descendants of all three populations become more strongly clustered at lower redshifts, and all are more clustered than M^* galaxies today. A turn-up in clustering strength at small scales is evident at $z \sim 0$, which reflects the high satellite fraction among the descendants. The clustering of DRGs is the least consistent with observation. Angular correlations are well reproduced on scales between 7 and 100 arcsec but our model appears more weakly clustered than real DRGs on both smaller and larger scales. This results in an estimated correlation length for the observed sample which is larger than that of our model DRGs. Our results show the expected scatter in angular correlation estimates to be quite large for areas as small as that currently observed, so a final judgement on this issue will require significantly larger observational surveys.

Together, model DRGs and BXs account for only 30% of the strongly star-forming galaxies ($\dot{M}_* > 20M_\odot/yr$) at $z \sim 2$. Most of the rest are gas- and metal-rich systems which are strongly obscured. In contrast, the model suggests that only 15% of all galaxies with

$M_* > 10^{11} M_\odot$ at $z \sim 2$ (most of which do indeed have high star formation rates) are missing in current optical and near-infrared surveys. Interestingly, the model predicts most DRGs to be star-forming galaxies. Their average SFR is even higher than those of LBGs and BXs, and they account for more than 65% of the galaxies with $M_* > 10^{11} M_\odot$ at $z \sim 2.2$. There is rather little overlap between these star-forming DRGs and BXs or LBG descendants. On the other hand, half of all LBG descendants are identified as BXs at $z \sim 2.2$. The physical properties and the clustering of these LBG-BXs are quite similar to those of other LBG descendants. These consist of three classes of galaxy: smaller galaxies where the potential is too shallow to retain the gas expelled by supernova feedback, satellite galaxies where the interstellar gas has been exhausted, and gas-rich galaxies where the dust extinction is strong.

Our simulation roughly reproduces the observed relation between stellar mass and gas-phase metallicity for local star-forming galaxies and for BX galaxies, but the gas-phase metallicities predicted for LBGs, although slightly lower than for BXs, are well above the values estimated for real LBGs by Maiolino & et al. (2008).

Most model LBGs, BXs and DRGs are disk-dominated systems, residing at the centres of their own halos. LBGs and BXs are selected as blue galaxies and so exclude the significant population of red galaxies which is already present at these redshifts. Nevertheless, by $z \sim 0$ at least half of their descendants are bulge-dominated and red. The typical stellar masses of LBGs and BXs increase by an order of magnitude by $z \sim 0$, whereas DRG stellar masses increase by a smaller factor, ~ 3 . Star formation is the main driver of growth before $z \sim 1$, then mergers become dominant. Most low-redshift massive galaxies ($M_* > 10^{11} M_\odot$) descend from at least one of these high redshift populations. Correspondingly, most descendants are massive galaxies living in massive dark matter halos today. Many of them are satellite galaxies in galaxy clusters. The central galaxies in rich clusters ($M > 10^{14.7} M_\odot$) typically have 8.4 LBG, BX or DRG progenitors, and on average the stars present in the high-redshift galaxies account for around 50% of the current stellar mass. Thus while the observed high-redshift galaxies have contributed significantly to today's massive galaxies, it appears that the relation between the two populations is quite complex.

Galaxy Formation Efficiency

Abstract

For any assumed standard stellar Initial Mass Function, the Sloan Digital Sky Survey (SDSS) gives a precise determination of the abundance of galaxies as a function of their stellar mass over the full stellar mass range $10^8 M_\odot < M_* < 10^{12} M_\odot$. Within the concordance Λ CDM cosmology, large high-resolution simulations give precise halo abundances as a function of mass and redshift for all halos within which galaxies can form. Under the plausible hypothesis that the stellar mass of a galaxy is an increasing function of the maximum mass ever attained by its halo, these results combine to give halo mass as a function of stellar mass. The result is in good agreement with direct measurements of mean halo mass as a function of stellar mass from gravitational lensing analysis of SDSS data, providing additional evidence of the overall consistency of the Λ CDM cosmology. For $M_* = 6 \times 10^{10} M_\odot$, the stellar mass usually assumed for the Milky Way, the implied halo mass is $2.6 \times 10^{12} M_\odot$, larger than most (but not all) recent direct estimates, but consistent with inferences from the MW/M31 Timing Argument. The efficiency of galaxy formation, defined as the fraction of the baryons associated with the halo which are present in stellar form, reaches a maximum of 20% at masses slightly below that of the Milky Way and falls rapidly at both higher and lower masses. These conversion efficiencies are much lower than in most recent high resolution simulations of the formation of spiral galaxies, showing that these are not yet viable models for the formation of typical members of the galaxy population. The predicted Tully-Fisher relation is consistent with recent observations, indicating that galaxy luminosity functions and the Tully-Fisher relation can be reproduced simultaneously in the context of the Λ CDM cosmology.

4.1 Introduction

It has been realized for several decades that baryons do not dominate the mass in the Universe. Instead, only about 15% of the total mass is in the form of baryons, while the remaining 85% is dark matter. In the concordant Λ CDM paradigm, galaxies form by cooling and condensation of the baryons within hierarchically formed dark matter halos (White & Rees 1978). The dark matter halo mass function is predicted to be close to a power law (Press & Schechter 1974), which has been confirmed with various cosmic simula-

tions (see below). The observed galaxy stellar mass function, however, bends down strongly at both high and low mass ends compared to this power law. This implies that the fraction of baryons locked in stars is quite different for dark matter halos of different mass. The mass-to-light ratio varies from about a hundred (M_{\odot}/L_{\odot}) for galaxies like the Milky Way, to several hundred (M_{\odot}/L_{\odot}) for dwarf galaxies and galaxy clusters. White & Frenk (1991) pointed out that supernova feedback can expel gas from shallow potential wells and reduce the star formation efficiency in low mass galaxies (Dekel & Silk 1986; Keres et al. 2009). Recent work shows that AGN feedback is able to suppress gas cooling and regulate the star formation in massive galaxies (Croton et al. 2006; Bower et al. 2006; Somerville et al. 2008).

Under the assumption of a one-to-one monotonic correspondence between the luminosity of a galaxy and its halo/subhalo mass, the two can be linked by matching galaxy luminosity functions with halo mass functions. This method has been adopted by Vale & Ostriker (2004) and then extended to match galaxy stellar mass functions and halo mass functions or circular velocity functions by Conroy et al. (2006), Shankar et al. (2006), Baldry et al. (2008), and Conroy & Wechsler (2008). After establishing the relationship between the galaxy stellar mass and halo mass and assuming a universal baryonic fraction, it is easy to estimate the fraction of baryons in the form of stars as a function of halo mass or galaxy stellar mass. Previous work has estimated this fraction to be around 20% – 35% (Marinoni & Hudson 2002; Mandelbaum et al. 2006; Baldry et al. 2008; Conroy & Wechsler 2008).

Here we use the precise stellar mass function of galaxies derived from the most recent SDSS data (Li & White 2009), and the precise dark matter halo mass function obtained by combining the Millennium Simulation (MS-I) (Springel et al. 2005b) and the Millennium II Simulation (MS-II) (Boylan-Kolchin et al. 2009), to derive the relation between the galaxy stellar mass and the dark matter halo mass to higher accuracy than was previously possible. This gives galaxy formation efficiency as a function of dark matter halo mass. We compare our derived dark matter halo masses of typical galaxies to those inferred from observations and discuss the constraints on hydro-simulations of galaxy formation.

We briefly describe the two Millennium simulations, the definition of dark matter halos and their masses in Sec. 4.2. The relation between galaxy stellar mass and dark matter halo mass is derived in Sec. 4.3. In this section, we also compare the predicted halo mass as a function of stellar mass with observations, we discuss our model constraint on galaxy formation simulations and we revisit the problem of simultaneously reproducing the luminosity function and the Tully-Fisher relation in a hierarchical cosmology. Conclusions and a discussion of our results are presented in Sec. 4.4

4.2 Dark Matter Halos

Both the *Millennium Simulation* and the *Millennium II Simulation* adopt the concordance Λ CDM cosmology, consistent with a combined analysis of the 2dFGRS (Colless & et al. 2001) and the first-year WMAP data (Spergel et al. 2003). The cosmological parameters are $\Omega_m = 0.25$, $\Omega_b = 0.045$, $h = 0.73$, $\Omega_{\Lambda} = 0.75$, $n = 1$, and $\sigma_8 = 0.9$, where the Hubble constant is parameterized as $H_0 = 100h \text{ km s}^{-1} \text{ Mpc}^{-1}$. Both simulations trace 2160^3 dark

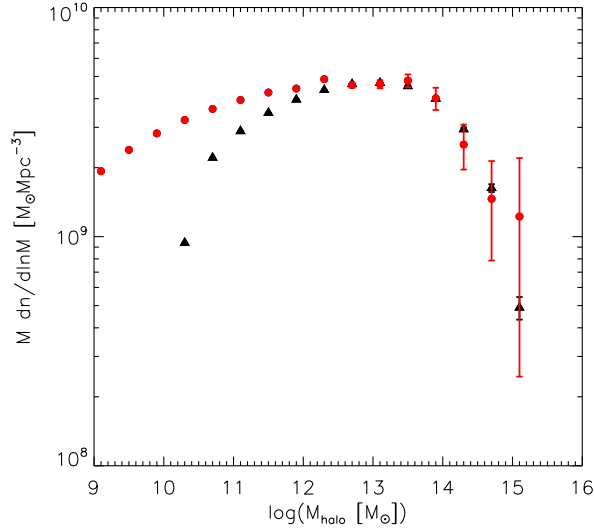


Figure 4.1: Dark matter halo mass functions where “halo” is defined to include both main subhalos and smaller subhalos. The halo mass is defined as the maximum mass, M_{halo} , the dark matter subhalo has ever attained. The black triangles are for the MS-I and the red dots are for the MS-II. Poisson errors are shown for both of the simulations

matter particles from $z \sim 127$ to $z \sim 0$. The simulations are carried out in boxes of side $500 h^{-1} \text{ Mpc}$ and $100 h^{-1} \text{ Mpc}$ for the MS-I and MS-II, respectively, corresponding to particle masses of $8.6 \times 10^8 h^{-1} M_{\odot}$ and $6.8 \times 10^6 h^{-1} M_{\odot}$. The large volume of the MS-I enables one to study even the rare, massive cD galaxies in clusters, while the excellent mass resolution of the MS-II can resolve the dark matter halos predicted to host the faintest known dwarf galaxies.

At each output time-step, the simulations identify friend-of-friend (FOF) groups on the fly by linking together particles separated by less than 0.2 of the mean interparticle separation (Davis et al. 1985). A SUBFIND algorithm (Springel et al. 2001) was then applied to each FOF group as a post-processing step to identify a disjoint set of self-bound subhalos, which represent locally overdense and dynamically stable regions within larger virialized halos. A main subhalo is defined as the largest self-bound part of a FOF group, in practice the leftovers after removing all the substructures and the unbound particles. Subsequently, merger trees were built by linking each subhalo/halo from a given output time to one and only one descendant at the following output time. We refer readers to Springel et al. (2005b) and Boylan-Kolchin et al. (2009) for a more detailed description of these simulations.

In this work, we use both the main subhalos and the smaller subhalos to calculate the dark matter halo mass function. For each FOF group, we define its center using the minimum of the gravitational potential well and define the virial radius, R_{vir} , as the radius that encloses a mean overdensity of 200 times the critical value. The mass within R_{vir} is

defined as the virial mass:

$$M_{halo} = \frac{100}{G} H^2(z) R_{vir}^3 \quad (4.1)$$

The mass of a main subhalo is defined as its current virial mass, while the mass of a subhalo is defined as its virial mass at the time step just before it gets accreted onto a larger system, i.e. when it was last a main subhalo. Hereafter, we refer to both main subhalos and smaller subhalos as halos. We show in Fig.4.1 the dark matter halo mass functions at redshift 0. The black triangles are the halo mass function for the MS-I, while the red dots are from the MS-II. The two simulations converge above $10^{12.3} M_{\odot}$. Below this threshold, the MS-II lies systematically above the MS-I, which we attribute to its much improved mass resolution. In the following, we combine the part of the MS-I mass function with $M_{halo} > 1.9 \times 10^{12} M_{\odot}$ with the part of the MS-II with $M_{halo} < 1.9 \times 10^{12} M_{\odot}$ to represent the overall dark halo mass function.

4.3 Galaxy Formation Efficiency

4.3.1 Connecting Galaxies to Dark Matter Halos

We connect stellar mass and its dark halo mass by assuming a one-to-one and monotonic relationship between them. Previous studies (Gao et al. 2004; Vale & Ostriker 2006; Wang et al. 2006; Berrier et al. 2006) show that the halo mass at the time of infall is more strongly related to the galaxy properties than is current subhalo mass, because subhalos experience mass-loss due to tidal stripping, while the galaxies in their cores are much less affected by tidal forces. We include both the main halos and the subhalos in this study and define their masses as described above.

In practice, for a given stellar mass M_* , if the number density of the dark matter halos with mass $> M_h$ matches the number density of the galaxies with mass $> M_*$

$$N(> M_h) = N(> M_*), \quad (4.2)$$

then we assume galaxies with M_* reside in dark matter halos with masses M_h .

Here we take the most recent observational measurement of the galaxy stellar mass function presented by Li & White (2009). This was based on a complete and uniform sample of almost half a million galaxies from the Sloan Digital Sky Survey data release 7 (SDSS DR7) (York et al. 2000; Abazajian & Sloan Digital Sky Survey 2008), which extends over almost four orders of magnitude in stellar mass ($10^8 M_{\odot} - 10^{11.7} M_{\odot}$). A detailed description of the measurement of the galaxy stellar mass function can be found in Li & White (2009).

We show the derived relation between the galaxy stellar mass and the dark matter halo mass in Fig. 4.2. The solid curve uses SDSS DR7 data over the stellar mass range from $10^{8.4}$ to $10^{11.7} M_{\odot}$, which corresponds to dark matter halo masses from $10^{10.7}$ to $10^{15} M_{\odot}$. We extrapolate this relation to $10^6 M_{\odot}$ at the low mass end and to $10^{12} M_{\odot}$ at the high mass end (dashed curve). Galaxies with mass around $10^6 M_{\odot}$ are expected to reside in dark matter halos with mass $\sim 10^{10} M_{\odot}$, well above the resolution limit of the MS-II. At the high mass end, the stellar mass of a central galaxy becomes very insensitive to its dark matter halo mass, indicating a suppression of star formation in the core of halos more massive than $\sim 10^{13} M_{\odot}$.

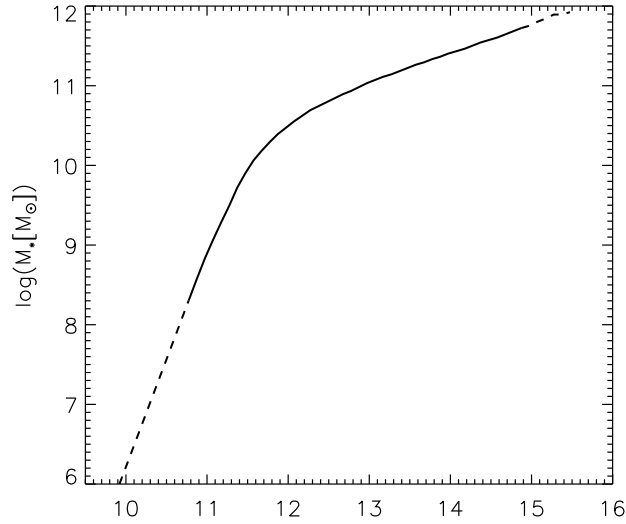


Figure 4.2: Stellar mass vs. dark matter halo mass relation. The solid curve is obtained by matching the galaxy number densities from SDSS DR7, to the dark matter halo number densities with the combination of the MS-I and the MS-II. The dashed curve is the extrapolation of this relation to $10^6 M_\odot$ and to $10^{12} M_\odot$ at the low and high mass end, respectively.

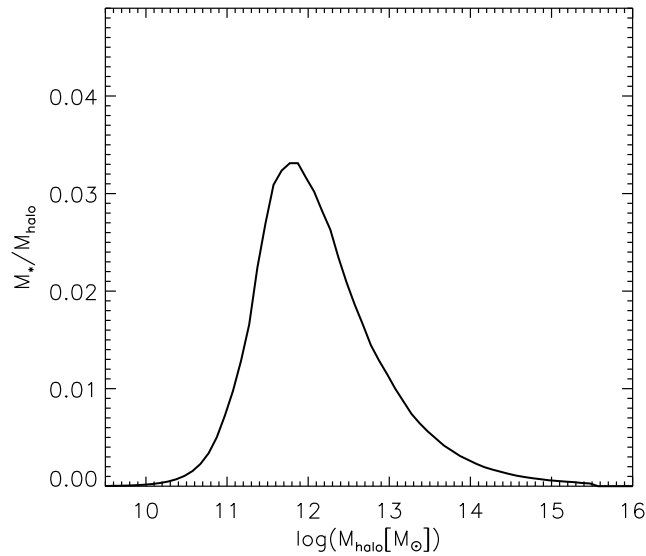


Figure 4.3: Stellar-mass-to-halo-mass ratio as a function of the halo mass.

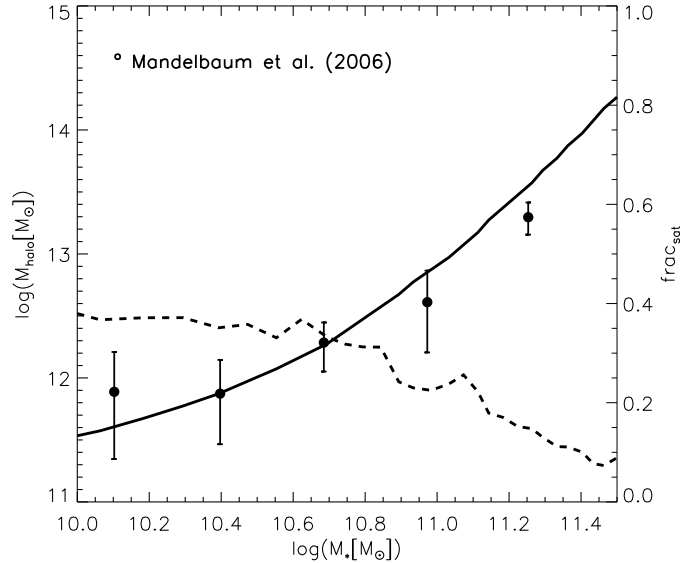


Figure 4.4: Dark matter halo mass as a function of stellar mass. The solid curve is the model prediction. Circles are estimates from weak lensing (Mandelbaum et al. 2006). Error bars show 95% confidence ranges. The dashed curve represents the satellite fraction as a function of stellar mass.

In Fig. 4.3 we show the stellar-mass-to-dark-halo-mass ratio, which is analogous to the light-to-mass ratio, as a function of dark matter halo mass. This ratio reaches its maximum in halos with mass $10^{11.8} M_{\odot}$, slightly less massive than the halos hosting L^* galaxies. The peak value is around 3.3%. The ratio drops very fast both at the low mass end and at the high mass end: $M_*/M_h < 0.015\%$ in dark matter halos with mass $\sim 10^{10.3} M_{\odot}$ and $M_*/M_h \sim 0.08\%$ in clusters with $\sim 10^{14.8} M_{\odot}$ (though note that in the latter case the stellar mass refers only to the central galaxy).

4.3.2 Dynamical Mass of the Milky Way

We now focus on galaxies with stellar mass between $10^{10} M_{\odot}$ and $3 \times 10^{11} M_{\odot}$ and show the halo mass vs. stellar mass relation in Fig. 4.4. The solid curve is our prediction and the circles show data obtained using the gravitational lensing measurements (Mandelbaum et al. 2006) for central galaxies. The data consisted of 351,507 galaxies from SDSS, including both early and late type galaxies in the mass range of $[0.7 \times 10^{10} M_{\odot}, 4 \times 10^{11} M_{\odot}]$. The error bars indicate 95% confidence intervals. Our results agree very well with these data, although there exist some discrepancies at the high mass end. The stellar masses used in Li & White (2009) were estimated by Blanton & Roweis (2007) based on the photometric properties of SDSS galaxies, while the masses of Mandelbaum et al. (2006) were estimated by Kauffmann et al. (2003b) based on the SDSS specstropy. The former is smaller than the latter by just under 0.2 dex in the mass range relevant here (see Fig. 17 of Blanton & Roweis (2007) and Fig. A1 of Li & White (2009)). This pushes the data points to the left and leads to a better agreement with our estimates. The dark matter halo mass is higher

in Mandelbaum et al. (2006) by 35%. This effect, however, may be compensated by the fact that they can underestimate the halo mass by a factor of two in their “scatter case” (Mandelbaum et al. 2005). The inclusion of satellite galaxies in our model may also lead to an overestimate of the halo masses. In Fig. 4.4 we show the satellite fraction as a function of stellar mass (dashed curve). The maximum fraction of satellite galaxies is $\sim 40\%$ for the smallest galaxies considered here. 30% of the Milky-Way-like galaxies are satellites and only 10% of the galaxies with stellar mass $10^{11.5}M_{\odot}$ are satellites, again this is consistent with the study by Mandelbaum et al. (2006). Both the simulations and the lensing estimates are carried out within the context of a Λ CDM cosmology. The good agreement in the halo mass estimates is evidence that the Λ CDM cosmology is self-consistent.

For galaxies like the Milky Way, which have masses $\sim 6 \times 10^{10}M_{\odot}$, we predict the halo mass to be around $2.6 \times 10^{12}M_{\odot}$. In the literature, the halo mass of the Milky Way has usually been estimated from the escape velocity or the velocity dispersion profile of the tracer populations. These are halo stars, globular clusters, or the surrounding satellite galaxies. Recent studies have suggested that the Milky Way halo mass is in the range $1 - 2 \times 10^{12}M_{\odot}$. Estimates, in units of $10^{12}M_{\odot}$, include $1.9^{+3.6}_{-1.7}$ (Wilkinson & Evans 1999), $2.5^{+0.5}_{-1.0}$ or $1.8^{+0.4}_{-0.7}$ (Sakamoto et al. 2003), depending on the inclusion or not of Leo I., $1.42^{+1.14}_{-0.54}$ (Smith & et al. 2007), $0.5 - 1.5$ (Battaglia et al. 2005; Dehnen et al. 2006), and $1.0^{+0.3}_{-0.2}$ (Xue et al. 2008). However, recent work by Li & White (2008) suggest a virial mass for the Milky Way of $2.43^{+0.8}_{-0.8} \times 10^{12}M_{\odot}$ from the Timing Argument. This implicitly includes all the mass in the system, and is quite close to our estimates here.

4.3.3 Galaxy Formation Efficiency

Using the relation between halo mass and stellar mass, we can derive a galaxy formation efficiency, taken to be the fraction of baryons locked in stars, as a function of the dark matter halo mass. Here we assume a universal baryon fraction $\frac{\Omega_b}{\Omega_m}$ in all the dark matter halos. The baryonic mass associated with a dark matter halo is

$$M_b = M_h \times \frac{\Omega_b}{\Omega_m} = M_h \times 17\% \quad (4.3)$$

We show the galaxy formation efficiency as a function of dark matter halo mass in Fig. 4.5. This efficiency peaks in halos with masses $\sim 6 \times 10^{11}M_{\odot}$, slightly less massive than typical Milky Way-like halos. The maximum value is around 20%. These efficiencies impose strong constraints on galaxy formation simulations. In most recent simulations of the formation of spiral galaxies similar to the Milky Way (Scannapieco et al. 2009; Governato et al. 2008; Okamoto et al. 2005), 30% – 60% of the baryons are typically converted into stars. The efficiency in Abadi et al. (2003) is even higher due to the lack of SN feedback in these simulations. Despite their success in reproducing many observed properties of real galaxies, these simulations all appear to have locked too many baryons in stars to be viable models for typical real galaxies.

The galaxy formation efficiency drops very fast towards both higher and lower masses. In galaxy groups of mass $10^{13}M_{\odot}$, only 5% of the total baryons can cool down and form stars in the central objects. A important candidate for this suppression of cooling is AGN feedback. In halos less massive than $4 \times 10^{10}M_{\odot}$, less than 1% of the baryons have been converted

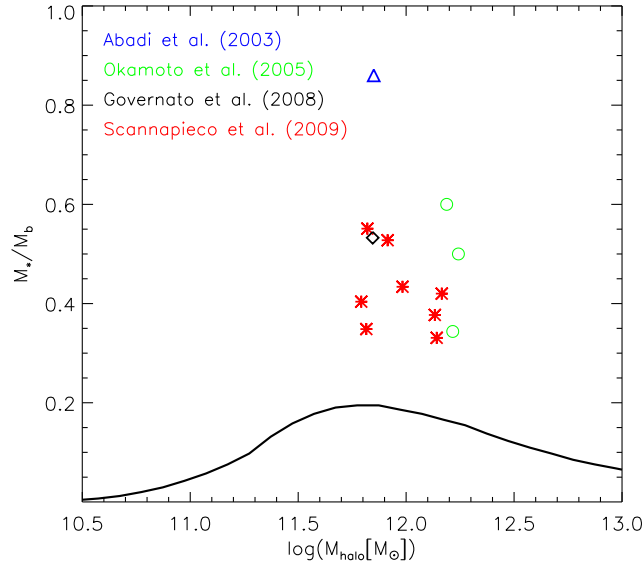


Figure 4.5: Galaxy formation efficiency as a function of halo mass. The black curve indicates the typical values required in a Λ CDM universe. The symbols of different colours are taken from different simulations of the formation of spiral galaxies. They show that most of these simulations have locked too many baryons into stars to be viable models for the bulk of the spiral population.

into stars. Here, SN feedback is believed to be responsible for the low efficiency since it is able to expel gas from the relatively shallow potential wells. In small systems, reionization may also play a role in suppressing star formation (Efstathiou 1992; Benson et al. 2002; Sawala et al. 2009).

4.3.4 Tully-Fisher Relation

A long standing problem in Λ CDM cosmology has been to reproduce the galaxy luminosity function, while at the same time matching the zero point of the Tully-Fisher relation (Kauffmann et al. 1993b; Cole et al. 1994; Navarro & Steinmetz 2000). The abundance matching method used here matches the stellar mass function automatically. To establish the link between galaxy stellar mass and circular velocity, we use the stellar mass vs. halo mass relation to find the stellar mass at the centre of each dark matter halo. The maximum circular velocity of each dark halo is tabulated directly in the simulations. The resulting “Tully-Fisher” relation is shown in Fig. 4.6. Black dots are our predictions for central galaxies. This assumes the galaxy rotation velocity to be equal to the maximum circular in the dark halo. There is a tight relation between stellar mass and halo maximum circular velocity. This relation can be described approximately by a double power law. The bend corresponds to the turn-over point in the stellar mass vs. halo mass relation (Fig. 4.2), and corresponds to the point where galaxy formation efficiency reaches its maximum. Large symbols are from the observable data for spiral galaxies (Bell & de Jong 2001). Crosses are for I band data, filled circles for K band data, and open circles for B and R band

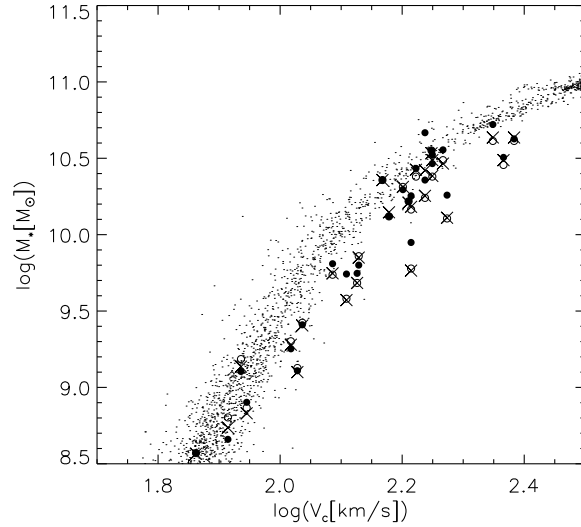


Figure 4.6: Stellar mass “Tully-Fisher” Relation. Small black dots represent our prediction for the stellar mass of central galaxies as a function of the maximum circular velocity of their halos. Big symbols are observational estimates using I band data (crosses), K band data (filled circles), and B and R data (open circles)(Bell & de Jong 2001).

data. Bell & de Jong (2001) adopted a scaled-down Salpeter Initial Mass Function (IMF) to derive the stellar mass, which is higher by 0.15 dex than Li & White (2009) who adopted a Chabrier IMF. We shift the observational data downwards by 0.15 dex in order to compare our prediction to their observational results directly. The Λ CDM model cannot be ruled out because the predicted circular velocities are similar to or lower than observed, as expected since the simulations do not take into account the gravity of the baryons. In the region $2.0 < \log V_c < 2.2$ where spiral galaxies dominate the mass functions, the predicted circular velocity at each stellar mass is lower than in the observations by about 25%. This is a plausible amount, given results from detailed simulations of spiral formations (e.g. Gustafsson et al. 2006; Abadi et al. 2009). At higher masses $\log V_c > 2.2$, the difference between prediction and observation is smaller, though the model still predicts a slightly lower circular velocity for a given stellar mass. At the low mass end $\log V_c < 2.0$, where dark matter dominates the gravity throughout the galaxies, the model prediction matches observations rather well.

4.4 Conclusions and Discussion

We have derived a parameter-free relation between the stellar mass of galaxies and their halo masses by assuming a one-to-one monotonic relation between the stellar mass of a galaxy and the maximum mass attained by its dark matter halo. The combination of MS-I and MS-II makes it possible to study halos over a wide mass range from $10^8 M_\odot$ up to $10^{15} M_\odot$. For the first time we are able to link stellar mass to the halo mass over this

full stellar mass range without assumptions about either the detailed galaxy formation processes or the evolution of subhalos.

We find that the mass-to-light ratio reaches its minimum in galaxies somewhat fainter than L^* , and increases rapidly both at higher and lower mass. Our derived halo masses are consistent with previous weak lensing estimates, confirming the self-consistency of the Λ CDM model. We find that the halo mass of typical Milky-Way-like galaxies is higher than many recent estimates from observations of halo tracers, but consistent with Timing Argument results.

Galaxy formation efficiency peaks at $\sim 20\%$ in halos slightly less massive than the hosts of $\sim L^*$ galaxies, and drops rapidly at both higher and lower masses. These values are consistent with previous work from weak lensing and abundance matching. Using weak lensing, Mandelbaum et al. (2006) found the maximum efficiencies to be 25% and 35% for late-type and early-type galaxies, respectively. Baldry et al. (2008) derived a peak efficiency of $\sim 25\%$, using a similar method to our own. The stellar mass function in Baldry et al. (2008) is consistent with that of Li & White (2009), which we adopt for this work. The difference in the estimates of peak galaxy formation efficiency can be attributed mainly to different halo mass functions. Baldry et al. (2008) use the main halo mass function plus the subhalo mass function. The latter was derived under certain assumptions about mass loss rates (Vale & Ostriker 2004). In addition, Baldry et al. (2008) dropped all the group/cluster halos (Shankar et al. 2006), while in our model, the cluster halos host the most massive galaxies. It is thus not surprising that, for a given stellar mass, the derived halo mass is smaller in Baldry et al. (2008) and the galaxy formation efficiency is then higher. Comparison with recent hydrodynamic simulations of spiral galaxy formation shows that the conversion efficiencies are too high in the simulations for them to be viable models for typical real galaxies.

We have predicted the stellar mass “Tully-Fisher” relation for central galaxies over the rotation velocity range $1.8 < \log(V_c [km/s]) < 2.5$. For galaxies like the Milky Way, our model prediction of circular velocity is lower than observed. However, the prediction could be increased by taking baryonic effects into account. At lower masses where dark matter dominates gravity throughout galaxies, our results match the observations fairly well. Thus, Λ CDM models do seem able to reproduce observed luminosity functions and Tully-Fisher relations simultaneously.

Although this method is a powerful way to relate galaxies to their dark matter halos, in reality, there must be some scatter in the relation which should be kept in mind. One of the most important sources of scatter comes from the evolution of the stellar mass vs. halo mass relation. The gas fraction is higher at high redshift than in the local universe. More baryons are in the form of gas rather than stars in the early stage of galaxy formation. Fig. 4.4 shows that the satellite fraction is higher for smaller stellar mass, suggesting there may be more scatter in low mass galaxies than at high mass. Another source of scatter comes from variations in halo assembly history (Gao & White 2007). For example, the star formation efficiency is higher in merger induced bursts than in quiescent phases. We can study this effect by comparing galaxy correlation functions, and their dependence on stellar mass and age with observation. Direct measurement of the stellar mass function at high redshift will also help us study the scatter in a more quantitative way.

Galaxy Formation in a Hierarchical Universe: What affects the formation of dwarf galaxies?

Abstract

We study dwarf galaxy formation and the effect of environment on galaxy evolution in clusters in the concordance Λ CDM cosmology. We implement updated semi-analytic models on both the Millennium Simulation (MS-I) and the Millennium II Simulation (MS-II) simultaneously, thus allowing a study of the effects of numerical resolution on such galaxy formation simulations. For the first time we are able to follow the formation and evolution of galaxies as faint as the faintest dwarf spheroidals around the Milky Way at the same time as cD galaxies in clusters. To reproduce the observed stellar mass function, we introduce a new supernova feedback model, in which the energy used to reheat the interstellar medium and to blow gas out of a halo is a decreasing function of the circular velocity of the host dark matter halo. We further assume the time-scale to reincorporate gas from the surroundings to decrease with the circular velocity of the dark matter halo. We explore environmental effects on galaxy evolution in groups and clusters by taking into account ram pressure and tidal stripping, disruption, and merging of satellite galaxies. The model parameters are adjusted to fit the local SDSS galaxy stellar mass function of Li & White (2009). We are able to reproduce this function accurately, from $10^{12}M_{\odot}$ down to 10^8M_{\odot} . The predicted stellar mass correlation function matches observations on large scales, but it is higher on small scales, almost a factor of 2 at $r \sim 10\text{kpc}$. The observed correlation functions of mass-limited samples of blue and red galaxies are qualitatively reproduced by our model. Their amplitude is, however, higher than observed for all mass ranges, suggesting that a lower value for the fluctuation amplitude than the $\sigma_8 = 0.9$ adopted in the MS-I and MS-II is needed. It is interesting that our model reproduces the luminosity function of satellite galaxies around the Milky Way automatically. Reionization has a significant effect only on the abundance of very low-mass galaxies, such as the very faint satellites of the Milky Way. In rich galaxy clusters of mass $\sim 10^{14}M_{\odot}$, our model predicts around 10% of stars to be in the intracluster medium; this fraction increase slightly with cluster mass. This is broadly consistent with observation.

5.1 Introduction

The Λ CDM model has been successful in interpreting a wide variety of observations, which include the cosmic microwave background fluctuations at $z \sim 1000$ (e.g. Spergel et al. 2003), the galaxy power spectrum in the local universe (Percival & et al. 2002; Tegmark & et al. 2004) large-scale galaxy clustering (Eisenstein & et al. 2005), the cosmic shear field measured by weak gravitational lensing (Van Waerbeke et al. 2002; Bacon et al. 2005; Heymans & et al. 2005; Hoekstra et al. 2006), the high-redshift power spectrum probed by the Lyman α forest (Mandelbaum et al. 2003; Desjacques & Nusser 2005; Jena et al. 2005), and the abundance of galaxy clusters (Borgani et al. 2001) as well as their baryon fractions (White et al. 1993; Allen et al. 2004). Nowadays, N-body simulations are able to follow the formation and evolution of dark matter halos from rich galaxy-cluster scales down to dwarf galaxy hosts in a cosmological context. As mentioned in Chapter 1 and Chapter 2, however, the formation and evolution of galaxies do not always trace those of dark matter halos. Theoretical predictions cannot be used to compare with observations without taking into account more complex baryonic processes.

In the standard scenario of galaxy formation, as originally proposed by White & Rees (1978), gas condenses at the center of hierarchically merging dark matter halos. The mass function of dark matter halos, which grow hierarchically by the merging of smaller systems which formed earlier is, however, a poor match in shape to galaxy luminosity functions (see also Chapter 1 and Chapter 4). Fewer stars have been observed in halos with higher and lower masses with respect to the Milky Way host halo than predicted, based on a constant mass-to-light ratio. One explanation of the low star formation efficiency in massive halos is that a supermassive black hole at the center releases vast amounts of energy when it absorbs mass from its surroundings, and this suppresses cooling and star formation in its host galaxy (AGN feedback) (Croton et al. 2006; Bower et al. 2006). The abundance of low mass halos could be reduced by replacing cold dark matter with warm dark matter (Bode et al. 2001), but the adoption of warm dark matter is challenged by the requirement to form relatively massive structures at high redshift, within which galaxies could form to produce high energy photons to account for the reionization of the intergalactic medium (Spergel et al. 2003). White & Rees (1978) argued that in the hierarchical paradigm, feedback can help expel gas from small galaxies, making them less successful at forming stars, thus reducing the stellar masses of faint galaxies. Cosmic reionization, which could inhibit gas collapsing into shallow potential well and suppress gas cooling in low mass halos, could also affect galaxy formation in very small halos (see Chapter 1).

A relevant issue is the *missing satellite* problem. There is no preferred scale in the Λ CDM paradigm. Substructures similar to a scaled-down version of that in cluster-mass dark matter halos is expected to occur in galactic-size dark matter halos. In fact, this has been already revealed in high-resolution dark matter simulations (Klypin et al. 1999; Moore et al. 1999; Diemand et al. 2007; Springel et al. 2008; Boylan-Kolchin et al. 2009). The number of satellite galaxies detected to date around the Milky Way appears less than expected from simple predictions based on the mass and number of dark matter substructures. One explanation is that the star formation efficiency is very low so that many dark matter substructures host very faint galaxies or no galaxy at all and so are missed by current surveys. This is closely related to the problem of dwarf galaxy formation

as discussed above. Environmental effects might also play a role in this 'missing satellite' problem: after a galaxy falls into a larger system, the gas and stars are stripped from the satellite, leading to a rapid decline in star formation and a transformation in galaxy color. The stripped materials are distributed in the intracluster medium, contributing to the hot gas reservoir of the central galaxy and the intracluster light.

In recent years, the Sloan Digital Sky Survey (SDSS) has been able to make a robust determination of the low mass end of galaxy stellar mass function, down to stellar mass of $10^7 M_\odot$ or $10^8 M_\odot$. Li & White (2009) provide the galaxy stellar mass function from $\sim 10^{12} M_\odot$ all the way down to $10^8 M_\odot$ based on SDSS DR7 and so with excellent statistics. In the Local Group, the number of known dwarf spheroidals has doubled in the past few years as a result of analysis of SDSS (Willman et al. 2005; Zucker & et al. 2006; Belokurov & et al. 2007; Irwin & et al. 2007; Gilmore et al. 2007). Most recently, the SDSS has made it possible to probe satellite galaxies as faint as $100 L_\odot$ (Koposov et al. 2008). It is now timely to revisit the issue of dwarf galaxy formation, both in the field and in galaxy groups/clusters. Here we use two very large N-body simulations, MS-I and MS-II. The combination of the two simulations enables one to study the formation of dark matter halos with good mass resolution and excellent statistics from several times $10^8 M_\odot$ to $10^{15} M_\odot$, providing a framework within which we can study the formation and evolution of all galaxy populations observed so far. The sub-grid physics, in terms of star formation, feedback etc, is grafted onto the two N-body simulations using simplified recipes. We revisit and improve the galaxy formation model, in particular with respect to supernova feedback and the reincorporation of expelled gas, which is most relevant for low-mass galaxy formation. The modelling of environmental effects is also improved by introducing a more sophisticated treatment of stripping and of the disruption of satellite galaxies.

This chapter is organized as follows. In Sec. 5.2 we briefly describe the two N-body simulations on which we implemented the galaxy formation models. A detailed description of the semi-analytic models is presented in Sec. 5.3. In Sec. 5.4 we study the galaxy stellar mass and luminosity functions, and the luminosity function of satellite galaxies in the Milky-Way-like systems. Model predictions for the stellar mass function of galaxies in clusters and for the fraction of intracluster light as a function of the cluster mass are also presented in this section. Conclusions and discussion are presented in Sec. 5.5.

5.2 N-body Simulations

We build up galaxy catalogues by implementing galaxy formation models on two large cosmological N-body simulation the *Millennium Simulation* (Springel et al. 2005b) and the *Millennium Simulation II* (Boylan-Kolchin et al. 2009). These simulations assume a concordance Λ CDM cosmology consistent with a combined analysis of the 2dFGRS (Colless & et al. 2001) and the first-year WMAP data (Spergel et al. 2003). The cosmological parameters are $\Omega_m = 0.25$, $\Omega_b = 0.045$, $h = 0.73$, $\Omega_\Lambda = 0.75$, $n = 1$, and $\sigma_8 = 0.9$, where the Hubble constant is parameterized as $H_0 = 100 h \text{ km s}^{-1} \text{ Mpc}^{-1}$. Both simulations trace 2160^3 particles from redshift 127 to the present day. MS-I was carried out in a periodic box of $500 h^{-1} \text{ Mpc}$ on a side, and MS-II in a box of $100 h^{-1} \text{ Mpc}$ on a side. The corresponding particle masses are $8.6 \times 10^8 h^{-1} M_\odot$ and $6.9 \times 10^6 h^{-1} M_\odot$, respectively. The

minimum halo contains 20 bound particles so that MS-II is just sufficient to study the faintest galaxies observed so far. At the same time, the large volume of MS-I makes it possible to study rare objects like rich clusters. A comparison of the two simulations where both have good statistics allows us to study how the limited resolution of MS-I affect its model galaxy populations.

The particle data were stored at 64 and 68 output times in MS-I and MS-II, respectively. At each time, the code produce a friends-of-friends (FOF) catalogue by linking particles with separation less than 0.2 of the mean value (Davis et al. 1985). In each FOF group, the SUBFIND algorithm (Springel et al. 2001) is applied to identify substructures (subhalos). The largest self-bound subhalo in the FOF group is referred to as its main subhalo (sometimes the main halo) and usually contains most of its mass. Each FOF group hosts a “central galaxy”, which resides at the center of the potential of the main subhalo. The rest of the galaxies are called satellite galaxies.

The virial radius is defined as the distance from the FOF group center within which the mean overdensity is 200 times the critical value. The group center is defined as the minimum of the gravitational potential well of the group. The virial radius and the virial mass are related by

$$R_{vir} = \left(\frac{G}{100} \frac{M_{vir}}{H^2(z)} \right)^{1/3}. \quad (5.1)$$

The virial radius is usually within the boundary of the FOF group (R_{FOF}). In our galaxy formation model (Sec. 5.3), satellite galaxies within R_{vir} of the main halo are treated differently from those between R_{vir} and R_{FOF} . This helps to avoid artificial effects when two distinct structures are joined by a tenuous bridge of particles.

We refer readers to Springel et al. (2005b) and Boylan-Kolchin et al. (2009) for full descriptions of these two simulations.

5.3 Galaxy Formation Models

Galaxies form in the centers of dark matter halos and gain stars by formation from their interstellar medium (ISM) and by accretion of satellite galaxies. The dense ISM is assumed to form a disk and may be replenished by infall from the surrounding halo, and by gas from accreted satellite galaxies. The interaction between these processes and the feedback driven by supernovae and by active galactic nuclei drives the overall evolution of galaxies, which thus cannot be followed realistically without considering a complex network of baryonic physics. As discussed in Chapter 1, the physical understanding of most of these baryonic processes is incomplete and can only be described in an approximate way.

Here we use a semi-analytic technique to implement simplified galaxy formation recipes into dark matter merger trees extracted from the MS-I and the MS-II. This treatment of baryonic evolution through post-processing cosmological N-body simulations enables us to explore a wide model and parameter space in a relatively short time, when compared to simulations that follow the hydrodynamics of diffuse gas directly. In general, our models are similar to those in Croton et al. (2006) and De Lucia & Blaizot (2007) (hereafter DLB07). The main modifications here include mass-dependent supernova feedback, gradual stripping and disruption of satellite galaxies, a model that follows the angular momentum

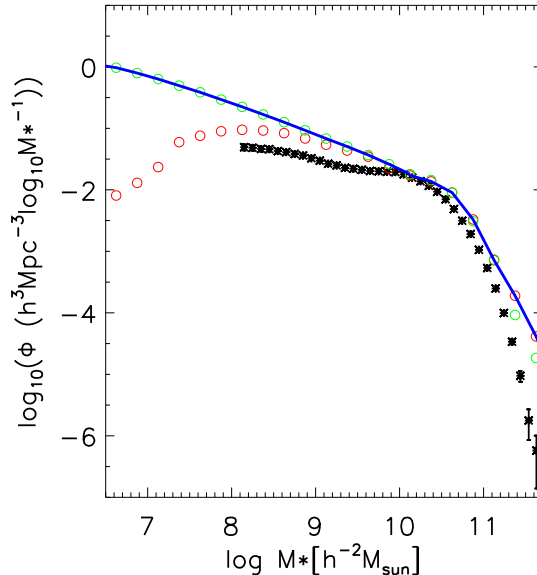


Figure 5.1: Stellar Mass functions. Green open circles are from the MS-II and red open circles are from the MS-I. The blue curve is the stellar mass function predicted by the DLB07. Black stars with error bars are for SDSS DR7 (Li & White 2009)

accumulation history of gas disks and stellar disks, and a model to calculate bulge sizes. We determine the free parameters of these models using the local observations. In the following we first discuss the discrepancy in abundance of low-mass galaxies between observations and the model predictions from DLB07, which is one motivation for this work. We then describe in detail our new galaxy formation models. The reader is referred to previous work for more general information about semi-analytic models (White & Frenk 1991; Kauffmann et al. 1993; Somerville & Primack 1999; Cole et al. 2000; Springel et al. 2001; Croton et al. 2006; DLB07).

5.3.1 Stellar Mass Function in DLB07

The galaxy formation model in DLB07 has been successful in reproducing many observational properties both in the local universe and at high redshift for galaxies with stellar mass exceeding $10^{9.5}M_{\odot}$. This limit corresponds to the mass resolution in the MS-I. However, when we apply this model to the MS-II, we find that it overpredicts the number density of low-mass galaxies by a significant factor. Part of the success of DLB07 was in fact due to the limited resolution of MS-I which suppressed star formation significantly in low-mass galaxies. Fig. 5.1 shows a comparison between the predictions of the DLB07 model and observational results. The green circles are for the MS-II and red for the MS-I. The combined stellar mass function is shown using the blue curve, and the black stars with error bars are from SDSS data release 7 (SDSS DR7) by Li & White (2009). At $M_* \sim 10^8 M_{\odot}$,

corresponding to halo masses of $5 \times 10^{10} M_{\odot}$ which are well resolved in MS-II, the model prediction is higher than observed by 0.6 dex. The predicted slope at the low mass end is 1.54, while Li & White (2009) give a value of 1.15. The overestimate of the abundance of low mass galaxies indicates that the DLB07 model has a star formation efficiency that is too high in low-mass halos.

The formation of low-mass galaxies is very sensitive to the star formation and supernova feedback recipes, as well as to environmental effects. We revisit all the relevant processes and describe our modified galaxy formation model below.

5.3.2 Reionization and Cooling

It is now well established that the global baryon to dark matter mass ratio is 15-20%. In galaxy clusters, the observed baryons fraction is close to but somewhat below this value, while in the halo of the Milky Way, at best one-quarter of the expected baryons have been detected (see Chapter 4). The detected baryon fraction is inferred to be even lower in the halos of dwarf galaxies. There are several mechanisms which may account for this “missing baryon” problem, one of which is photoheating by the UV background. This could prevent gas from collapsing into dark matter halos if the thermal energy dominates the gravitational potential energy. We follow Croton et al. (2006) and introduce a “filter halo mass” under which the baryon collapsing is affected by the UV background radiation. We adopt the fitting formula given by Gnedin (2000), which describes the baryon fraction as a function of halo mass:

$$f_b(z, M_{vir}) = \frac{f_b^{cosmic}}{[1 + 0.26M_F(z)/M_{vir}]^3}. \quad (5.2)$$

Here $f_b^{cosmic}=17\%$ is the universal baryon fraction, which is consistent with the first year WMAP estimates (Spergel et al. 2003). The filter mass M_F is a function of redshift, which depends on the re-ionization process in early universe. Kravtsov et al. (2004) parameterized the simulation results of Gnedin (2000) by distinguishing the reionization epoch into three phases: i) $z > z_0$, the universe is mainly neutral and isolated HII regions do not overlap; ii) $z_0 < z < z_r$, individual HII regions overlap; iii) $z > z_r$, the universe is completely ionized. We adopt their best fit parameters $z_0 = 8$ and $z_r = 7$ in this paper. This model gives a filtering mass of $3 \times 10^{10} M_{\odot}$ at $z=0$. However, recent work by Hoeft et al. (2006) and Okamoto et al. (2008) argue that the reionization effect has been overestimated. They find a characteristic mass $\sim 6.5 \times 10^9 M_{\odot}$ at $z=0$, which is significantly lower than the value given by Kravtsov et al. (2004). We will show later that reionization is not necessary to reproduce local galaxy properties in the presence of strong supernova (SN) feedback except for the faintest Milky Way satellite systems.

When a dark matter halo collapses, a fraction f_b of baryons collapses with it and shocks to a high temperature. At early times and in low-mass halos, the post-shock cooling time is very short and the gas condenses out on the a free-fall time scale; at late times and in massive halos, the cooling time can be relatively long and the gas shock heats to form a quasi-static hot atmosphere from which gas cools onto the center through a cooling flow. The critical mass separating these two modes is around $10^{12} M_{\odot}$ at $z=0$ (Rees & Ostriker 1977). This idea has been employed by many authors in their galaxy formation models (White & Frenk 1991; Kauffmann et al. 1993b, 1999; Cole et al. 1994, 2000;

Springel et al. 2001; Croton et al. 2006; De Lucia & Blaizot 2007; Somerville & Primack 1999b; Somerville et al. 2008).

Here we follow the procedure of Croton et al. (2006) to estimate the boundary between these cold flow and hot halo regimes. We assume that the collapsing gas is shock-heated to the virial temperature of the host halo and its distribution is described by an isothermal profile. The cooling time is calculated according to:

$$t_{cool}(r) = \frac{3\mu m_{\text{H}} k T_{\text{vir}}}{2\rho_{\text{hot}}(r)\Lambda(T_{\text{hot}}, Z_{\text{hot}})} \quad (5.3)$$

where μm_{H} is the mean particle mass, k is the Boltzmann constant, $\rho_{\text{hot}}(r)$ is the hot gas density at radius r , $\Lambda(T_{\text{hot}}, Z_{\text{hot}})$ is the temperature and metallicity dependent cooling function, and Z_{hot} is the metallicity of the hot halo gas. $T_{\text{hot}} = 35.9(V_{\text{vir}}/(km/s))^2$ is the virial temperature of the host halo. In the main halo, the gas temperature is updated according to the current circular velocity at the virial radius of the main halo at each snapshot, while in subhalos, we assume the gas temperature to be constant at the value at the time of accretion onto the main halo.

The cooling radius is determined through

$$r_{cool} = \left[\frac{t_{dyn, dm} m_{\text{hot}} \Lambda(T_{\text{hot}}, Z_{\text{hot}})}{6\mu m_{\text{H}} k T_{\text{vir}} R_{\text{vir}}} \right]^{\frac{1}{2}} \quad (5.4)$$

There are several possible choices for $t_{dyn, dm}$. Here we follow Croton et al. (2006) taking $t_{dyn, dm} \equiv R_{\text{vir}}/V_{\text{vir}} = 0.1H(z)^{-1}$. Readers are referred to Croton et al. (2006) and Somerville et al. (2008) for the discussion of other choices of the $t_{dyn, dm}$ used to define r_{cool} . When $r_{cool} < R_{\text{vir}}$ we assume we are in the static halo/cooling flow regime, and the cooling rate is:

$$\dot{M}_{cool} = \frac{1}{2} m_{\text{hot}} \frac{r_{cool}}{R_{\text{vir}}} \frac{1}{t_{cool}}. \quad (5.5)$$

When $r_{cool} > R_{\text{vir}}$, on the other hand, we assume that we are in the cold flow regime and gas condenses onto the central object in a halo dynamical time:

$$\dot{M}_{cool} = \frac{m_{\text{hot}}}{t_{dyn, dm}} \quad (5.6)$$

In our model the cooling rate is slower than DLB07, where they assume that the gas falls onto the central object instantaneously in the cold flow regime.

5.3.3 Star Formation

5.3.3.1 Disk Sizes

Disk size is very important for determining the density of gas in disks, which in turn determines the star formation rate. In many semi-analytical models, galaxy disks are assumed always to have the same spin parameter as their host halos. Here we introduce a new and more realistic disk model which distinguishes between gas and stellar disks and traces their angular momentum accumulation histories separately.

The total angular momentum vector of the gas disk at the end of a timestep can be expressed as

$$\mathbf{J}_{gas} = \mathbf{J}_{init,gas} + \delta\mathbf{J}_{gas,cooling} + \delta\mathbf{J}_{gas,acc} - \delta\mathbf{J}_{gas,SF} \quad (5.7)$$

where $\mathbf{J}_{init,gas}$ is the angular momentum of the gas disk at the beginning of the step, and $\delta\mathbf{J}_{gas,cooling}$, $\delta\mathbf{J}_{gas,acc}$ and $\delta\mathbf{J}_{SF}$ are the angular momentum changes due to addition of gas by cooling and by accretion from minor mergers, and to removal of gas by star formation, respectively.

When hot gas cools onto the central object we assume it carries a specific angular momentum which matches the current value for the dark matter halo \mathbf{J}_{DM}/M_{DM} . The angular momentum change due to gas cooling can thus be expressed as

$$\delta\mathbf{J}_{gas,cooling} = \dot{M}_{cool} \frac{\mathbf{J}_{DM}}{M_{DM}} \delta t \quad (5.8)$$

where \dot{M}_{cool} is the cooling rate, and δt is the corresponding time interval. When a merger happens between two galaxies with mass ratio larger than 3 (a minor merger), we assume that the cold gas in the minor progenitor is added to the disk of the main progenitor (see sec. 5.3.6), carrying a specific angular momentum equal to the current value for the dark matter halo. The corresponding angular momentum change in gas disk is thus

$$\delta\mathbf{J}_{gas,acc} = M_{sat,gas} \frac{\mathbf{J}_{DM}}{M_{DM}} \quad (5.9)$$

where $M_{sat,gas}$ is the cold gas mass in the satellite disk. When an amount of cold gas is converted into stars we assume it carries the average specific angular momentum of the gas disk, \mathbf{J}_{gas}/M_{gas} , and the change in angular momentum is

$$\delta\mathbf{J}_{gas,SF} = \dot{M}_* \frac{\mathbf{J}_{gas}}{M_{gas}} \delta t = -\delta\mathbf{J}_{*,SF} \quad (5.10)$$

where $\delta\mathbf{J}_{*,SF}$ is the change of angular momentum of the stellar disk, and \dot{M}_* is the star formation rate.

For the stellar disk, the angular momentum at the end of the timestep is a vector sum

$$\mathbf{J}_* = \mathbf{J}_{init,*} + \delta\mathbf{J}_{*,SF} \quad (5.11)$$

where $\mathbf{J}_{init,*}$ is the angular momentum of the stellar disk at the beginning of the step, and $\mathbf{J}_{*,SF}$ is the angular momentum gained during star formation. In this simple model, the total angular momentum of the stellar disk only changes due to the star formation.

We assume both the gas disk and the stellar disk to be thin, to be in centrifugal equilibrium and to have exponential density profiles

$$\Sigma(R_{gas}) = \Sigma_{gas0} \exp(-R_{gas}/R_{gas,d}), \quad (5.12)$$

$$\Sigma(R_*) = \Sigma_{*0} \exp(-R_*/R_{*,d}), \quad (5.13)$$

where $R_{gas,d}$ and $R_{*,d}$ are the scale-lengths of the gas disk and the stellar disk, and Σ_{gas0} and Σ_{*0} are the corresponding central surface densities. Assuming a flat circular velocity

curve, which holds for a galaxy with negligible self-gravity in an isothermal dark matter halo, the scale-lengths can be calculated as

$$R_{gas,d} = \frac{J_{gas}/M_{gas}}{2V_{cir}}, \quad (5.14)$$

$$R_{*,d} = \frac{J_*/M_{*,D}}{2V_{cir}} \quad (5.15)$$

where M_{gas} and $M_{*,D}$ are the total mass of the gas disk and the stellar disk, and V_{cir} is the circular velocity. Here we adopt the maximum velocity of the surrounding dark matter halo, V_{max} , as V_{cir} . Note for a satellite galaxy, we keep its circular velocity fixed after the infall. This is because the core of the dark matter subhalo, which determines the circular velocity of the gas disk, is usually compact and does not change by much until the subhalo is about to be destroyed.

5.3.3.2 Star Formation Law

Kennicutt (1998) found the star formation only takes place in regions where the density is above some critical value. Toomre (1964) derived a surface mass density threshold as a function of velocity dispersion, surface density and velocity gradient, above which the gas in a rotationally supported disk is unstable and starts to collapse to form stars. Here we adopt a simplified version of this threshold surface density as a function of radius, assuming a gas velocity dispersion of 6 km/s, as in Kauffmann (1996) and Croton et al. (2006),

$$\Sigma_{crit}(R) = 12 \left(\frac{V_{max}}{200 \text{ km s}^{-1}} \right) \left(\frac{R}{10 \text{ kpc}} \right)^{-1} M_{\odot} \text{ pc}^{-2}. \quad (5.16)$$

This corresponds to a critical mass within three exponential scale radii (i.e. $R < 3R_{gas,d}$)

$$M_{crit} = 7.6 \times 10^9 \left(\frac{V_{max}}{200 \text{ km/s}} \right) \left(\frac{R}{10 \text{ kpc}} \right) M_{\odot}. \quad (5.17)$$

We reduce this threshold mass by a further factor of 2 to account for additional sources of instability and to agree with Croton et al. (2006) who assume constant cold gas surface density in the disk. The result is consistent with the study of H₂ formation in galaxies of solar metallicity (Krumholz et al. 2008).

The amount of gas that can be converted into stars in a unit time is assumed to be

$$\dot{M}_* = \alpha (M_{gas} - M_{crit}) / t_{dyn} \quad (5.18)$$

where we set $\alpha = 0.02$. This means that gas consumption would take several Hubble times if no feedback were present.

5.3.4 Supernova Feedback

At the end stage of evolution of a massive star, an enormous amount of energy is released during a supernova (SN) explosion. The radiation and the blast-waves from supernovae may heat the interstellar medium and blow them out of the host galaxy. This effect is

of particular importance in the formation of low-mass galaxies where the potential well is shallower. White & Rees (1978) first proposed that supernova feedback can help to reproduce the proper abundance of dwarf galaxies. This has been further investigated by many authors (e.g. Cole et al. 2000).

We calculate the amount of gas which is reheated by SN as

$$\delta M_{reheat} = \epsilon_{disk} \times \delta M_* \quad (5.19)$$

$$\epsilon_{disk} = \epsilon \times \left(0.5 + \left(\frac{V_{max}}{70 \text{ km/s}}\right)^{-\beta_1}\right) \quad (5.20)$$

where δM_* is the mass of stars formed during a certain time interval, and ϵ and β_1 are free parameters which describe the amplitude of the reheating efficiency and its dependence on V_{max} , respectively. Here we set $\epsilon = 3.5$ and $\beta_1 = 5.5$. Although the dependence on the V_{max} is very strong in this default model, the results are not very sensitive to this choice because of saturation effects at low velocity (see below). $\beta_1 = 3$ gives very similar results for the galaxy stellar mass function and the gas metallicity vs. stellar mass relation.

The total amount of energy released to reheat and eject gas is parameterized as:

$$\delta E_{SN} = \epsilon_{halo} \times \frac{1}{2} \delta M_* V_{SN}^2 \quad (5.21)$$

$$\epsilon_{halo} = \eta \times \left(0.5 + \left(\frac{V_{max}}{70 \text{ km/s}}\right)^{-\beta_2}\right) \quad (5.22)$$

where $0.5V_{SN}^2$ gives the mean energy in the supernova ejecta per unit mass of stars formed. As in Croton et al. (2006), we take $V_{SN}=630 \text{ km s}^{-1}$. Here η is a free parameter, and β_2 describes the dependence on V_{max} . In our preferred model, $\eta = 0.35$ and $\beta_2 = 5.5$. Again, the results are not very sensitive to the choice of β_2 because we do not allow ϵ_{halo} to exceed unity. The total amount of gas which can be ejected from the dark matter halo is thus:

$$\delta M_{ejec} = \frac{\delta E_{SN} - \frac{1}{2} \delta M_{reheat} V_{vir}^2}{\frac{1}{2} V_{vir}^2} \quad (5.23)$$

If $\delta M_{ejec} < 0$, we assume that the mass of reheated gas saturates at $\delta M_{reheat} = \delta E_{SN} / (\frac{1}{2} V_{vir}^2)$ and no gas could be ejected out of the dark matter subhalo. Compared to DLB07, our model of SN feedback is more effective in low circular velocity halos. The reheating efficiency and ejection efficiency, $\frac{\delta M_{reheat}}{\delta M_*}$ and $\frac{\delta E_{SN}}{0.5 \delta M V_{SN}^2}$, decline with the halo circular velocity and saturate at 0.5ϵ and 0.5η , respectively.

If gas is ejected from the main subhalo, it will contribute to the mass M_{ejec} in the ejecta “reservoir” of the main subhalo, from which it might be reincorporated into the cooling cycle as the halo grows. If gas is ejected from a subhalo, on the other hand, it will contribute to the hot atmosphere of the main subhalo, and will never fall back into the subhalo. In low-mass halos, the hot gas is much more weakly bound than in massive halos and gas is thus easier to eject to give high kinematic energy relative to the binding energy. We model virial velocity dependent reincorporation as

$$\dot{M}_{ejec} = -\gamma \left(\frac{V_{vir}}{220 \text{ km/s}}\right) \left(\frac{M_{ejec}}{t_{dy}}\right) \quad (5.24)$$

where γ is a free parameter which we set to be 0.4. In halos similar to the Milky-Way host halo, the ejected gas will return to the hot halo in a few dynamical times.

5.3.5 Satellite Galaxies in Groups and Clusters

In this section, we treat satellite galaxies within and beyond R_{vir} of the main halo separately. The satellite galaxy in the center of a subhalo beyond R_{vir} is treated in the same manner as the central galaxy of a main halo, while satellite galaxies in subhalos within R_{vir} lose their gas due to environmental effects.

5.3.5.1 Gas Stripping

In most semi-analytic models, hot gas associated with a halo is assumed to be stripped immediately after accretion on to a larger system, leading to a rapid decline in star formation and a reddening in color. In the real Universe (Sun et al. 2007; Jeltema et al. 2008) and in hydrodynamic simulations, however, the hot atmosphere of massive satellite galaxies may survive for a considerable while after accretion. McCarthy et al. (2008) found that for satellite galaxies with typical structural and orbital parameters, around 30% of the initial hot galactic halo gas can remain in place for more than 10 Gyr. In the following we introduce a model for the ram pressure and tidal effects in galaxy clusters, which gradually strip the hot atmospheres from satellite galaxies.

As for the main halo, we assume the hot gas relaxes to a distribution that exactly parallels that of its host dark matter subhalo. The specific tidal force on the hot atmosphere is then the same as on the dark matter in its subhalo. We calculate the remaining hot gas mass after tidal stripping assuming it is reduced in exactly the same way as the dark matter mass which is followed explicitly in the original simulations, i.e.

$$\frac{M_{hot}(R_{tidal})}{M_{hot,infall}} = \frac{M_{DM}}{M_{DM,infall}} \quad (5.25)$$

where $M_{DM,infall}$ and $M_{hot,infall}$ are the masses of the subhalo and of the associated hot gas just before accretion, and M_{DM} and $M_{hot}(r)$ are the current mass of the subhalo and the hot gas, respectively. Recall that we assume an isothermal profile for the hot gas distribution, thus $M_{hot}(r) = r/R_{tidal} \times M_{hot}(R_{tidal})$. The tidal radius beyond which the hot gas is stripped can be expressed as

$$R_{tidal} = \left(\frac{M_{DM}}{M_{DM,infall}}\right)R_{DM,infall} \quad (5.26)$$

where $R_{DM,infall}$ is the virial radius of the subhalo just before accretion.

In addition to the tidal force, the hot gas of satellite galaxies also feels pressure from the intracluster medium (ICM) due to their relative movement (ram pressure). At a certain radius, $R_{r.p.}$, the self-gravity is balanced by this ram pressure:

$$\rho_{sat}(R_{r.p.})V_{sat}^2 = \rho_{par}(R)V_{orbit}^2 \quad (5.27)$$

where $\rho_{sat}(R_{r.p.})$ is the hot gas density of the satellite at the radius $R_{r.p.}$, V_{sat} is the virial velocity of the subhalo at infall (which we assume to be constant as the subhalo orbits

around the main halo), $\rho_{par}(R)$ is the hot gas density of the parent dark matter halo at distance R from the center of its potential well, and V_{orbit} is the orbital velocity of satellite, which we assume to be the virial velocity of the main halo. The pressure from surroundings wins over the gravity beyond $R_{r.p.}$ and the hot gas at these radii is stripped.

We compare the two radii R_{tidal} and $R_{r.p.}$ and define the minimum of the two as the stripping radius

$$R_{strip} = \min(R_{tidal}, R_{r.p.}) \quad (5.28)$$

Beyond R_{strip} we assume all the hot gas is stripped away. The relative importance of these two mechanisms in stripping hot gas will be discussed elsewhere.

Besides the stripping, there are at least two other processes that may change the hot gas reservoir of satellites. One is cooling. The hot gas in satellite galaxies can cool and replenish the central cold star-forming disk. Here we assume that the temperature of hot gas within R_{strip} does not change after infall. The cooling rate is calculated in the same way as in sec. 5.3.2, which ensures continuity in the treatment of cooling as central galaxies turn into satellite galaxies. Another process which changes the hot atmosphere around the satellite galaxies is SN feedback. As happened in central galaxies, stars formed in satellite galaxies evolve into supernovae, releasing a huge amount of energy and reheating the cold gas in the disk. Font et al. (2008) found that satellite galaxy properties are very sensitive to the way in which the reheated gas is distributed between components: if the reheated gas is stripped to the same degree as the hot gas at infall, satellite galaxies will lose their gas and become red very rapidly. In fact, in their work, they adopted a stripping efficiency for the reheated gas which is only $\sim 10\%$ that for the hot gas. In contrast, we treat the reheated gas in satellite galaxies in the same way as in the central galaxies. We assume the reheated gas extends to a radius equal to the virial radius of the subhalo at infall. Taking into account the stripping mechanism discussed above, only reheated gas within R_{strip} remains in the subhalo and the rest is added to the hot atmosphere of the main halo.

5.3.5.2 Disruption

The stellar component in subhalos can also be stripped in the presence of very strong tidal forces. Usually, the galaxy is harder to disrupt than the dark matter halo because it is more compact. We thus assume the stellar component of a satellite galaxy will only be affected by the tidal force after its host subhalo is entirely disrupted. The position of the satellite galaxy is then assigned to the most bound particle of its subhalo at the last time when this could be identified. To estimate when stripping of stars is important we assume the satellite orbits in an isothermal potential field:

$$\phi(R) = V_{vir}^2 \ln R \quad (5.29)$$

Assuming conservation of the orbital energy and angular momentum, the distance of the pericenter from the potential center can be estimated from:

$$\left(\frac{R}{R_{peri}}\right)^2 = \frac{\ln \frac{R}{R_{peri}} + \frac{1}{2}V_{vir}}{\frac{1}{2}V_{vir,t}} \quad (5.30)$$

where R is the current distant of the satellite galaxy from the center and $V_{vir,t}$ is the tangential part of the orbital velocity of the satellite galaxy.

We compare the main halo density at pericenter with the average stellar mass density of satellite within its half light radius. If

$$\frac{M_{DM}(R_{peri})}{R_{peri}^3} \equiv \rho_{DM} > \rho_{sat} \equiv \frac{M_{sat,stellar}}{R_{sat,half}^3}, \quad (5.31)$$

we assume the satellite galaxy is disrupted entirely and its stars are assigned to a population of intracluster stars (ICS). In this calculation we do not fully take into account dynamical friction effects on the satellite orbit, which are underestimated by the simulation once the remaining mass of a subhalo drops below the stellar mass of its associated galaxy.

5.3.6 Mergers

Mergers can occur between a central galaxy and a satellite galaxy, and between two satellite galaxies. In MS-I, the minimum resolved halo has a mass of $1.7 \times 10^{10} h^{-1} M_{\odot}$. The stellar mass of the galaxy within a given dark matter subhalo is thus usually smaller than the subhalo mass, except for very massive satellite galaxies. In MS-II, however, the minimum halo mass is $1.4 \times 10^8 M_{\odot}$, and it is more common that the stellar mass of a galaxy becomes larger than the mass of its host subhalo even before we lose the track of the subhalo. We therefore change the treatment of mergers from DLB07 where a satellite galaxy follow its host subhalo until it is finally disrupted and a dynamical friction time until merging is then estimated. Here when the mass of a subhalo drops below that of its central galaxy, we already set the countdown clock for merging. After this point, the position and velocity of the satellite galaxy are traced by the most bound particles of the subhalo at the time when the merger clock is switched on. Following Croton et al. (2006), we adopt the dynamical friction formula of Binney & Tremaine (1987) to estimate the merging time for a satellite galaxy,

$$t_{friction} = \alpha_{fric} \frac{V_{vir} r_{sat}^2}{G m_{sat} \ln \Lambda}. \quad (5.32)$$

where $\alpha_{fric} = 2.34$. This value is higher than those adopted by Croton et al. (2006) but is consistent with DLB07. As described in DLB07, the factor of 2 is introduced to reproduce the luminosity functions at the luminous end. This factor is also found to be appropriate in the analysis of N-body simulations by Boylan-Kolchin et al. (2008) and Jiang et al. (2008). m_{sat} is the sum of the stellar mass of the satellite galaxy and the mass of its subhalo, r_{sat} is the distance between the central and satellite galaxies at the time when we start the merger clock, and $\ln \Lambda = \ln(1 + M_{vir}/m_{sat})$ is the Coulomb logarithm. After a time $t_{friction}$ the satellite galaxy is assumed to merge with the central galaxy of the main halo. If a main halo is accreted onto a larger system and becomes a subhalo, its satellite galaxies keep orbiting within this subhalo and will merge into the galaxy in the center of this subhalo. In this way, our model allow mergers to occur both between central galaxies of main halos and their satellite galaxies, and between the galaxies in the centers of subhalos and their own satellites.

Mergers are classified into major and minor mergers. Major mergers happen between two galaxies with baryonic mass ratio less than 3. More extremely mass ratios are considered as minor mergers. During major mergers, the disks of the progenitors are destroyed completely, leading to the formation of a spheroidal remnant. For minor mergers, cold gas of the minor (less massive) progenitor is added to the disk of the major (more massive) progenitor, while all the stars from the minor progenitor are added to the bulge of the main progenitor. In both cases, merger triggers a strong star formation event (a starburst). Here we adopt the “collisional starburst” model in Somerville et al. (2001). When merger happens, a fraction, e_{burst} , of the cold gas of the merging galaxies is converted into stars,

$$e_{burst} = 0.56 * \left(\frac{M_{minor}}{M_{major}}\right)^{0.7}.$$

where M_{minor} and M_{major} are the total baryon masses in the minor and major progenitors, respectively. As a consequence, strong SN feedback after a major merger can expel almost all the remaining cold gas and suppress further star formation until a new gas disk grows.

5.3.7 Bulge Formation

There are two modes of bulge formation included in our model: major mergers and disk buckling.

During major mergers, all stars of the progenitor and the newly formed stars end up in a spheroidal component, while during minor mergers, stars from the minor progenitor are added to the bulge of the major progenitor. In both cases, the spheroidal component grows in mass and changes in size. We apply energy conservation and the virial theorem to derive the bulge size of the remnant:

$$c \frac{GM_{new,bulge}^2}{R_{new,bulge}} = c \frac{GM_1^2}{R_1} + c \frac{GM_2^2}{R_2} + \alpha_{inter} \frac{G(M_1 \times M_2)}{R_1 + R_2}, \quad (5.33)$$

where c is a structure parameter and α_{inter} is a parameter quantifying the interaction energy. We adopt $c=0.5$ and $\alpha_{inter} = 2$. The term on the left-hand side is the binding energy of the final bulge: $M_{new,bulge}$ is its stellar mass and $R_{new,bulge}$ is its half-stellar-mass radius. The first and second terms on the right-hand side are the binding energy of the mass involved in mergers for the major and minor progenitors individually, and the third term is their orbital binding energy at merger. For major mergers, M_1 and M_2 are the sum of the mass of stars and of the cold gas converted into stars for the two progenitors, and R_1 and R_2 are the corresponding half mass radii. For minor mergers, M_1 and R_1 are the mass and half mass radius of the bulge of the major progenitor, and M_2 and R_2 are the stellar mass and the half-stellar-mass radius of the minor progenitor.

Secular evolution is also important for the formation of galaxy bulges, in particular in systems where the self-gravity of the disk is dominant. Here we adopt the treatment of Mo et al. (1998) to delineate disk instability:

$$\frac{V_{max}}{GM_{*,D}/R_{*,D}} < 1 \quad (5.34)$$

where $M_{*,D}$ and $R_{*,D}$ are the disk stellar mass and three times exponential scale radius. When the above criterion is met, we transfer mass, δM_* , from the disk to the bulge to keep the disk marginally stable. We assume that the mass is transferred from the inner part of the disk and the bulge formed in this way occupies the corresponding region:

$$\delta M_* = 2\pi\Sigma_*0R_{*,d}[1 - (R_b + R_{*,d})\exp(-R_b/R_{*,d})] \quad (5.35)$$

where R_b is the half-mass radius of the newly formed bulge, and covers the region from which the stellar mass is transferred into the bulge. If there is already a bulge present before mass transfer, we assume a disk instability leads to the formation of a new bulge with half mass radius R_b , which “merges” into the existing bulge in the same way as in galaxy mergers, simply replacing M_1 and R_1 with the mass and half mass radius of the existing bulge, and replacing M_2 and R_2 with δM_* and R_b .

5.3.8 Black Hole Growth and AGN feedback

There is growing evidence that galactic nuclear activity is closely related to galaxy formation. Here we follow Croton et al. (2006) to separate black hole growth into two modes : ‘quasar’ mode and ‘radio’ mode.

The quasar mode applies to black hole growth during gas-rich mergers. When a merger happens, the central black hole of the major progenitor grows both by absorbing the central black hole of the minor progenitor, and by accreting cold gas. The total growth in mass is calculated as

$$\delta M_{BH} = M_{BH,minor} + f \frac{M_{minor}}{M_{major}} \frac{M_{cold}}{1 + (280 \text{ km s}^{-1} / V_{vir})}, \quad (5.36)$$

where $M_{BH,minor}$ is the mass of the black hole in the minor progenitor, M_{cold} is the total cold gas in the two progenitors, and M_{minor} and M_{major} are the total baryon mass in the minor and major progenitors, respectively. Here f is a free parameter, which is set to be 0.03 (Croton et al. 2006) in order to reproduce the observed local $M_{BH} - M_{bulge}$ relation. Both major merger and gas-rich minor mergers can contribute significantly to the growth of the black hole. The relative role of these two mechanism needs more detailed study, but is beyond the the scope of the current work.

The radio mode applies to hot gas accretion onto central black holes. Black hole growth in this mode is calculated as

$$\delta M_{BH} = 6.96k f_{hot} \left(\frac{T_{vir}}{10^7 K}\right)^{3/2} \left(\frac{M_{BN}}{10^9 M_\odot}\right), \quad (5.37)$$

where f_{hot} is the ratio of hot gas mass to the total mass within the dark matter halo, and k is a free parameter which is $4.5 * 10^{-5} M_\odot / yr$ in our best fit model.

Following Croton et al. (2006), we assume that 10% of the energy produced near the event horizon is injected into the surrounding medium and reheats the cooling gas to the virial temperature:

$$E_{radio} = 0.1 \dot{M}_{BH} c^2, \quad (5.38)$$

where c is the speed of light. The effective cooling rate is thus

$$\dot{M}_{cool,eff} = \dot{M}_{cool} - 2E_{radio}/V_{vir}^2. \quad (5.39)$$

This effect is found to be more effective at low redshift, and in massive objects, where the black hole is more massive and the fraction of hot gas is higher. This effect has a very weak, if any, dependence on environment (Croton & Farrar 2008). Note that the radio mode also applies to satellite galaxies at the centers of subhalos in our model, while in DLB07, there is no hot gas left in subhalos and thus radio mode is quenched there automatically.

5.3.9 Metal Enrichment

We follow De Lucia et al. (2004) and Croton et al. (2006) when treating metal enrichment in different galaxy components. We briefly summarize the processes here. As stars evolve, a yield of heavy elements, Y , as well as a fraction of the initial stellar mass, are returned to the ISM. Here we assume instantaneous cycling between the newly formed stars and the cold gas in the disk. A more realistic treatment that takes into account the time delay between star formation and SN explosions (both type I and type II), as well as the different heavy element yields associated with these two kinds of supernova, will be implemented in future work. The cold gas carries metals with it when reheated by SN feedback, and is assumed to mix evenly with the hot gas in halos. The metals in the hot atmosphere may then be ejected with the ejected hot gas into the surroundings of the halo. Conversely, as ejected gas is reincorporated into the halos, it carries its metal fraction with it. A detailed description of metal enrichment and the exchange between different components can be found in De Lucia et al. (2004). Fig. 5.2 shows the gas metallicity as a function of stellar mass for star-forming galaxies. The solid curves are taken from Tremonti et al. (2004) and the black dots in the top panel are our results. This plot shows that our model successfully reproduces the tight observed relation between gas metallicity and stellar mass. This is mainly due to our introduction of a velocity dependence in the SN feedback. For comparison, in the bottom panel we show the results predicted by DLB07 model, where the SN feedback efficiency is a constant ($\beta_1 = \beta_2 = 0$). In this model both the amplitude and the slope at the low-mass end fail to match observations.

5.3.10 Stellar Synthesis and Dust Extinction

To compare model prediction with observations, we need to calculate the photometric properties of our model galaxies. Here we use the stellar population synthesis models from Bruzual & Charlot (2003). We adopt a Chabier initial function which has fewer low-mass stars than a Salpeter IMF. A detailed description can be found in De Lucia et al. (2004).

To include the extinction due to dust, we adopt the slab model developed by Guo & White (2009). The dust extinction is modeled as a function of gas column density, metallicity and redshift (see Chapter 3 and references therein).

5.4 Results

We have implemented our galaxy formation model on the MS-I and MS-II simulations simultaneously. These differ in mass resolution by a factor 125. In the following, we first study resolution effects on galaxy properties, then compare model galaxy properties to observation, and give some predictions for the intracluster light.

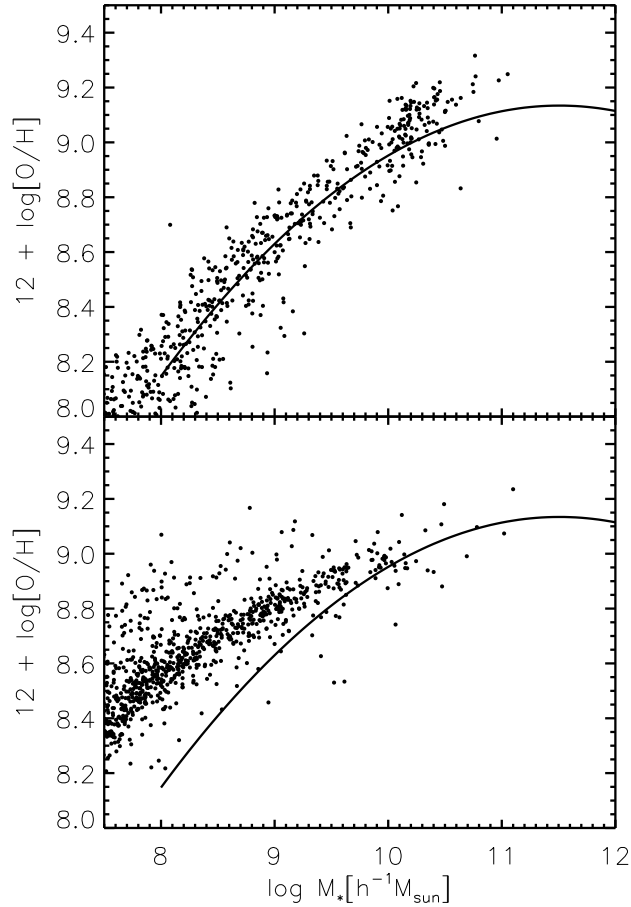


Figure 5.2: Gas metallicity vs. stellar mass. The top panel shows results for the model of this chapter (black dots) while the bottom panel shows results for the DLB07 model. In both panels, the solid curves show observational results for the SDSS by Tremonti et al. (2004)

5.4.1 Global Mass Function and Luminosity Functions

Fig. 5.3 shows the global galaxy stellar mass functions (GSMF) for the two simulations. The green open circles are results for MS-II and red ones for MS-I. The galaxy stellar mass functions in the MS-I and in the MS-II converge above a stellar mass about $10^{10} M_{\odot}$. The difference at the low mass end is due to mass resolution: the minimum halo mass resolved in the MS-I is $1.7 \times 10^{10} h^{-1} M_{\odot}$ versus $1.36 \times 10^8 h^{-1} M_{\odot}$ in the MS-II. Thus the formation of galaxies in low-mass halos is not well-resolved in MS-I and their masses are underestimated. At high mass, the two simulations diverge mainly due to cosmic variance: the volume of the MS-II is smaller than the MS-I by a factor 125. Boylan-Kolchin et al. (2009) show that this divergence is more prominent at high redshifts. As may be seen in Fig. 5.3, adopting the MS-II GSMF below about $10^{10} M_{\odot}$ and the MS-I GSMF at higher masses results in a very good match to the observational result from the SDSS DR7 (Li & White 2009).

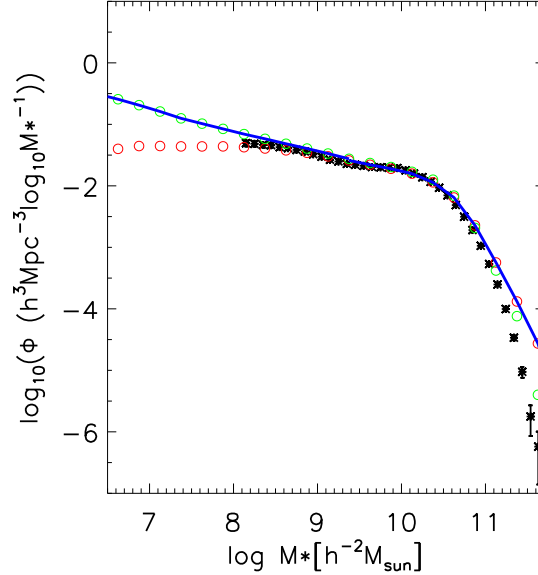


Figure 5.3: Galaxy stellar mass functions. Green open circles are from the MS-II and red open circles are from the MS-I. The thin black line is the SDSS DR7 result from Li & White (2009).

Our model reproduces the global GSMF well from $\sim 10^{12}/h^2 M_\odot$ all the way down to $10^8/h^2 M_\odot$. We find the slope at the low-mass end in the model to be around -1.32, slightly steeper than that found by Li & White (2009): -1.155. The high resolution of MS-II allows us to study galaxy abundances to even lower mass. Here we show the predicted GSMF down to $10^{6.8} M_\odot$. The corresponding number density is around $0.3 h^3 \text{Mpc}^{-3} \log_{10} M_*^{-1}$. We investigate the abundance of even small galaxies, such as the satellite galaxies around the Milky Way, whose typical stellar mass is even below $10^7 M_\odot$ in section 5.4.3. At high stellar masses, where the mass is determined by AGN feedback (Croton et al. 2006), our model overpredicts the abundance found by Li & White (2009). This may reflect the observational uncertainty in estimating stellar masses for the most luminous cD galaxies in clusters. It is possible that the SDSS photometry underestimates the luminosities of such galaxies significantly.

An important constraint on galaxy formation models is that they should convert a proper amount of baryons into stars in halos of given mass. Fig. 5.4 shows the relation between the stellar mass and the dark matter halo mass for central galaxies in our model at $z = 0$. Dark matter halo mass refers here to the current virial mass for main subhalos, and to the virial mass at the time of infall for subhalos. Our model predictions are shown as a scatter plot. The line is the relation derived using the abundance matching between the observed galaxy stellar mass function and the maximum dark matter halo mass function (see Chapter 4). These two relations match each other fairly well. The scatter for the model is quite small, though for low-mass halos, a few galaxies have stellar mass as large

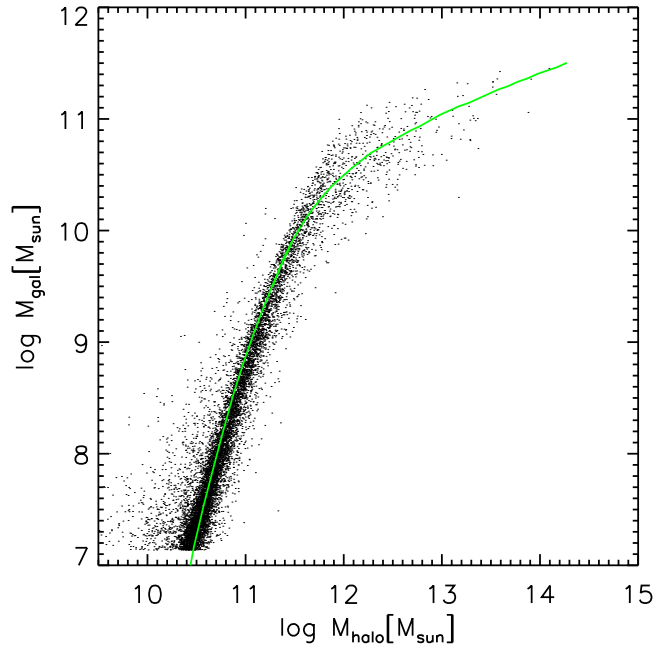


Figure 5.4: Galaxy stellar mass vs. dark matter halo mass. Dark matter halo mass refers to the maximum mass obtained in the history. The small dots are for the model predictions and the green curve is the relation derived from the SDSS GSMF and the dark matter mass function under the assumption of a monotonic relation between galaxy stellar mass and dark matter halo mass.

as $\sim 10\%$ of their host halo mass. This supports the assumption of a monotonic relation between galaxy stellar mass and dark matter halo mass adopted in the last Chapter.

Fig. 5.5 shows luminosity functions in SDSS g and r bands. The observational results (black stars) are best fits from Bell et al. (2003). Our predicted luminosity functions agree reasonably well with the SDSS data in both bands. The model, however, overpredicts the abundance of very luminous galaxies in the g band. These are massive galaxies whose recent growth is dominated by mergers. This effect is at least partly due to our over-simplified treatment of starbursts during mergers. Our model predicts a turn-up at low luminosity end (g-band), which is also seen in Bell et al. (2003) data, though it is missed in the fitting formula.

5.4.2 Correlation Functions

In this subsection we study the autocorrelation of stellar mass and standard galaxy auto-correlation functions for stellar mass limited samples of galaxies.

Fig. 5.6 shows the stellar mass autocorrelation using galaxies with $M_* > 10^8 h^{-1} M_\odot$. The results from the MS-I (red circles) and the MS-II (green circles) converge well beyond 1Mpc. Within 1Mpc, the results from the MS-I are slightly higher than from MS-II. This may reflect a slightly overestimation of galaxy merger times in the lower resolution MS-I. Li & White (2009) find that the main contribution to the autocorrelation of stellar mass

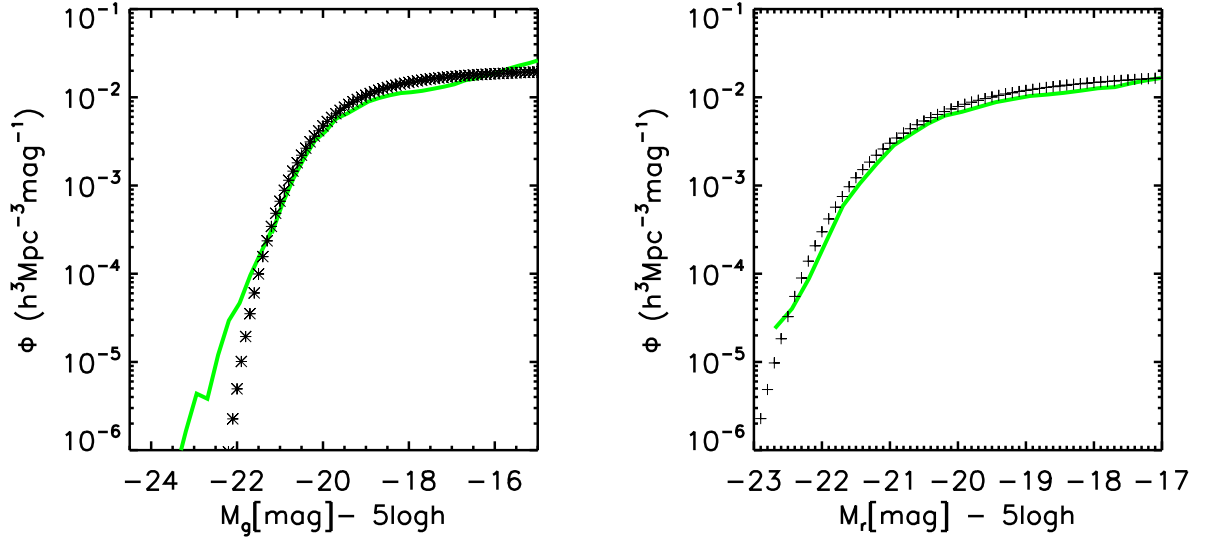


Figure 5.5: Galaxy luminosity functions in the g (left) and r (right) photometric bands. Symbols are the best fitting from observational results by Bell et al. (2003). Solid curves are the model predictions.

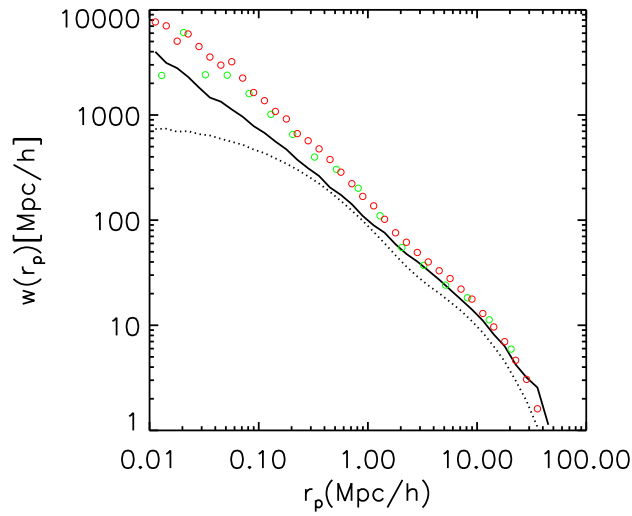


Figure 5.6: Projected stellar mass autocorrelation functions. The green circles are for the MS-II and the red are for the MS-I. The results from these two simulations converge well. The solid curve represents the results in the SDSS (Li et al. 2009). The dotted curve, for comparison, is the projected autocorrelation function of dark matter in the MS-I.

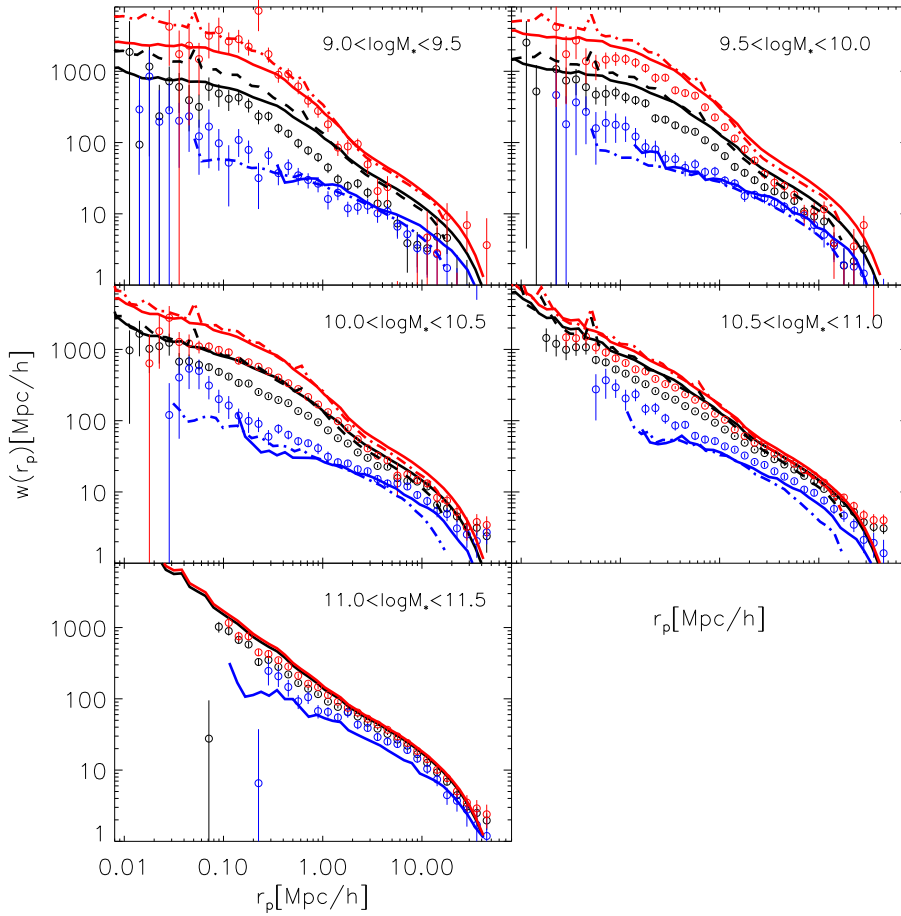


Figure 5.7: Projected two point correlation functions for galaxies with different stellar masses. Solid curves are for the MS-I and dash-dotted curves are for the MS-II. Symbols with error bars are for SDSS data (Li et al. 2006). The black curves and symbols are for all galaxies with stellar mass within the corresponding stellar mass bin as indicated on the top right corner of each panel. The blue curve and blue symbols are for the blue galaxy population, and the red are for the red galaxy population (see the definition of blue and red galaxies in the text). The results on MS-I and MS-II converge for galaxies more massive than $10^{9.5} M_{\odot}$, which corresponds to the resolution limit in MS-I.

comes from galaxies with stellar masses similar to the Milky Way, where abundance from the two simulations converge (see the stellar mass functions in sec. 5.4.1 and the mass-dependent galaxy correlation functions below). The solid curve is the estimate from the SDSS (Li & White 2009). It shows that although the model prediction agrees qualitatively with observations, the predicted amplitude is higher by about 10% for the two-halo term and by upto a factor of 2 in one-halo term on the smallest scales. This suggests the need of adopt a lower value of σ_8 , as discussed in Li & White (2009).

Fig. 5.7 shows projected two point correlation functions for galaxies in various stellar mass

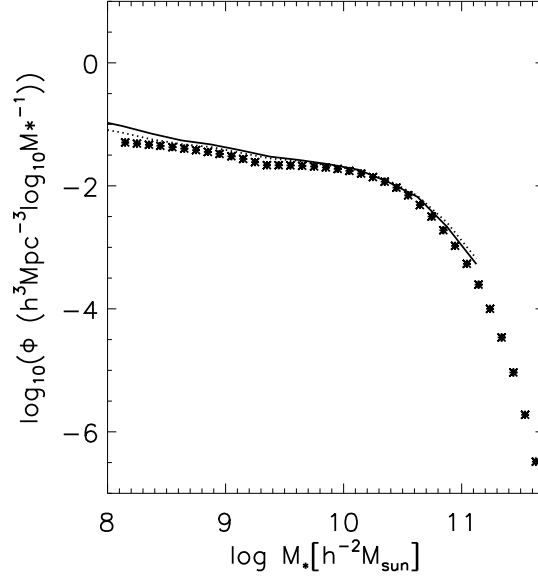


Figure 5.8: Galaxy stellar mass functions. The solid curve is the GSMF without reionization and the dotted curve is the GSMF with reionization. Reionization does not much affect the formation of galaxies more massive than $10^8/h^2 M_\odot$.

bins. The mass unit is $[h^{-1}M_\odot]$. In each mass bin, we further divide the galaxies into blue and red populations according to their $g-r$ colors. Black curves give the total correlation function in each stellar mass bin. Blue curves are for the blue galaxy populations and the red for red galaxy populations. The solid curves are for the MS-I and the dot-dashed curves are for the MS-II. Results in the most massive bins are only shown for MS-I because there are only a few galaxies in the MS-II in this mass range. Results in the two simulations converge for galaxies more massive than $10^{9.5}M_\odot$. Open circles are observational results taken from the SDSS DR4 (Li et al. 2006). The variation in correlation functions across the various stellar mass ranges agree qualitatively with those observed. The difference between the correlation functions of red galaxies and those of all galaxies in the corresponding bin is similar to what is found in the SDSS. The red galaxy correlation functions of small galaxies, $10^9/hM_\odot < M < 10^{9.5}/hM_\odot$, are well reproduced in our model. Although our model is much improved with respect to that of DLB07, where hot gas atmospheres are stripped out instantaneously after subhalo infall, our model still underpredicts the number of close blue pairs seen in the SDSS. The overall amplitude of the correlation function is higher than observed at all scales in all mass bins, again indicating that the value of σ_8 used in the MS-I and MS-II is probably too large.

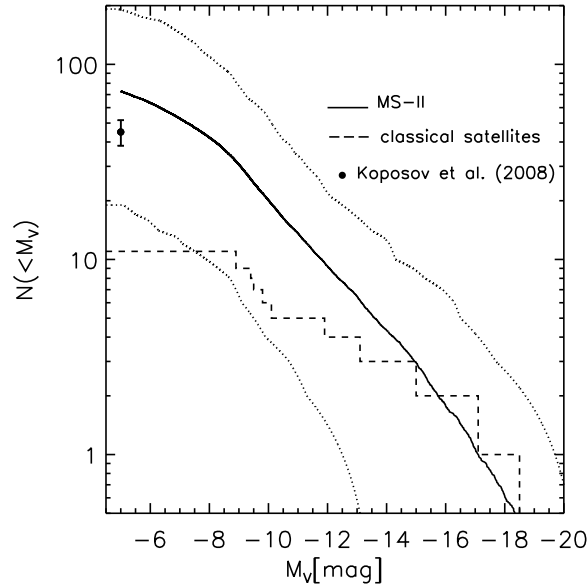


Figure 5.9: Cumulative luminosity functions of the Milky Way satellite galaxy. Solid curve is the median value of the model prediction, and dotted curves are 10% and 90% regions. The observed 11 classical Milky Way satellite galaxies are represented using the dashed curve. The big dots represents the most recent results by Koposov et al. (2008) using SDSS.

5.4.3 Satellite Luminosity Function around the Milky Way

In this subsection we study the luminosity function of satellite galaxies in Milky-Way like systems. In MS-II, there are around 7000 halos with mass comparable to that of the Milky Way’s host halo, and its mass resolution turns out to be just sufficient to study even the faintest dwarf spheroidals observed so far. Here we select 1000 central galaxies with stellar mass between 4 and $6 \times 10^{10} M_{\odot}$ from the MS-II. All other galaxies within 280kpc are defined as satellite galaxies. We show the V-band cumulative satellite luminosity function in Fig. 5.9. The solid curve is the median value, and the dotted curves are the 10% and 90% regions. A dashed curve represents the 11 classical satellite galaxies around the Milky Way. The big dot with error bar at $M_v \sim -5$ is estimated from Koposov et al. (2008). The observed luminosity function falls well within our 10% to 90% region. Our simulated Milky Way systems have the right number of satellites all the way from bright LMC/M33 like systems down to the faintest objects yet found around the Milky Way. Note that all our parameters were fixed with reference to the global stellar mass function. The satellite luminosity functions then come “for free”.

Reionization is always an important consideration in the formation of low mass galaxies. In Fig. 5.8, we show the global stellar mass functions with and without reionization. Here we focus on reionization effects on the formation of low mass galaxies and only use the MS-II simulation. The solid curve is the GSMF without reionization and the dashed curve

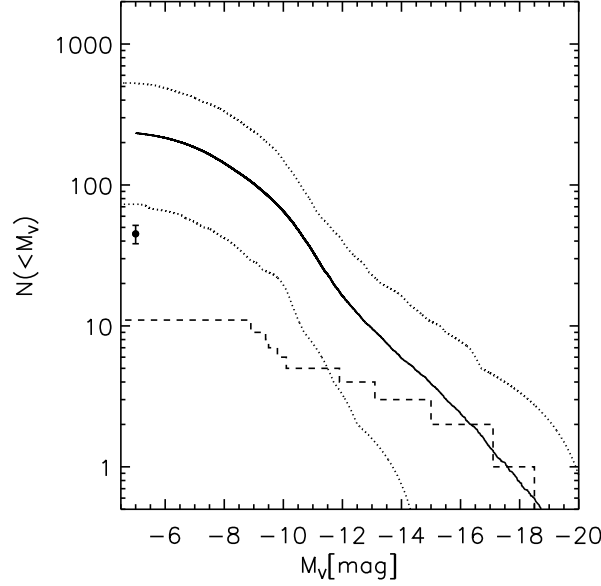


Figure 5.10: Cumulative luminosity functions for Milky Way satellites when reionization is ignored. The line coding is the same as in Fig. 5.9.

is that with reionization. The latter is identical to the open green circles in Fig. 5.3. Reionization has almost no effect on the formation of galaxies with mass above $10^8/h^2 M_\odot$. We turn to reionization effects on the formation of satellite galaxies in the Milky-Way-like systems, which are even lower in stellar mass. The result is shown in Fig. 5.10. Again, the solid curve is the median value and the dotted curves are the 10% and 90% boundaries. Reionization does not affect the formation of relative luminous satellite galaxies like the LMC or SMC, but it plays an important role in the formation of very faint satellites. The number density of galaxies with $M_V \sim -5$ is overpredicted by a factor of 5 if reionization is ignored. Thus although reionization does not affect the formation of galaxies more massive than the LMC, it significantly modifies the formation of low-mass dwarf spheroidals.

5.4.4 Galaxy Stellar Mass Function in Rich Clusters

The most massive halo in the MS-II has a mass of $\sim 10^{14.7} h^{-1} M_\odot$ and contains over 119 million particles. Substructures in this big halo are very well resolved. It is similar to the Coma cluster both in mass and in radius. Here we use this biggest halo to investigate the galaxy stellar mass function inside such a rich cluster. The result is shown in Fig. 5.11. The solid curve is the galaxy stellar mass function and error bars denote the Poisson errors. The slope at the low mass end is around -1.3, which is slightly higher than the observed r and R band slope for galaxies in the Coma cluster : ~ 1.16 (Beijersbergen et al. 2002; Mobasher et al. 2003), and consistent with recent observational estimates based on the SDSS galaxy cluster catalog (Popesso et al. 2005), though the observed slope at the very

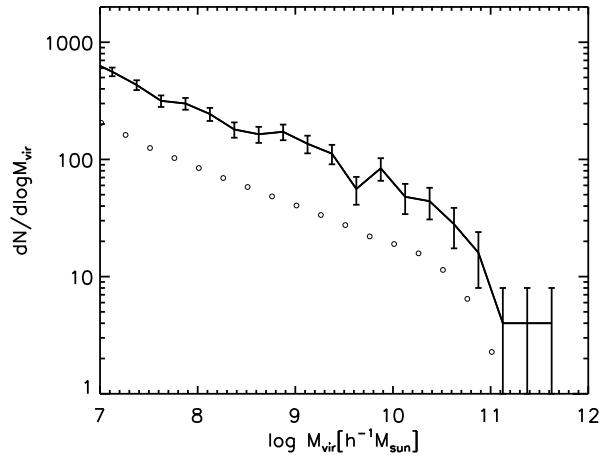


Figure 5.11: Satellite galaxy stellar mass function in a rich cluster. Error bars denote the Poisson errors. The open circles represent the global GSMF, renormalized arbitrarily to fit in the diagram in order to compare its shape to that of the cluster stellar mass function.

faint end in the Coma cluster is steeper (Adami et al. 2007; Jenkins et al. 2007; Milne et al. 2007). Given the large error bars, our model gives a reasonable prediction for the stellar mass function of galaxies within clusters. The circles here show the global stellar mass function, renormalized to fit in the diagram, in order to compare its shape to the stellar mass function in clusters. The shape of the stellar mass function in the simulated cluster does not show any significant difference in either characteristic mass or faint-end slope from the GSMF in the general field (Bai et al. 2006), indicating a general independence of galaxy formation from large-scale environment. This is interesting since both simulations and observation show the colour and morphology distributions of cluster galaxies to differ from those of the field.

5.4.5 Intracluster Light

Recent observations of diffuse intracluster light and intracluster stars (Zibetti et al. 2005; Gonzalez et al. 2000; Arnaboldi et al. 2002; Arnaboldi & et al. 2003; Gerhard et al. 2005; Mihos et al. 2005) indicate a large fraction of stars distributed in the diffuse intracluster medium. In our model, the diffuse stars come from disrupted satellite galaxies. In Fig. 5.12, we show the fraction of stars in the ICM as a function of cluster virial mass. Two kinds of fractions are considered. The black crosses show the fraction $F_{DSC} = M_{ICM,R_{vir}}/M_{*,R_{vir}}$, where $M_{ICM,R_{vir}}$ is the total mass of diffuse stars and $M_{*,R_{vir}}$ is the total stellar mass within the virial radius of the main halo R_{vir} . In our model around 5-10% of all the stars in galaxy clusters are distributed in the intracluster medium. This fraction increase slightly with the virial mass of the cluster and has a large scatter at the low mass end. Both the trends and the value are consistent with recent observational findings (Arnaboldi et al. 2004; Aguerri et al. 2005, 2006; Zibetti et al. 2005). Another fraction we considered is

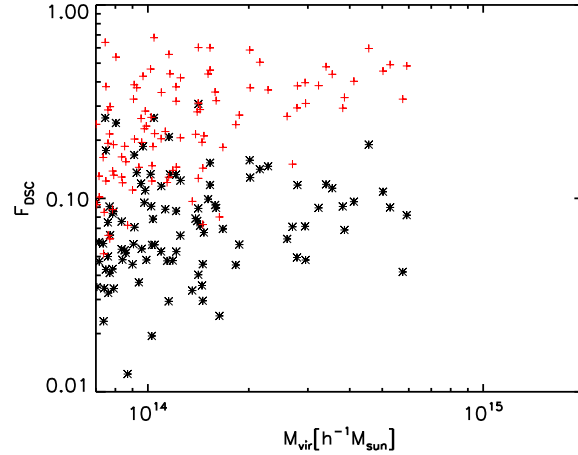


Figure 5.12: The fraction of intracluster stars as a function of virial mass for clusters. Black stars show the total fraction of stars in the ICM within the virial radius of the main halo. Red crosses shows the ratio of diffuse stellar mass to diffuse + central galaxy stellar mass.

$F_{DSC} = M_{ICM,cen}/M_{*,cen}$, where $M_{ICM,cen}$ is the mass of diffuse star associated with the main subhalo and $M_{*,cen}$ is the sum of $M_{ICM,cen}$ and the stellar mass of the central galaxy. These are shown using red crosses. This fraction increases with cluster virial mass, ranging from 18% in clusters of mass $\sim 7 \times 10^{13} h^{-1} M_{\odot}$ to 40% in clusters of mass $\sim 10^{15} h^{-1} M_{\odot}$. In halos of mass $> 3 \times 10^{14} h^{-1} M_{\odot}$, the typical value is around 40%, which means that the stars locked in the central galaxy of such a galaxy cluster are comparable in mass to those in the diffuse phase. This is consistent with the fact that the cD galaxy usually has a large, diffuse envelope with similar stellar mass to the more concentrated central region.

5.5 Conclusion and Discussion

The study of dwarf galaxy formation is key to understanding the effects of SN feedback, of mass exchange between different baryonic components, of reionization, and of environmental stripping processes. For the first time, the combination of the MS-I and MS-II has made it possible to study in a single consistent model the statistics of the formation of galaxies from the faintest dwarf spheroidals to giant cD galaxies in clusters. In this work, we implement an updated galaxy formation model on the output of the MS-I and MS-II, focusing on the treatment of SN feedback, gas reincorporation, galaxy size and the stripping and disruption of satellite galaxies. Results from these two simulations converge well for galaxies with $M_* > 10^{10} M_{\odot}$. At high mass the MS-I gives good statistics, while at low mass the MS-II provides well-resolved galaxy assembly histories.

By including strong SN feedback and a long reincorporation timescale for small galaxies, we are able to reproduce both the amplitude and the slope of the observed galaxy stellar

mass function from $10^8/h^2 M_\odot$ to $10^{12}/h^2 M_\odot$. As found by Croton et al. (2006), the stellar mass of rare, massive galaxies is determined by AGN feedback.

The stellar mass correlation predicted by our model agrees quite well with the SDSS estimates for $r > 1 \text{ Mpc}$, but it is higher by a factor of 2 at the smallest scales ($r \sim 10 \text{ kpc}$). Correlation functions for galaxies in various stellar mass ranges are also qualitatively well reproduced, including the strong dependence on colour at fixed mass. All these model correlation functions are, however, higher than observed on large scales, indicating that a lower value of σ_8 is preferred in the real Universe than adopted in the MS-I and MS-II.

Remarkably, without further adjustment our model reproduces the luminosity function of satellite galaxies in Milky-Way like systems down to $M_V \sim -5$. We find that reionization does not significantly affect the formation of galaxies larger than the SMC, but it plays an important role in the formation of very low-mass dwarf spheroidals.

The galaxy stellar mass function in a model rich cluster, like the Coma cluster, can be fitted by a Schechter function with a characteristic stellar mass $\sim 8 \times 10^{10} M_\odot$, slightly higher than the value for the global GSMF. The slope at the low-mass end is slightly steeper than in the real Coma Cluster when estimated from r-band observations. The shape of the stellar mass function of cluster galaxies is very similar to the GSMF in the general field, implying that environment has little effect in establishing the stellar mass distribution.

We find that around 5% to 10% of all the stars in a galaxy cluster are distributed in the diffuse intracluster medium. This fraction increases slightly with the mass of the the host cluster. In our model around 40% of the stars associated with the central galaxy and its stellar halo are in the diffuse envelope. This is consistent with observational estimates for cD galaxies.

The introduction of gradually stripping and disruption of satellite galaxies has helped to bring the blue fraction in clusters, as well as star formation rates in satellite galaxies into better agreement with observation. In follow up work, we will study in detail galaxy evolution in different environments and explore the relative roles that different mechanisms play in galaxy evolution in clusters.

Concluding remarks

In this thesis, I have made use of high-resolution numerical dark matter simulations and the semi-analytic technique to study galaxy formation and evolution in the context of a Λ CDM cosmology. It consists of four projects. In the following, I will first summarize the main results of this thesis and then outline the follow-up projects that I plan to do.

In the standard scenario of galaxy formation, galaxies form at the center of hierarchically merging dark matter halos. However, galaxy formation is much more complicated than the formation of dark matter halos because it involves dissipative, poorly understood baryonic processes.

In Chapter 2, I studied the role that mergers played in the growth of galaxy stellar mass, and compared to the situation for dark matter halos. This work is based on a model galaxy catalogue which was calculated by coupling the galaxy formation model of De Lucia & Blaizot (2007) to the Millennium Run Λ CDM N-body simulation. I find that the mass and redshift dependence of galaxy mergers differs completely from that of dark matter halo mergers. Galaxy growth through a major merger is a strong function of stellar mass but depends at most weakly on redshift, while dark matter halo growth through a major merger is proportional to $(1+z)$, but the mass dependence is very weak. At high redshift, star formation dominates the galaxy growth for all masses except the most massive ones. For galaxies comparable in mass to the Milky Way, mergers start to dominate only after $z = 1$. While for dark matter halos, at all redshifts and for all masses, mergers play a more important role in the mass growth than the accretion of “diffuse” particles. The build-up of dark matter halos through mergers is not parallel to galaxies. Another interesting finding is that the star formation efficiency is a decreasing function of stellar mass both in the local universe and at high redshift.

In Chapter 3 I investigated the predictions for high-redshift galaxies and their evolution in a Λ CDM cosmology. I developed a redshift dependent dust model and created a new photometric table for model galaxies in the catalogue used in Chapter 2. This is to reproduce the abundances of three high redshift populations: Lyman break galaxies at $z \sim 3$ (LBGs), optically selected star-forming galaxies at $z \sim 2$ (BXs), and distant red galaxies at $z \sim 2$ (DRGs). I made mock catalogues and selected these three high redshift populations using exactly the observational colour and apparent magnitude criteria. I first

compare the model galaxies with the observed ones, and then use the model to predict their evolution and study the relation between their descendants and local galaxies.

The model is successful in reproducing the abundances, redshift distributions and clustering of all three observed populations simultaneously. The star formation rates of model LBGs and BXs are, however, lower than those quoted for the real samples. I attribute this at least partly to the difference in initial mass functions adopted in the model and by observers. Interestingly, model DRGs are found to be star-forming galaxies. Their star formation rates cover the range from 1 to $\sim 100M_{\odot}/\text{yr}$ and peak at $\sim 30M_{\odot}/\text{yr}$, which is similar to, or even higher than, the BXs and LBGs. Most (85%) of the massive galaxies ($M_* > 10^{11}M_{\odot}$) are identified as DRGs or BXs, while they together only account for 30% of the star-forming galaxies ($\dot{M}_* > 20M_{\odot}/\text{yr}$) at $z = 2.2$. The rest are gas- and metal-rich systems which are strongly obscured and are thus missing in current optical and near-infrared surveys.

I find rather little overlap between these DRGs and BXs or LBG-descendants, though they are all star-forming galaxies at $z = 2.2$. In contrast, around half of LBG descendants are identified as BXs (LBG-BXs) at $z \sim 2.2$. There is no significant difference in stellar mass, color and morphology distributions and correlation functions between the LBG-BXs and BXs.

The typical stellar masses for model LBGs and BXs are $\sim 10^{9.9}M_{\odot}$ and they contribute 30% of the most massive galaxies ($M_* > 10^{11}M_{\odot}$) at the relevant redshifts, while for model DRGs the typical stellar mass is $\sim 10^{10.7}M_{\odot}$ and they contribute 65% of the most massive galaxies at $z = 2.2$. The stellar mass increases by a factor of ~ 10 and ~ 3 for LBG/BXs and DRGs respectively. At $z = 0$, many of them end up as massive elliptical galaxies, though they are identified as disk-dominated galaxies at the relevant redshift. Over 70% of the model galaxies with $M_* > 10^{11}M_{\odot}$ at $z = 0$ have at least one LBG/BX/DRG progenitor; around half the stars in the central galaxies of rich clusters have already formed in these high-redshift galaxies. Following the growth history of these high-redshift populations, I find that star formation dominated their growth until $z \sim 1$ and then mergers become dominant. This is coincident with the results we found for the growth of the Milky-Way-like systems (see Chapter 2). However, the clustering for descendants of all three populations is stronger than that of the Milky-Way-like galaxies by $z = 0$, indicating that they have different evolution histories from the Milky Way.

Results in Chapter 2 and Chapter 3 are based on a particular galaxy formation model. In Chapter 4, I established a galaxy-formation-model independent link between galaxy stellar mass and dark matter halo mass. This is achieved by using the galaxy stellar mass function from the SDSS and the dark matter halo mass function derived from the combination of the MS-I and MS-II, and by assuming a one-to-one monotonic relation between the stellar mass of a galaxy and the maximum mass ever attained by its dark matter halo. I first compare the predicted halo mass as a function of galaxy stellar mass with direct measurement using weak lensing. It shows good agreement between these two, which supports the self-consistency of the Λ CDM model. The stellar mass ‘‘Tully-Fisher’’ relation has also been qualitatively reproduced especially after taking baryon effects into account. In contrast to previous assessments, this implies that it is possible to simultaneously reproduce observed luminosity functions and Tully-Fisher relations in the context of Λ CDM cosmology.

I then compare the predicted virial mass of Milky-Way-like systems to recent observations

and find that though the prediction is slightly higher than many estimates from observations of halo tracers, it is consistent with the MW/M31 Timing Argument.

One important application of this work is to pose constraints on direct galaxy formation simulations. I defined a galaxy formation efficiency as the fraction of the baryons in the form of stars in the central galaxy of a given halo. This efficiency reaches a maximum of 20% at masses slightly below that of the Milky Way and falls rapidly at both higher and lower masses. Most recent direct simulations fall above this maximum value by at least a factor of 2, showing that they have converted too many baryons into stars to be viable models for typical spiral galaxy formation.

Finally, in Chapter 5, I shifted the focus to the formation of dwarf galaxies. The formation of these low-mass systems is sensitive to SN feedback, the mass exchange between different baryonic components, reionization, and environmental stripping processes. I developed a new galaxy formation model, mainly focusing on these processes, and implemented it on the MS-I and the MS-II simulations. The combination of the MS-I and MS-II enables us to study the statistics of the formation of galaxies from the luminous cD galaxies in clusters all the way down to the faintest dwarf spheroidals. This model has been able to reproduce both the amplitude and the slope of the observed galaxy stellar mass function from $10^8/h^2 M_\odot$ to $10^{12}/h^2 M_\odot$. Meanwhile, it reproduces the luminosity function of satellite galaxies in Milky-Way-like systems down to $M_V \sim -5$ without any further adjustment. Detailed study shows that the circular-velocity-dependent SN feedback is necessary to reproduce the observed galaxy stellar mass function down to $10^8 M_\odot$, and that reionization is only important for the formation of the faintest spheroidals.

I find that in rich clusters like the Coma cluster, the shape of the simulated galaxy stellar mass function does not show any significant difference in either characteristic mass or faint-end slope from that in the general field, which implies that environment has little effect in establishing the stellar mass distribution. Around 10% of stars in clusters are distributed in the intracluster medium, though the scatter is very large. This fraction increases slightly with the mass of clusters and can reach more than 20% in the most massive halos. Concerning on the central galaxies in cluster centres, I find that around half of the stars associated with the central galaxies and their stellar halos are in the diffuse envelope, which is consistent with observational estimates for cD galaxies.

This model has been able to reproduce the observed stellar mass correlation at scales $r > 1\text{Mpc}$, but fails at small scales: the model prediction is higher by almost a factor of 2 at $r \sim 10\text{kpc}$. The observed correlation functions for mass-limited samples of red and blue populations are qualitatively reproduced by our model. All the amplitudes are, however, higher than observed on large scales, suggesting the need for a lower value of σ_8 than adopted in the MS-I and MS-II.

The following outlines several projects which will complement and extend what has already been achieved in this thesis.

In Chapter 5, I show that the correlation functions of stellar mass and those of galaxies suggest that the matter power spectrum normalization, σ_8 , is somewhat lower in the real Universe than adopted by the MS-I and the MS-II. I plan to implement the galaxy formation model onto outputs of N-body simulations, which are adapted/rescaled to different cosmologies (Angulo et al. in prep.) in order to constrain cosmology parameters. Wang et al. (2008) suggest that the WMAP1 and WMAP3 cosmologies can only be distin-

guished using high redshift galaxy properties, given the uncertainties in galaxy formation models. I plan to build mock galaxy catalogues based on a variety of cosmologies, and to compare with high redshift observations to constrain cosmology.

There is plenty of evidence of the existence of metals in the intergalactic medium (IGM). However, it is still not clear *how* the IGM is polluted. I plan to include a dynamical feedback model similar to that of Bertone et al. (2007) together with a more realistic treatment of metal recycling into our galaxy formation model as presented in Chapter 5. I will then look at metal abundances both in galaxies and in the intracluster medium. The latter can be compared to X-ray surveys in order to investigate the origin of the metals in the IGM.

The relative abundance of α elements and iron, which are contributed primarily by type II supernovae (SNII) and type Ia supernova (SNIa) respectively, are closely related to the star formation timescales of galaxies. I intend to construct a model which treats SNIa and SNII separately in terms of rates, timescales and metal yields. Besides clarifying their effects on galaxy formation histories, I also expect this analysis to give some constraints on SNIa lifetimes.

In Chapter 5 I have introduced gradual stripping and disruption of satellite galaxies. This has proven helpful in improving the blue fraction in clusters. In the future, I plan to investigate in detail the relative contribution of mergers, disruption and gas stripping in the evolution of galaxies in clusters. This will be compared to the evolution of galaxies in the field, in order to study the environmental effects on galaxy formation.

Acknowledgements

Now this thesis is finally finished. I cannot just stop here without thanks to all of people who make it possible.

Firstly, very warm thanks to my supervisor Simon White, not only for your invaluable advices on my work, but also for your continuous encouragement during all the last four years. It is you who trained me from an amateur astronomers to a real scientist. Thank you for forgiving me all the stupid mistakes I have made; thank you for giving me the opportunities to involve in all kinds of astrophysical activities; thank you for teaching me the research attitude and installing me the way to find new ideas... I have learned from you much more than I can write down here. It has been the most amazing experience in my life to work with you.

Many thanks to Guinevere Kauffmann. Thank you for organizing the weekly REAL GALAXY meeting. I learned a lot from that. It is also very happy to work with you and Fujian on the gas project. Thanks to Volker Spingel, for helping me with the numerical techniques. The whole thesis work is based on the frame code you built up. It is not possible to finish this thesis without it. Thanks to Mike, for helping me with the MS-II data and my English, and for your timely reply to my email. Many thanks to Gabriella for your valuable suggestions on my work. Thank you Manfred, for leaving me with the great light-cone code and teaching me how to use it.

Thanks to my dear friends Cheng, Roderik and Andreas, for useful discussions both scientifically and non-scientifically. I learned much from you guys and thank you for brought so much fun into my life. And also I enjoy the lunch with you. Many thanks to Liang. It is you who help me to come to this wonderful institute and who always encourage me when I was not self-confident. Thanks to ChunYan. You taught me to be independent with your own words and deeds. Thanks to HuiYuan, for being patient to all my questions (most time very stupid). Special thanks to Jie. Thank you for the science discussion and for the help in my daily life. Thanks to Xiao Ling for your wonderful food. I love it very much. Thank you, Simone, for recommending me the great gym and Yoga courses. Many thanks to my officemates, Umberto, Mona, Federico. Thank you for your warm friendships. Many thanks to all other friends: Yan-Mi, Francesco, Dimitri, Cecilia, Jing, Lu, Andre, Zhen, Dong, ZhongLi... I have so many people names in my mind and I cannot write down all of them.

I should not forget to present my acknowledgments to Cornelia, Kate, and Maria, for

Acknowledgements

you making my life here so much easier.

Finally, very special thanks to my family. You were and you are always there supporting me. Your love and encouragement are all my source of energy. I can finish nothing without you behind me.

Bibliography

- Abadi M. G., Navarro J. F., Fardal M., Babul A., Steinmetz M., 2009, ArXiv e-prints
- Abadi M. G., Navarro J. F., Steinmetz M., Eke V. R., 2003, ApJ, 591, 499
- Abazajian K., Sloan Digital Sky Survey f. t., 2008, ArXiv e-prints
- Abraham R. G., van den Bergh S., Glazebrook K., Ellis R. S., Santiago B. X., Surma P., Griffiths R. E., 1996, ApJS, 107, 1
- Adami C., Picat J. P., Durret F., Mazure A., Pelló R., West M., 2007, A&A, 472, 749
- Adelberger K. L., Steidel C. C., 2000, ApJ, 544, 218
- Adelberger K. L., Steidel C. C., Pettini M., Shapley A. E., Reddy N. A., Erb D. K., 2005, ApJ, 619, 697
- Adelberger K. L., Steidel C. C., Shapley A. E., Hunt M. P., Erb D. K., Reddy N. A., Pettini M., 2004, ApJ, 607, 226
- Aguerri J. A. L., Castro-Rodríguez N., Napolitano N., Arnaboldi M., Gerhard O., 2006, A&A, 457, 771
- Aguerri J. A. L., Gerhard O. E., Arnaboldi M., Napolitano N. R., Castro-Rodriguez N., Freeman K. C., 2005, AJ, 129, 2585
- Allen S. W., Schmidt R. W., Ebeling H., Fabian A. C., van Speybroeck L., 2004, MNRAS, 353, 457
- Arnaboldi M., Aguerri J. A. L., Napolitano N. R., Gerhard O., Freeman K. C., Feldmeier J., Capaccioli M., Kudritzki R. P., Méndez R. H., 2002, AJ, 123, 760
- Arnaboldi M., et al. 2003, AJ, 125, 514
- Arnaboldi M., Gerhard O., Aguerri J. A. L., Freeman K. C., Napolitano N. R., Okamura S., Yasuda N., 2004, ApJ, 614, L33

Bibliography

- Bacon D. J., Taylor A. N., Brown M. L., Gray M. E., Wolf C., Meisenheimer K., Dye S., Wisotzki L., Borch A., Kleinheinrich M., 2005, *MNRAS*, 363, 723
- Bai L., Rieke G. H., Rieke M. J., Hinz J. L., Kelly D. M., Blaylock M., 2006, *ApJ*, 639, 827
- Baldry I. K., Glazebrook K., Driver S. P., 2008, *MNRAS*, 388, 945
- Barnes J. E., 1988, *ApJ*, 331, 699
- Barnes J. E., 1992, *ApJ*, 393, 484
- Barnes J. E., Hernquist L. E., 1991, *ApJ*, 370, L65
- Battaglia G., Helmi A., Morrison H., Harding P., Olszewski E. W., Mateo M., Freeman K. C., Norris J., Shectman S. A., 2005, *MNRAS*, 364, 433
- Baugh C. M., Lacey C. G., Frenk C. S., Granato G. L., Silva L., Bressan A., Benson A. J., Cole S., 2005, *MNRAS*, 356, 1191
- Beijersbergen M., Hoekstra H., van Dokkum P. G., van der Hulst T., 2002, *MNRAS*, 329, 385
- Bell E. F., de Jong R. S., 2001, *ApJ*, 550, 212
- Bell E. F., McIntosh D. H., Katz N., Weinberg M. D., 2003, *ApJS*, 149, 289
- Bell E. F., Phleps S., Somerville R. S., Wolf C., Borch A., Meisenheimer K., 2006, *ApJ*, 652, 270
- Belokurov V., et al. 2007, *ApJ*, 654, 897
- Benson A. J., Bower R. G., Frenk C. S., Lacey C. G., Baugh C. M., Cole S., 2003, *ApJ*, 599, 38
- Benson A. J., Cole S., Frenk C. S., Baugh C. M., Lacey C. G., 2000, *MNRAS*, 311, 793
- Benson A. J., Lacey C. G., Baugh C. M., Cole S., Frenk C. S., 2002, *MNRAS*, 333, 156
- Benson A. J., Pearce F. R., Frenk C. S., Baugh C. M., Jenkins A., 2001, *MNRAS*, 320, 261
- Berrier J. C., Bullock J. S., Barton E. J., Guenther H. D., Zentner A. R., Wechsler R. H., 2006, *ApJ*, 652, 56
- Bertone S., De Lucia G., Thomas P. A., 2007, *MNRAS*, 379, 1143
- Binney J., Tremaine S., 1987, *Galactic dynamics*
- Birnbom Y., Dekel A., 2003, *MNRAS*, 345, 349
- Blaizot J., Guiderdoni B., Devriendt J. E. G., Bouchet F. R., Hatton S. J., Stoehr F., 2004, *MNRAS*, 352, 571
- Blanton M. R., Roweis S., 2007, *AJ*, 133, 734

- Bode P., Ostriker J. P., Turok N., 2001, *ApJ*, 556, 93
- Bond J. R., Cole S., Efstathiou G., Kaiser N., 1991, *ApJ*, 379, 440
- Borgani S., Rosati P., Tozzi P., Stanford S. A., Eisenhardt P. R., Lidman C., Holden B., Della Ceca R., Norman C., Squires G., 2001, *ApJ*, 561, 13
- Bower R. G., Benson A. J., Malbon R., Helly J. C., Frenk C. S., Baugh C. M., Cole S., Lacey C. G., 2006, *MNRAS*, 370, 645
- Boylan-Kolchin M., Ma C.-P., Quataert E., 2008, *MNRAS*, 383, 93
- Boylan-Kolchin M., Springel V., White S. D. M., Jenkins A., Lemson G., 2009, *ArXiv e-prints*
- Bruzual G., Charlot S., 2003, *MNRAS*, 344, 1000
- Bullock J. S., Dekel A., Kolatt T. S., Kravtsov A. V., Klypin A. A., Porciani C., Primack J. R., 2001, *ApJ*, 555, 240
- Bullock J. S., Kravtsov A. V., Weinberg D. H., 2000, *ApJ*, 539, 517
- Bundy K., Fukugita M., Ellis R. S., Kodama T., Conselice C. J., 2004, *ApJ*, 601, L123
- Butcher H., Oemler Jr. A., 1978, *ApJ*, 219, 18
- Calzetti D., Armus L., Bohlin R. C., Kinney A. L., Koornneef J., Storchi-Bergmann T., 2000, *ApJ*, 533, 682
- Cardelli J. A., Clayton G. C., Mathis J. S., 1989, *ApJ*, 345, 245
- Carlberg R. G., Cohen J. G., Patton D. R., Blandford R., Hogg D. W., Yee H. K. C., Morris S. L., Lin H., Hall P. B., Sawicki M., Wirth G. D., Cowie L. L., Hu E., Songaila A., 2000, *ApJ*, 532, L1
- Carroll S. M., Press W. H., Turner E. L., 1992, *ARA&A*, 30, 499
- Cen R., Ostriker J., 1992, *ApJ*, 393, 22
- Cen R., Ostriker J. P., 2000, *ApJ*, 538, 83
- Chabrier G., 2003, *PASP*, 115, 763
- Charlot S., Fall S. M., 2000, *ApJ*, 539, 718
- Chibisov G. V., 1972, *Soviet Astronomy*, 16, 56
- Ciardi B., Madau P., 2003, *ApJ*, 596, 1
- Cimatti A., Daddi E., Renzini A., 2006, *A&A*, 453, L29
- Cole S., Aragon-Salamanca A., Frenk C. S., Navarro J. F., Zepf S. E., 1994, *MNRAS*, 271, 781

- Cole S., Helly J., Frenk C. S., Parkinson H., 2008, MNRAS, 383, 546
- Cole S., Lacey C. G., Baugh C. M., Frenk C. S., 2000, MNRAS, 319, 168
- Colless M., et al. 2001, MNRAS, 328, 1039
- Conroy C., Wechsler R. H., 2008, ArXiv e-prints, 805
- Conroy C., Wechsler R. H., Kravtsov A. V., 2006, ApJ, 647, 201
- Conselice C. J., Bershadsky M. A., Dickinson M., Papovich C., 2003, AJ, 126, 1183
- Couchman H. M. P., Rees M. J., 1986, MNRAS, 221, 53
- Croton D. J., Farrar G. R., 2008, MNRAS, 386, 2285
- Croton D. J., Springel V., White S. D. M., De Lucia G., Frenk C. S., Gao L., Jenkins A., Kauffmann G., Navarro J. F., Yoshida N., 2006, MNRAS, 365, 11
- Davis M., Efstathiou G., Frenk C. S., White S. D. M., 1985, ApJ, 292, 371
- de Jong R. S., Lacey C., 2000, ApJ, 545, 781
- De Lucia G., Blaizot J., 2007, MNRAS, 375, 2
- De Lucia G., Kauffmann G., White S. D. M., 2004, MNRAS, 349, 1101
- De Lucia G., Springel V., White S. D. M., Croton D., Kauffmann G., 2006, MNRAS, 366, 499
- Dehnen W., McLaughlin D. E., Sachania J., 2006, MNRAS, 369, 1688
- Dekel A., Birnboim Y., Engel G., Freundlich J., Goerdt T., Mumcuoglu M., Neistein E., Pichon C., Teyssier R., Zinger E., 2009, Nature, 457, 451
- Dekel A., Silk J., 1986, ApJ, 303, 39
- Desjacques V., Nusser A., 2005, MNRAS, 361, 1257
- Devriendt J. E. G., Guiderdoni B., 2000, A&A, 363, 851
- Di Matteo T., Springel V., Hernquist L., 2005, Nature, 433, 604
- Diemand J., Kuhlen M., Madau P., 2007, ApJ, 657, 262
- Doroshkevich A. G., Zel'Dovich Y. B., Novikov I. D., 1967, Soviet Astronomy, 11, 233
- Dressler A., 1980, ApJ, 236, 351
- Dunkley J., et al. 2009, ApJS, 180, 306
- Efstathiou G., 1992, MNRAS, 256, 43P
- Eisenstein D. J., et al. 2005, ApJ, 633, 560

- Erb D. K., Steidel C. C., Shapley A. E., Pettini M., Reddy N. A., Adelberger K. L., 2006a, *ApJ*, 647, 128
- Erb D. K., Steidel C. C., Shapley A. E., Pettini M., Reddy N. A., Adelberger K. L., 2006b, *ApJ*, 646, 107
- Fabian A. C., Sanders J. S., Allen S. W., Crawford C. S., Iwasawa K., Johnstone R. M., Schmidt R. W., Taylor G. B., 2003, *MNRAS*, 344, L43
- Fall S. M., 1979, *Nature*, 281, 200
- Fan X., Strauss M. A., Becker R. H., White R. L., Gunn J. E., Knapp G. R., Richards G. T., Schneider D. P., Brinkmann J., Fukugita M., 2006, *AJ*, 132, 117
- Fan X., White R. L., Davis M., et al. 2000, *AJ*, 120, 1167
- Farouki R. T., Shapiro S. L., 1982, *ApJ*, 259, 103
- Farouki R. T., Shapiro S. L., Duncan M. J., 1983, *ApJ*, 265, 597
- Field G. B., 1971, *ApJ*, 165, 29
- Firmani C., Avila-Reese V., 2000, *MNRAS*, 315, 457
- Font A. S., Bower R. G., McCarthy I. G., Benson A. J., Frenk C. S., Helly J. C., Lacey C. G., Baugh C. M., Cole S., 2008, *MNRAS*, 389, 1619
- Franx M., Labbé I., Rudnick G., van Dokkum P. G., Daddi E., Förster Schreiber N. M., Moorwood A., Rix H.-W., Röttgering H., van de Wel A., van der Werf P., van Starckenburg L., 2003, *ApJ*, 587, L79
- Gao L., White S. D. M., 2007, *MNRAS*, 377, L5
- Gao L., White S. D. M., Jenkins A., Stoehr F., Springel V., 2004, *MNRAS*, 355, 819
- Gerhard O., Arnaboldi M., Freeman K. C., Kashikawa N., Okamura S., Yasuda N., 2005, *ApJ*, 621, L93
- Ghigna S., Moore B., Governato F., Lake G., Quinn T., Stadel J., 1998, *MNRAS*, 300, 146
- Gilmore G., Wilkinson M. I., Wyse R. F. G., Kleyna J. T., Koch A., Evans N. W., Grebel E. K., 2007, *ApJ*, 663, 948
- Gnedin N. Y., 2000, *ApJ*, 542, 535
- Gonzalez A. H., Zabludoff A. I., Zaritsky D., Dalcanton J. J., 2000, *ApJ*, 536, 561
- Governato F., Brook C. B., Brooks A. M., Mayer L., Willman B., Jonsson P., Stilp A. M., Pope L., Christensen C., Wadsley J., Quinn T., 2008, *ArXiv e-prints*
- Governato F., Mayer L., Wadsley J., Gardner J. P., Willman B., Hayashi E., Quinn T., Stadel J., Lake G., 2004, *ApJ*, 607, 688

- Granato G. L., Lacey C. G., Silva L., Bressan A., Baugh C. M., Cole S., Frenk C. S., 2000, *ApJ*, 542, 710
- Grazian A., Fontana A., Moscardini L., Salimbeni S., Menci N., Giallongo E., de Santis C., Gallozzi S., Nonino M., Cristiani S., Vanzella E., 2006, *A&A*, 453, 507
- Guiderdoni B., Hivon E., Bouchet F. R., Maffei B., 1998, *MNRAS*, 295, 877
- Guiderdoni B., Rocca-Volmerange B., 1987, *A&A*, 186, 1
- Gunn J. E., Gott J. R. I., 1972, *ApJ*, 176, 1
- Guo Q., White S. D. M., 2009, *MNRAS*, 396, 39
- Gustafsson M., Fairbairn M., Sommer-Larsen J., 2006, *Phys. Rev. D*, 74, 123522
- Guth A. H., 1981, *Phys. Rev. D*, 23, 347
- Guth A. H., Pi S.-Y., 1982, *Physical Review Letters*, 49, 1110
- Hatton S., Devriendt J. E. G., Ninin S., Bouchet F. R., Guiderdoni B., Vibert D., 2003, *MNRAS*, 343, 75
- Hawking S. W., 1982, *Physics Letters B*, 115, 295
- Helly J. C., Cole S., Frenk C. S., Baugh C. M., Benson A., Lacey C., 2003, *MNRAS*, 338, 903
- Heymans C., et al. 2005, *MNRAS*, 361, 160
- Hoeft M., Yepes G., Gottlöber S., Springel V., 2006, *MNRAS*, 371, 401
- Hoekstra H., Mellier Y., van Waerbeke L., Semboloni E., Fu L., Hudson M. J., Parker L. C., Tereno I., Benabed K., 2006, *ApJ*, 647, 116
- Irwin M. J., et al. 2007, *ApJ*, 656, L13
- Jeans J. H., 1902, *Royal Society of London Philosophical Transactions Series A*, 199, 1
- Jeltema T. E., Binder B., Mulchaey J. S., 2008, *ApJ*, 679, 1162
- Jena T., Norman M. L., Tytler D., Kirkman D., Suzuki N., Chapman A., Melis C., Paschos P., O'Shea B., So G., Lubin D., Lin W.-C., Reimers D., Janknecht E., Fechner C., 2005, *MNRAS*, 361, 70
- Jenkins L. P., Hornschemeier A. E., Mobasher B., Alexander D. M., Bauer F. E., 2007, *ApJ*, 666, 846
- Jiang C. Y., Jing Y. P., Faltenbacher A., Lin W. P., Li C., 2008, *ApJ*, 675, 1095
- Kang X., Jing Y. P., Mo H. J., Börner G., 2005, *ApJ*, 631, 21
- Kang X., Jing Y. P., Silk J., 2006, *ApJ*, 648, 820

- Katz N., Weinberg D. H., Hernquist L., 1996, *ApJS*, 105, 19
- Kauffmann G., 1996, *MNRAS*, 281, 487
- Kauffmann G., Charlot S., 1998, *MNRAS*, 297, L23+
- Kauffmann G., Colberg J. M., Diaferio A., White S. D. M., 1999, *MNRAS*, 303, 188
- Kauffmann G., Heckman T. M., White S. D. M., Charlot S., Tremonti C., Peng E. W., Seibert M., Brinkmann J., Nichol R. C., SubbaRao M., York D., 2003a, *MNRAS*, 341, 54
- Kauffmann G., Heckman T. M., White S. D. M., et al. 2003b, *MNRAS*, 341, 33
- Kauffmann G., Nusser A., Steinmetz M., 1997, *MNRAS*, 286, 795
- Kauffmann G., White S. D. M., 1993a, *MNRAS*, 261, 921
- Kauffmann G., White S. D. M., Guiderdoni B., 1993b, *MNRAS*, 264, 201
- Kaviani A., Haehnelt M. G., Kauffmann G., 2003, *MNRAS*, 340, 739
- Kennicutt Jr. R. C., 1998, *ApJ*, 498, 541
- Keres D., Katz N., Dave R., Fardal M., Weinberg D. H., 2009, *ArXiv e-prints*
- Kitzbichler M. G., White S. D. M., 2007, *MNRAS*, 376, 2
- Klypin A., Gottlöber S., Kravtsov A. V., Khokhlov A. M., 1999, *ApJ*, 516, 530
- Knebe A., Green A., Binney J., 2001, *MNRAS*, 325, 845
- Koposov S., Belokurov V., Evans N. W., Hewett P. C., Irwin M. J., Gilmore G., Zucker D. B., Rix H.-W., Fellhauer M., Bell E. F., Glushkova E. V., 2008, *ApJ*, 686, 279
- Kravtsov A. V., Gnedin O. Y., Klypin A. A., 2004, *ApJ*, 609, 482
- Kravtsov A. V., Klypin A. A., Khokhlov A. M., 1997, *ApJS*, 111, 73
- Kriek M., van Dokkum P. G., Franx M., Förster Schreiber N. M., Gawiser E., Illingworth G. D., Labbé I., Marchesini D., Quadri R., Rix H.-W., Rudnick G., Toft S., van der Werf P., Wuyts S., 2006, *ApJ*, 645, 44
- Kroupa P., 2002, *Science*, 295, 82
- Krumholz M. R., McKee C. F., Tumlinson J., 2008, *ApJ*, 689, 865
- Lacey C., Cole S., 1993, *MNRAS*, 262, 627
- Larson R. B., Tinsley B. M., Caldwell C. N., 1980, *ApJ*, 237, 692
- Law D. R., Steidel C. C., Erb D. K., Pettini M., Reddy N. A., Shapley A. E., Adelberger K. L., Simenc D. J., 2007, *ApJ*, 656, 1

- Le Fèvre O., Abraham R., Lilly S. J., Ellis R. S., Brinchmann J., Schade D., Tresse L., Colless M., Crampton D., Glazebrook K., Hammer F., Broadhurst T., 2000, MNRAS, 311, 565
- Li C., Kauffmann G., Jing Y. P., White S. D. M., Börner G., Cheng F. Z., 2006, MNRAS, 368, 21
- Li C., White S. D. M., 2009, ArXiv e-prints
- Li Y.-S., White S. D. M., 2008, MNRAS, 384, 1459
- Liddle A. R., Lyth D. H., 2000, *Cosmological Inflation and Large-Scale Structure*
- Lifshitz E. M., 1946, J. Phys. Moscow, 10, 116
- Lin L., Koo D. C., Willmer C. N. A., Patton D. R., Conselice C. J., Yan R., Coil A. L., Cooper M. C., Davis M., Faber S. M., Gerke B. F., Guhathakurta P., Newman J. A., 2004, ApJ, 617, L9
- Madau P., 1995, ApJ, 441, 18
- Maiolino R., et al. 2008, ArXiv e-prints, 806
- Mandelbaum R., McDonald P., Seljak U., Cen R., 2003, MNRAS, 344, 776
- Mandelbaum R., Seljak U., Kauffmann G., Hirata C. M., Brinkmann J., 2006, MNRAS, 368, 715
- Mandelbaum R., Tasitsiomi A., Seljak U., Kravtsov A. V., Wechsler R. H., 2005, MNRAS, 362, 1451
- Marinoni C., Hudson M. J., 2002, ApJ, 569, 101
- Martin C. L., 1997, ApJ, 491, 561
- Martin C. L., 1998, ApJ, 506, 222
- Martin C. L., 1999, ApJ, 513, 156
- McCarthy I. G., Frenk C. S., Font A. S., Lacey C. G., Bower R. G., Mitchell N. L., Balogh M. L., Theuns T., 2008, MNRAS, 383, 593
- McNamara B. R., Nulsen P. E. J., Wise M. W., Rafferty D. A., Carilli C., Sarazin C. L., Blanton E. L., 2005, Nature, 433, 45
- McNamara B. R., Wise M., Nulsen P. E. J., David L. P., Sarazin C. L., Bautz M., Markevitch M., Vikhlinin A., Forman W. R., Jones C., Harris D. E., 2000, ApJ, 534, L135
- Menci N., Fontana A., Giallongo E., Grazian A., Salimbeni S., 2006, ApJ, 647, 753
- Merritt D., Graham A. W., Moore B., Diemand J., Terzić B., 2006, AJ, 132, 2685

- Merritt D., Navarro J. F., Ludlow A., Jenkins A., 2005, *ApJ*, 624, L85
- Mihos J. C., Harding P., Feldmeier J., Morrison H., 2005, *ApJ*, 631, L41
- Mihos J. C., Hernquist L., 1994, *ApJ*, 425, L13
- Mihos J. C., Hernquist L., 1996, *ApJ*, 464, 641
- Miller G. E., Scalo J. M., 1979, *ApJS*, 41, 513
- Milne M. L., Pritchett C. J., Poole G. B., Gwyn S. D. J., Kavelaars J. J., Harris W. E., Hanes D. A., 2007, *AJ*, 133, 177
- Miralda-Escudé J., Haehnelt M., Rees M. J., 2000, *ApJ*, 530, 1
- Mo H. J., Mao S., White S. D. M., 1998, *MNRAS*, 295, 319
- Mobasher B., Colless M., Carter D., Poggianti B. M., Bridges T. J., Kranz K., Komiyama Y., Kashikawa N., Yagi M., Okamura S., 2003, *ApJ*, 587, 605
- Monaco P., Fontanot F., Taffoni G., 2007, *MNRAS*, 375, 1189
- Moore B., Ghigna S., Governato F., Lake G., Quinn T., Stadel J., Tozzi P., 1999, *ApJ*, 524, L19
- Moore B., Katz N., Lake G., Dressler A., Oemler A., 1996, *Nature*, 379, 613
- Naab T., Burkert A., 2003, *ApJ*, 597, 893
- Nagashima M., Gouda N., Sugiura N., 1999, *MNRAS*, 305, 449
- Nagashima M., Lacey C. G., Okamoto T., Baugh C. M., Frenk C. S., Cole S., 2005, *MNRAS*, 363, L31
- Navarro J. F., Frenk C. S., White S. D. M., 1997a, *ApJ*, 490, 493
- Navarro J. F., Steinmetz M., 1997b, *ApJ*, 478, 13
- Navarro J. F., Steinmetz M., 2000, *ApJ*, 528, 607
- Navarro J. F., White S. D. M., 1994, *MNRAS*, 267, 401
- Negroponte J., White S. D. M., 1983, *MNRAS*, 205, 1009
- Okamoto T., Eke V. R., Frenk C. S., Jenkins A., 2005, *MNRAS*, 363, 1299
- Okamoto T., Gao L., Theuns T., 2008, *MNRAS*, 390, 920
- Okamoto T., Nagashima M., 2001, *ApJ*, 547, 109
- Okamoto T., Nagashima M., 2003, *ApJ*, 587, 500
- Ott J., Walter F., Brinks E., 2005, *MNRAS*, 358, 1453

- Panuzzo P., Silva L., Granato G. L., Bressan A., Vega O., 2005, in Popescu C. C., Tuffs R. J., eds, *The Spectral Energy Distributions of Gas-Rich Galaxies: Confronting Models with Data* Vol. 761 of American Institute of Physics Conference Series, Panchromatic models of galaxies: GRASIL. pp 187–196
- Papovich C., Dickinson M., Giavalisco M., Conselice C. J., Ferguson H. C., 2005, *ApJ*, 631, 101
- Papovich C., et al. 2006, *ApJ*, 640, 92
- Parkinson H., Cole S., Helly J., 2008, *MNRAS*, 383, 557
- Patton D. R., Pritchett C. J., Carlberg R. G., Marzke R. O., Yee H. K. C., Hall P. B., Lin H., Morris S. L., Sawicki M., Shepherd C. W., Wirth G. D., 2002, *ApJ*, 565, 208
- Peacock J. A., 1999, *Cosmological Physics*
- Peacock J. A., Smith R. E., 2000, *MNRAS*, 318, 1144
- Peebles P. J. E., 1993, *Principles of physical cosmology*
- Peebles P. J. E., Yu J. T., 1970, *ApJ*, 162, 815
- Percival W. J., et al. 2002, *MNRAS*, 337, 1068
- Pettini M., Shapley A. E., Steidel C. C., Cuby J.-G., Dickinson M., Moorwood A. F. M., Adelberger K. L., Giavalisco M., 2001, *ApJ*, 554, 981
- Pfrommer C., Springel V., Enßlin T. A., Jubelgas M., 2006, *MNRAS*, 367, 113
- Popesso P., Böhringer H., Romaniello M., Voges W., 2005, *A&A*, 433, 415
- Press W. H., Schechter P., 1974, *ApJ*, 187, 425
- Quadri R., et al. 2007a, *AJ*, 134, 1103
- Quadri R., van Dokkum P., Gawiser E., Franx M., Marchesini D., Lira P., Rudnick G., Herrera D., Maza J., Kriek M., Labbé I., Francke H., 2007b, *ApJ*, 654, 138
- Quadri R. F., Williams R. J., Lee K.-S., Franx M., van Dokkum P., Brammer G. B., 2008, *ArXiv e-prints*, 808
- Quilis V., Moore B., Bower R., 2000, *Science*, 288, 1617
- Reddy N. A., Steidel C. C., Fadda D., Yan L., Pettini M., Shapley A. E., Erb D. K., Adelberger K. L., 2006, *ApJ*, 644, 792
- Reddy N. A., Steidel C. C., Pettini M., Adelberger K. L., Shapley A. E., Erb D. K., Dickinson M., 2008, *ApJS*, 175, 48
- Rees M. J., Ostriker J. P., 1977, *MNRAS*, 179, 541

- Sakamoto T., Chiba M., Beers T. C., 2003, *A&A*, 397, 899
- Salpeter E. E., 1955, *ApJ*, 121, 161
- Sanders D. B., Soifer B. T., Elias J. H., Madore B. F., Matthews K., Neugebauer G., Scoville N. Z., 1988, *ApJ*, 325, 74
- Sawala T., Scannapieco C., White S. D. M., 2009, ArXiv e-prints
- Scalo J. M., 1986, *Fundamentals of Cosmic Physics*, 11, 1
- Scannapieco C., White S. D. M., Springel V., Tissera P. B., 2009, *MNRAS*, 396, 696
- Schmidt M., 1959, *ApJ*, 129, 243
- Seljak U., 2000, *MNRAS*, 318, 203
- Shankar F., Lapi A., Salucci P., De Zotti G., Danese L., 2006, *ApJ*, 643, 14
- Shapley A. E., Steidel C. C., Erb D. K., Reddy N. A., Adelberger K. L., Pettini M., Barmby P., Huang J., 2005, *ApJ*, 626, 698
- Silk J., 1967, *Nature*, 215, 1155
- Silk J., 1968, *ApJ*, 151, 459
- Smith M. C., et al. 2007, *MNRAS*, 379, 755
- Somerville R. S., 2002, *ApJ*, 572, L23
- Somerville R. S., Hopkins P. F., Cox T. J., Robertson B. E., Hernquist L., 2008, *MNRAS*, 391, 481
- Somerville R. S., Kolatt T. S., 1999a, *MNRAS*, 305, 1
- Somerville R. S., Primack J. R., 1999b, *MNRAS*, 310, 1087
- Somerville R. S., Primack J. R., Faber S. M., 2001, *MNRAS*, 320, 504
- Sommer-Larsen J., Dolgov A., 2001, *ApJ*, 551, 608
- Sommer-Larsen J., Gelato S., Vedel H., 1999, *ApJ*, 519, 501
- Spergel D. N., Verde L., Peiris H. V., Komatsu E., et al. 2003, *ApJS*, 148, 175
- Springel V., 2005c, *MNRAS*, 364, 1105
- Springel V., Di Matteo T., Hernquist L., 2005a, *ApJ*, 620, L79
- Springel V., Frenk C. S., White S. D. M., 2006, *Nature*, 440, 1137
- Springel V., Hernquist L., 2003, *MNRAS*, 339, 289

Bibliography

- Springel V., Wang J., Vogelsberger M., Ludlow A., Jenkins A., Helmi A., Navarro J. F., Frenk C. S., White S. D. M., 2008, *MNRAS*, 391, 1685
- Springel V., White S. D. M., Jenkins A., Frenk C. S., Yoshida N., Gao L., Navarro J., Thacker R., Croton D., Helly J., Peacock J. A., Cole S., Thomas P., Couchman H., Evrard A., Colberg J., Pearce F., 2005b, *Nature*, 435, 629
- Springel V., White S. D. M., Tormen G., Kauffmann G., 2001, *MNRAS*, 328, 726
- Starobinsky A. A., 1982, *Physics Letters B*, 117, 175
- Steidel C. C., Adelberger K. L., Shapley A. E., Pettini M., Dickinson M., Giavalisco M., 2003, *ApJ*, 592, 728
- Steidel C. C., Giavalisco M., Pettini M., Dickinson M., Adelberger K. L., 1996, *ApJ*, 462, L17+
- Steidel C. C., Shapley A. E., Pettini M., Adelberger K. L., Erb D. K., Reddy N. A., Hunt M. P., 2004, *ApJ*, 604, 534
- Sun M., Jones C., Forman W., Vikhlinin A., Donahue M., Voit M., 2007, *ApJ*, 657, 197
- Tegmark M., et al. 2004, *Phys. Rev. D*, 69, 103501
- Thacker R. J., Couchman H. M. P., 2001, *ApJ*, 555, L17
- Thomas D., 1999, *MNRAS*, 306, 655
- Thoul A. A., Weinberg D. H., 1996, *ApJ*, 465, 608
- Toomre A., 1964, *ApJ*, 139, 1217
- Toomre A., 1976, in *Bulletin of the American Astronomical Society Vol. 8 of Bulletin of the American Astronomical Society, INVITED PAPER - Interacting Galaxies*. pp 354–+
- Tremonti C. A., Heckman T. M., Kauffmann G., Brinchmann J., Charlot S., White S. D. M., Seibert M., Peng E. W., Schlegel D. J., Uomoto A., Fukugita M., Brinkmann J., 2004, *ApJ*, 613, 898
- Vale A., Ostriker J. P., 2004, *MNRAS*, 353, 189
- Vale A., Ostriker J. P., 2006, *MNRAS*, 371, 1173
- van Dokkum P. G., 2005, *AJ*, 130, 2647
- Van Waerbeke L., Mellier Y., Pelló R., Pen U.-L., McCracken H. J., Jain B., 2002, *A&A*, 393, 369
- Velazquez H., White S. D. M., 1999, *MNRAS*, 304, 254
- Wang J., De Lucia G., Kitzbichler M. G., White S. D. M., 2008, *MNRAS*, 384, 1301

- Wang L., Li C., Kauffmann G., De Lucia G., 2006, MNRAS, 371, 537
- Webb T. M., Eales S., Foucaud S., Lilly S. J., McCracken H., Adelberger K., Steidel C., Shapley A., Clements D. L., Dunne L., Le Fèvre O., Brodwin M., Gear W., 2003, ApJ, 582, 6
- Weinberg D. H., Hernquist L., Katz N., 1997, ApJ, 477, 8
- Weinberg S., 1971, ApJ, 168, 175
- Weinberg S., 1972, Gravitation and Cosmology: Principles and Applications of the General Theory of Relativity
- White S. D. M., 1978, MNRAS, 184, 185
- White S. D. M., Frenk C. S., 1991, ApJ, 379, 52
- White S. D. M., Navarro J. F., Evrard A. E., Frenk C. S., 1993, Nature, 366, 429
- White S. D. M., Rees M. J., 1978, MNRAS, 183, 341
- Wilkinson M. I., Evans N. W., 1999, MNRAS, 310, 645
- Willman B., Dalcanton J. J., Martinez-Delgado D., West A. A., Blanton M. R., Hogg D. W., Barentine J. C., Brewington H. J., Harvanek M., Kleinman S. J., Krzesinski J., Long D., Neilsen Jr. E. H., Nitta A., Snedden S. A., 2005, ApJ, 626, L85
- Xue X. X., Rix H. W., Zhao G., Re Fiorentin P., Naab T., Steinmetz M., van den Bosch F. C., Beers T. C., Lee Y. S., Bell E. F., Rockosi C., Yanny B., Newberg H., Wilhelm R., Kang X., Smith M. C., Schneider D. P., 2008, ApJ, 684, 1143
- York D. G., Adelman J., Anderson Jr. J. E., et.al 2000, AJ, 120, 1579
- Yoshida N., Stoehr F., Springel V., White S. D. M., 2002, MNRAS, 335, 762
- Zibetti S., White S. D. M., Schneider D. P., Brinkmann J., 2005, MNRAS, 358, 949
- Zucker D. B., et al. 2006, ApJ, 643, L103

Curriculum vitae

Max Planck Institute for Astrophysics
Karl-Schwarzschild-Str. 1
85741 Garching, Germany

Phone: +49 89 30000 2207
Fax: +49 89 30000 2235
E-mail: guoqi@mpa-garching.mpg.de

Biographical Data

Date of Birth:	February 18, 1980
Place of Birth:	China
Marital Status:	Single
Citizenship:	China
Sex:	Female

Research Interests

- Galaxy Formation and evolution
- Merging of galaxies and dark matter halos
- Galaxy clusters
- Chemical evolution
- Environment effects on galaxy formation
- High redshift galaxies
- Globular clusters
- Large-scale structure
- SN and AGN feedback

Education

2006-	PhD in Astrophysics Max Planck Institute for Astrophysics Supervisors: Prof. Simon D.M. White
2002-2005	M.Sc. in Theoretical Physics Institute of Theoretical Physics, Chinese Academy of Science Supervisor: Prof. Rong-Gen Cai
1999-2002	Bachelor in Theoretical Physics NanKai University

Computer Skills

- Languages: C, Fortran, IDL
- Applications: L^AT_EX, common Windows spreadsheet and presentation software
- Simulation L-Galaxy (Semi-analytic simulation)
- Operating Systems: Unix/Linux, Windows

Scientific Talks

- June. 2009 “Mock COSMOS Surveys: Galaxy Formation in A Simulated Universe”
COSMOS meeting, Matsuyama, Japan
- Feb. 2009 “Galaxy Formation in a LCDM Universe”
The 8th Sino-German workshop on galaxy formation and cosmology, KunMing, China
- Jan. 2009 “Galaxy Formation in MS-I and MS-II”
VIRGO meeting, Garching
- Oct. 2008 “High Redshift Galaxy Populations and Their Descendants”
Cosmology Seminar, MPA-Garching
- Jun. 2008 “Galaxy Sizes in a LCDM Universe”
IAU254, Copenhagen
- Apr. 2008 “Reproducing the Observed Universe with Simulations”
VO workshop, MPE-Garching
- Feb. 2008 “Get into L-Galaxies”
Informal Meeting, MPA-Garching
- Nov. 2007 “Galaxy Growth in the Concordance LCDM Cosmology”
IMPRS Seminar, MPE-Garching
- Nov. 2007 “Tidal Effects and Strangulation in Satellite Galaxies”
MPA/SHAO workshop, MPA-Garching

Refereed Scientific Publications

Qi Guo, Simon D. M. White
Galaxy growth in the concordance LCDM cosmology
MNRAS, 2008, 384, 2

Qi Guo, Simon D. M. White
High Redshift Galaxy Populations and their Descendants

MNRAS, 2009, 396, 39

Roderik Overzier, Qi Guo, Guinevere Kauffmann, Gabriella De Lucia, Rychard Bouwens, Gerard Lemson

ΛCDM predictions for galaxy protoclusters I: the relation between galaxies, protoclusters and quasars at $z \sim 6$

MNRAS, 2009, 394, 577

Wei Zhang, Cheng Li, Guinevere Kauffmann, Hu Zou, Barbara Catinella, Shiyin Shen, Qi Guo, Ruixiang Chang

Estimating the H I gas fractions of galaxies in the local Universe

arXiv: 0902.2392, accepted by MNRAS

Qi Guo, Simon D. M. White

Disk Sizes in a ΛCDM Universe

IAUS, 2009, 254, 411

Qi Guo, Cheng Li, Simon D. M. White

Galaxy formation efficiency

2009, in preparation

Qi Guo, Simon D. M. White

Dwarf Galaxy Formation and Environment Effects

2009, in preparation

Refereed Scientific Publications in Theoretical Cosmology

Qi Guo, Rong-Gen Cai

Classification of Cosmological Trajectories

arXiv:gr-qc/0504033

Hongsheng Zhang, Qi Guo, Rong-Gen Cai

Friedmann cosmology on codimension 2 brane with time dependent tension

Mod.Phys.Lett. 2006, 21, 159

Rong-Gen Cai, Qi Guo

Gauss-Bonnet Black Holes in dS Spaces

Phys.Rev. D 2004, 69, 104025